MOBILE HYBRID ROBOTS WITH ADAPTIVE MORPHOLOGY FOR ADVANCED LOCOMOTION AND OBJECT MANIPULATION

LUIZA LABAZANOVA
PhD

The Hong Kong Polytechnic University
2025

The Hong Kong Polytechnic University
Department of Mechanical Engineering

Mobile Hybrid Robots with Adaptive Morphology for Advanced Locomotion and Object Manipulation

Luiza Labazanova

A thesis submitted in partial fulfillment of the requirements
for the degree of Doctor of Philosophy

August 2024

CERTIFICATE OF ORIGINALITY

I hereby declare that this thesis is my own work and that, to the best of my knowledge and belief, it reproduces no material previously published or written, nor material that has been accepted for the award of any other degree or diploma, except where due acknowledgement has been made in the text.

Signature:
Name of Student: Luiza Labazanova

ABSTRACT

Mobile robots have demonstrated exceptional capabilities in traversing diverse environments, while manipulators excel at precise object interaction. However, combining these functionalities within a single compact system remains challenging, particularly for applications requiring navigation through confined spaces while maintaining object handling capabilities. This thesis introduces a novel solution: a hybrid mobile robot with adaptive stiffness and morphology that can transition between functioning as an efficient mobile platform and a versatile manipulator.

The proposed system features a dual locomotion unit architecture connected by a variable stiffness bridge incorporating low melting point alloy. This design enables controlled transitions between rigid and flexible states, providing stability during locomotion and adaptability during manipulation. The robot's modular construction significantly reduces stiffness transition time while maintaining optimal mechanical properties throughout operation. Each locomotion unit functions autonomously while collectively facilitating coordinated bridge deformation during flexible states, enabling precise morphological adaptations for object manipulation.

This dissertation presents the complete development process from design conceptualization to experimental validation. A comprehensive hybrid kinematic model characterizes the robot's behavior across both rigid and flexible states, identifying four distinct locomotion modes emerging from its variable stiffness capabilities. The hierarchical control framework integrates stiffness management with motion planning through model predictive control schemes that optimize performance across operational modes. For navigation, two complementary approaches are implemented: a hybrid RRT*-APF algorithm for environments with sparse obstacles, and a sophisticated Voronoi-based optimization method for highly cluttered environments requiring morphological adaptations.

Experimental results demonstrate the robot's capacity for efficient omnidirectional mobility, rapid stiffness transitions, and effective full-body grasping of objects with diverse geometries. The system successfully navigates through confined spaces by leveraging its variable morphology to adapt to environmental constraints. Performance metrics validate significant advantages over conventional single-function systems in terms of versatility, adaptability, and operational effectiveness across multiple domains.

This research establishes fundamental design principles and control methodologies for a new generation of multifunctional robots with adaptive properties. The contributions advance the field of robotics by bridging the gap between conventional rigid systems and soft robots, creating versatile platforms capable of addressing complex challenges in exploration, inspection, and search and rescue operations where both mobility and manipulation capabilities are essential within strict size constraints.

Contents

List of Tables

List of Figures

List of Abbreviations

2SR	Self-reconfigurable soft rigid
2SRA	Self-reconfigurable soft rigid agent
APF	Artificial potential field
AWG	American wire gauge
CC	Constant curvature
DOF	Degrees of freedom
DTW	Dynamic time warping
FSM	Finite State Machine
IR	Infrared
LMPA	Low-melting point alloy
LU	Locomotion unit
MC	Mean curvature
MIMO	Multiple input and multiple output
M&M	Motion & morphology controller
MPC	Model predictive control
MU	Modular unit
NTC	Negative temperature coefficient
PID	Proportional–integral–derivative controller
PWM	Pulse-width modulation
RGB	Red-green-blue color model
RRT	Rapidly exploring random tree
SMA	Shape memory alloy
SMP	Shape memory polymer
VAMP	Voronoi-assisted morphological planning
VS	Variable stiffness

VSB	Variable stiffness bridge
VSS	Variable stiffness segment

ACKNOWLEDGEMENTS

First and foremost, I extend my deepest appreciation to my supervisor, Dr. David Navarro-Alarcon, Associate Professor from the Department of Mechanical Engineering at PolyU. His mentorship, unwavering support, encouragement, and patience have been instrumental throughout my PhD journey. Dr. Navarro-Alarcon's valuable insights and advice have significantly shaped my professional and personal development. More than a supervisor, he became a friend, supporting me not only in research but also in my personal life, always ready to help during my most challenging times. His approach made this PhD not just about fulfilling requirements, but also about communication and joy.

I am also grateful to my co-supervisor, Dr. Thrishantha Nanayakkara, Professor in Robotics from the Dyson School of Design Engineering at Imperial College London. His acceptance of me as an exchange student in his Morph Lab provided me with new learning opportunities and experiences. His accommodating nature made my time at Imperial College both productive and enjoyable.

A special thanks goes to my invaluable student helpers, Liuming Qiu and Shuang Peng. Their exceptional knowledge, expertise, and work ethic set them apart. Their significant contributions to my research and their constant willingness to assist were crucial to my progress.

I owe a debt of gratitude to my friend and senior, Maria Victorova. As the only person I knew when I first arrived in Hong Kong, her consideration and guidance about living here helped me adapt to a new place and find new friends.

I would like to thank my colleagues Dr. Samantha Lee, Bowen Fan, Bin Zhang, Hui Zhi, Dr. Jeffery Zhou, Zeyu Wu, Aamir Mahmood, Bilal Hussain, Dr. Celia Saghour, and many other friends from PolyU and other universities for their help and support during my PhD study. My labmates deserve special mention for making this PhD journey colorful and interesting. The non-lab activities we shared made them like a second family to me.

I am thankful to my friend Chris Hoellriegl for her constant concern about my well-being and her persistent efforts to get me out of my dungeon of the lab to enjoy life outside.

My heartfelt thanks go to my old friends from home - Adam Vishanov, Tamara Mataeva, Selita Hazbulatova, and others - for their constant support despite the distance. Their presence was always felt, and our friendship only grew stronger. I especially appreciate Tamara and Selita for visiting me in Hong Kong, making it a special time for me.

Last but certainly not least, I express my profound gratitude to my family - my parents and my sister Elizaveta. Their unconditional love and support have been my anchor. I owe a special debt to my mother, whose constant support and sacrifices have shaped me into who I am today. Despite all the difficulties and hardships, she gave me everything she could to provide me with a good life and education.

I cannot thank enough everyone who has supported me, worked with me, and taught me. This five-year journey has been a special and unforgettable experience of my life.

I dedicate this thesis to the best mom in the world

Chapter 1

Introduction

TASK-specific robots have demonstrated remarkable performance in assisting people across various domains; however, their limited versatility restricts applications requiring diverse behaviours and advanced capabilities, particularly in uncontrolled, changing environments. This creates a clear need for *multifunctional* robotic systems, especially those combining land-based mobility with the ability to interact with objects of arbitrary shapes. We propose that such multifunctionality can be achieved through hybrid robots with *adaptive stiffness and morphology*. Their controllable properties enable switching between different operational modes, each providing distinct functions. In this chapter, we explore various approaches to developing robots that can navigate through tight spaces while maintaining object manipulation abilities, define research objectives, and outline the thesis structure.

1.1 Effectiveness vs Versatility in Robotics

Robots have steadily integrated into numerous aspects of human life since their inception, primarily designed to automate manual labor and streamline processes. Initially dominated by industrial applications [1], robotic systems have expanded into transportation [2] and logistics [3, 4], exploration [5] and surveillance [6], healthcare [7], entertainment [8], and various other domains. Such rapid development has been driven by advancements in physics, mechanical and electrical engineering, optics, material science, and computer science, collectively enabling robots to become increasingly sophisticated and intelligent.

Today's robotic landscape features a large diversity of machines, each engineered for specific tasks across numerous fields. This specialization stems from a fundamental approach in robotics development: identifying a particular problem or application and subsequently designing a robot with precise capabilities to address that specific task. While this approach has produced highly effective task-specific robots, it has simultaneously created systems that lack *versatility*.

This presents a stark contrast to human capabilities. Humans, while rarely exceptional at any specific task, possess remarkable versatility across a broad spectrum of activities [9]. Robots, conversely, excel in their narrowly defined functions but struggle outside their designated parameters. This specialization, though advantageous in controlled environments, introduces several significant limitations:

- **Limited adaptability**: Task-specific robots typically feature fixed morphologies and capabilities, significantly restricting their ability to adapt to new or unforeseen challenges. Their inherent rigidity renders them less effective in dynamic or unpredictable environments where versatility becomes essential. When conditions change beyond their design parameters, these specialized machines often fail entirely.

- **Costly maintenance and development**: The inability of robots to adapt means that task modifications or environmental changes frequently necessitate developing entirely new systems. This approach demands substantial investments in financial resources, development time, and specialized expertise. Furthermore, maintaining diverse fleets of specialized robots increases operational complexity and costs while reducing overall system efficiency.

- **Scaling challenges**: Integrating various specialized robots into cohesive, collaborative systems presents significant technical hurdles due to incompatible standards and interfaces. This incompatibility fundamentally limits the deployment potential of large-scale, coordinated robotic systems that could otherwise address complex, multifaceted challenges.

These limitations highlight the growing need for multifunctional robotic platforms — systems capable of performing diverse tasks within changing environments while maintaining operational efficiency. By functionality, task-specific robots can be broadly categorized into two major types (examples in Fig. 1.1):

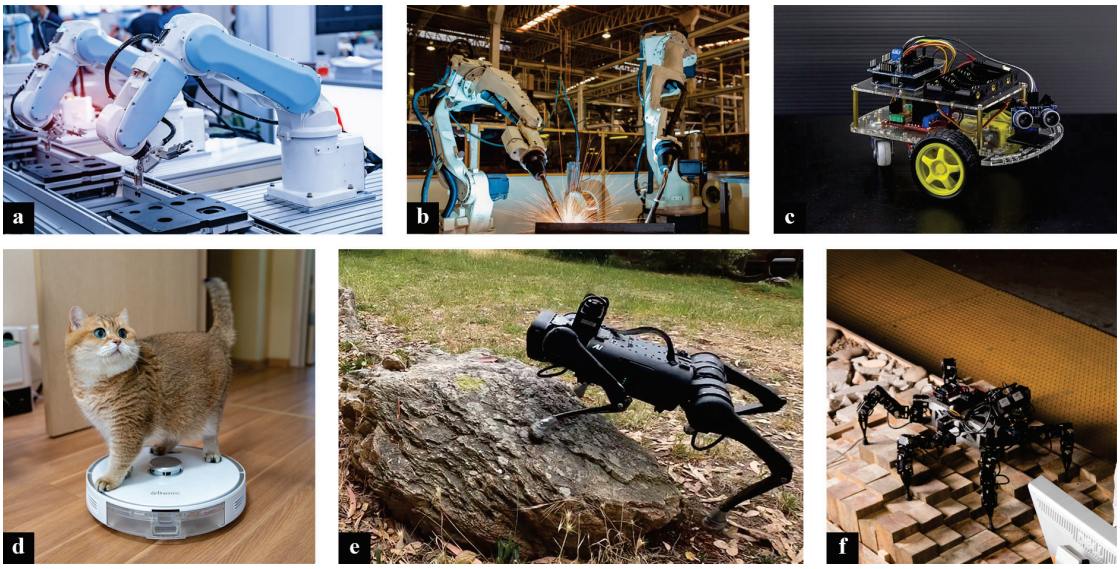

Figure 1.1: Examples of uni-functional robots. Manipulation robots used for: (a) assembly; (b) welding. Mobile robots: (c) differential wheeled robot [10]; (d) robot vacuum cleaner; (e) quadruped robot [11]; (f) legged robot [12].

- **Manipulation robots** are designed to interact with objects, typically featuring robotic arms [13–15] or grippers [16, 17] that can perform tasks such as assembly [18], welding [19], and material handling [20]. These robots are characterized by their precision, strength, and ability to perform repetitive tasks with high accuracy. The most well-established manipulators are industrial robotic arms used in manufacturing [21] and surgical robots used in medical procedures [22].

- **Mobile robots** are designed for movement and navigation [23]. They can be further classified into various types based on their operational environments:

  - **Marine robots** are vehicles for maritime applications [24, 25].

  - **Land-based robots** navigate terrestrial environments through different locomotion mechanisms, each designed to address specific mobility challenges and operational requirements. Wheeled robots are the most investigated and frequently used set of mobile robots [26]. They can cover long distances on plain surfaces at high speed. Wheeled robots are commonly used in drop shipping [27] and transportation in warehouses [28]. Legged robots are designed to traverse rough terrains where wheel robots fail to perform [11, 12, 29]. These robots are typically more

complex in design and control. Legged robots are perfect candidates for exploration missions and rescue operations [30].

– **Aerial drones**: are the most recent mobile robots and quickly gained popularity due to their ability to access remote or dangerous areas, facilitate environmental monitoring and capture high-resolution imagery [31]. Due to these functions, they are actively used in military, industrial and commercial applications [32].

We can observe that while manipulation robots excel in interacting with objects, they lack mobility. Conversely, mobile robots are adept at motion but lack sophisticated interaction capabilities with their surroundings. Though researchers have attempted to bridge this gap by integrating manipulators onto mobile platforms [33–35], the resulting systems often prove bulky and primarily confined to structured industrial settings. This integration challenge becomes especially significant when considering applications requiring *navigation through tight spaces while maintaining object interaction capabilities* — a critical requirement for industrial inspection tasks, search and rescue operations in disaster zones, and maintenance work in confined environments such as pipe systems or collapsed structures, see Fig. 1.2. The conflict between achieving both *compactness* and *functional versatility* represents a persistent challenge in developing robots suitable for these complex operational domains, where spatial constraints and manipulation needs coexist.

Figure 1.2: Applications that require multifunctional robots.

1.2 Development of Multifunctional Robots

In this section, we analyze existing approaches to multifunctional robot design and identify possible ways to achieve desired versatility.

1.2.1 Limitations of Conventional Hard Machines

Conventional robots are characterized by rigid links, fixed joints, and invariable structures composed of hard materials with static properties. These design principles have enabled robots with remarkable strength, precision, and speed — attributes that have secured their position in industrial and manufacturing settings. Hard robots utilize conventional electronics and power systems that provide continuous state monitoring and predictable control. Their discrete topology with finite degrees of freedom simplifies modeling and control implementation but simultaneously restricts their adaptability and behavioural versatility [36].

The rigid-bodied design approach offers significant advantages in specific contexts. Manufacturing environments benefit from robots that can handle substantial loads with high precision, performing repetitive tasks such as assembly, welding, painting, and quality inspection with consistent accuracy. This reliability has revolutionized production processes across industries. However, this approach is lacking when attempting to develop multifunctional robots. Current mobile manipulators [33–35] are a prime example of it, as demonstrated in Fig. 1.3. These systems typically consist of a robotic arm mounted atop a standard mobile platform — essentially a direct combination of two single-function robots. This design philosophy represents a *mechanical compromise* rather than an *integrated solution*.

Figure 1.3: Examples of conventional mobile manipulators. **Left**: KUKA KMR QUANTEC. **Right**: Aubo Robotics AMR300.

The challenge stems from an inherent constraint: a structure with fixed material properties and unchangeable configuration can only efficiently optimize for a single function or a set of closely related functions. When attempting to incorporate multiple functionalities into a conventional hard robot, engineers must either:

1. Accept performance compromises across all functions.
2. Significantly increase system complexity, size, and weight.
3. Narrow the operational range to address only specific use cases.

This fundamental limitation explains why most robots excel at specialized tasks but struggle with functional versatility. Mobile manipulators, despite combining two functionalities, often become bulky, energy-inefficient, and impractical for confined spaces or dynamic environments. Their rigid structure cannot adapt to changing task requirements or environmental conditions.

The inherent constraints of conventional hard machines point toward a necessary paradigm shift in robotics design. Rather than continuing to stack discrete functional components onto increasingly complex platforms, we must reconsider the foundational principles guiding robot development. This realization leads us to explore new approaches that enable genuine multifunctionality through adaptive morphology and material properties.

1.2.2 Adaptive Morphology for Expanded Functionality

Adaptive morphology represents a paradigm shift in robotics design, enabling systems to dynamically modify their physical structure and behavioural characteristics in response to changing operational conditions. Unlike conventional rigid robots, adaptively morphing systems can accommodate opposing dynamic requirements (e.g., maneuverability, efficiency, and speed) when navigating diverse environments or transitioning between different substrates. This design philosophy offers a promising solution for endowing robots with multiple functionalities, including enhanced transportability and self-protection mechanisms [37].

Multi-modal locomotion stands as the most compelling application of adaptive morphology. Researchers have developed robots that exploit morphing appendages to facilitate seamless transitions between diverse locomotion modes. Recent ad-

vances have demonstrated remarkable combinations of movement capabilities, including jumping-gliding systems [38–40], and rolling-climbing mechanisms [41–43]. This approach extends to cross-environmental locomotion, with significant progress in aerial-terrestrial robots that can both fly and walk effectively [44–46], and aerial-aquatic systems capable of operating above and below water surfaces [47–49].

Beyond locomotion, adaptive morphology offers transformative potential for *functional versatility*. Since function is often directly encoded in physical structure, the ability to reconfigure shape enables multiple functionalities within a single system. This principle aligns with emerging concepts of programmable and smart matter — materials that can assume different morphological configurations and consequently perform various tasks [50]. Such approaches directly address the hardware limitations inherent in conventional robotic systems.

The field has established several promising directions for implementation. Reconfigurable modular systems represent one established approach, utilizing collections of simple robotic units that can physically connect and collaborate to form complex functional structures [51–53]. Alternative strategies leverage the structural and material properties of a single continuous system, as exemplified by self-folding [54, 55] and origami [56, 57] robots that morph into different configurations to perform diverse tasks.

The advancement of adaptive morphology is fundamentally tied to progress in materials science and engineering design. While showing tremendous potential, this approach remains in early developmental stages and lacks standardized methodologies. It necessitates the integration of novel technologies and unconventional design principles, requiring researchers to explore diverse implementation strategies. The field's evolution demands cross-disciplinary collaboration between roboticists, materials scientists, and engineers to overcome significant technical challenges related to actuation, sensing, control, and energy efficiency in morphologically adaptive systems.

As this research domain matures, it promises to deliver robotic platforms that transcend the single-function limitations of conventional machines, offering genuine versatility through structural adaptation rather than mechanical complexity.

1.2.3 Hybrid Robotics: Trade-off in Hard-Soft Design

The embodiment of adaptive morphology is perhaps most vividly realized in *soft robotics*. Despite being a relatively young field, soft robotics has demonstrated remarkable achievements in adaptability through its inherent compliance [58]. These systems primarily utilize soft elastic elastomers, such as silicone, combined with fluidic or pneumatic actuation mechanisms [59] that allow them to adapt to their environment and interact safely with humans [60]. These robots feature continuously deformable structures with muscle-like actuation that emulates biological systems, resulting in a relatively large number of degrees of freedom compared with their hard-bodied counterparts. Soft robots have proven particularly effective as grippers and manipulators [61–63], leveraging their ability to conform to objects of diverse geometries and execute damage-free grasping operations. Fig. 1.4 shows several examples of soft robots introduced by the scientific community.

While soft robots excel in adaptability and safety, these advantages come with significant trade-offs. Their limitations include reduced force capacity and restricted mobility — soft robots often require external actuators [68,69], exhibit slow and imprecise movement [70], and present greater modeling and control challenges compared to rigid systems [71]. Furthermore, the development of autonomous mobile soft robots is hindered by the lack of sophisticated flexible electronics, making it practically impossible to create fully self-contained soft machines.

This situation stands in direct contrast to conventional hard robots. This inher-

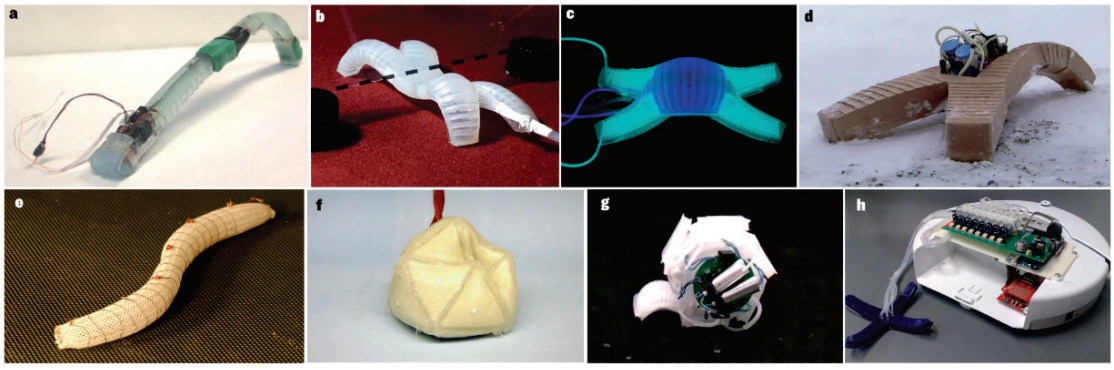

Figure 1.4: Examples of soft robots: (a) Caterpillar-inspired locomotion; (b) A multi-gait quadruped [64]; (c) Active camouflage [65]; (d) Walking in hazardous environments [66]; (e) Worm-inspired locomotion [67]; (f) Particle-jamming-based actuation; (g) Rolling powered by a pneumatic battery; (h) A hybrid hard–soft robot.

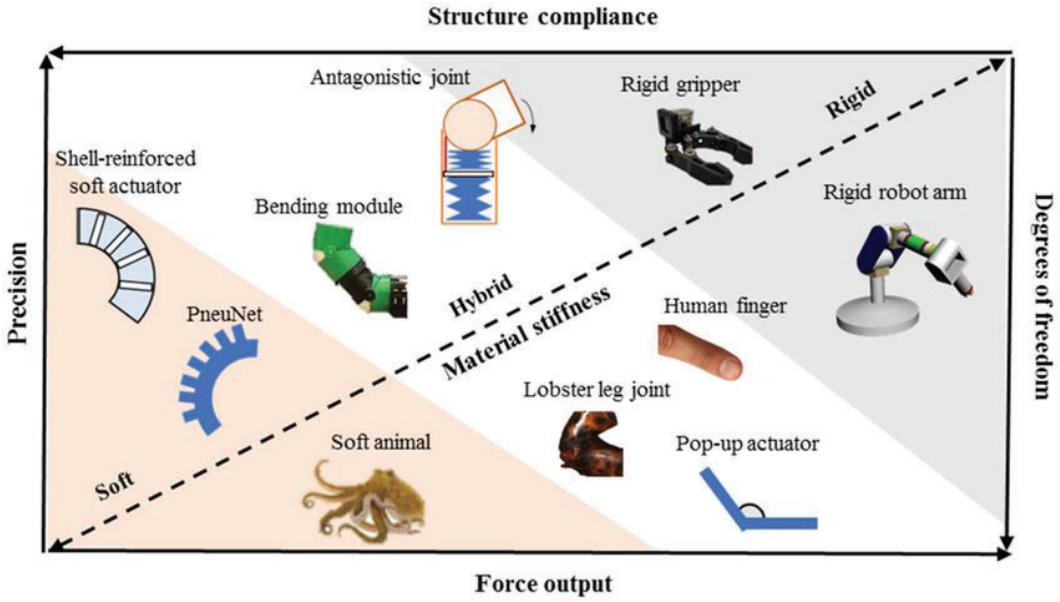

Figure 1.5: Classification of robots into rigid, soft, and hybrid robots [79].

ent trade-offs between soft and hard robots present designers with a fundamental dilemma: choosing either mobility, force capacity, and autonomy, or adaptability and versatility. To address this dichotomy, researchers have pioneered the concept of hybrid robotics [72], see Fig. 1.5. These systems integrate both soft/flexible and rigid components, enabling the development of robots that combine adaptability with efficient movement capabilities [73–75]. Such hybrid platforms demonstrate remarkable versatility, including the ability to switch between different locomotion modes [76–78]. This approach holds significant promise for developing versatile robotic systems that can perform a wide range of functions.

A key innovation in hybrid robotics involves the implementation of variable-stiffness materials, which can significantly expand a robot's functional capabilities by exhibiting distinct properties and behaviours across different stiffness states [80]. Such controllable variable stiffness can be achieved by combining soft materials, such as silicone, with phase-changing components or smart materials. Shape-memory materials represent one promising approach, offering the ability to maintain temporary deformed shapes and return to their original configuration upon external stimulation [81]. Notable applications include a finger-sized robot utilizing shape memory alloy (SMA) for crawling and climbing on rough surfaces [82], and an SMA-actuated crawling micro-robot [83].

Another effective approach to achieving variable stiffness involves jamming systems [84]. By leveraging jamming and stiffness modulation, Steltz et al. [85] transformed a single-DOF linear actuator into a multiple-DOF bending actuator, successfully developing a worm robot that achieves crawling motion through specialized actuation sequences. The integration of jamming techniques with distributed hardware design enabled multi-functional capabilities in the work by Karimi et al. [86]. Their hybrid robot demonstrates both locomotion and object manipulation capabilities through a novel loop-shaped design, where rigid mobile units are interconnected by a flexible membrane that achieves variable stiffness through particle jamming activated by vacuum pumps.

Hybrid robotics with adaptive morphology emerges as an ideal principle for developing robots capable of both land-based motion and object manipulation. Our motivation for this research lies in the potential of hybrid adaptive robots to bridge the gap between conventional and soft robotics, creating a new class of versatile, universal robots. By developing systems that can transition between rigid and soft states, it becomes possible to address the fundamental limitations of existing robotic paradigms and pave the way for more adaptable multifunctional robots capable of operating effectively across diverse environments and applications.

1.3 Challenges in Integrating Mobility with Manipulation

Designing and developing a robot capable of both land-based motion and object manipulation poses several significant challenges. First of all, since the intended robot is supposed to be compact, it cannot have any additional tools or grippers attached to it. This means that the only viable mechanical option for interacting with external objects would be *full-body grasping*, where the robot uses its own body to envelope objects and subsequently manipulate them. This approach necessitates that the robot should be deformable, possessing adaptive morphology. On the other hand, we also want it to be mobile (on a planar ground) and untethered so that it can freely traverse long distances, which likely requires the integration of conventional hard technologies. We can summarize these **design-related requirements** as follows:

- *Dual functionality within a unified structure:* The robot must seamlessly transition between a locomotion-optimized configuration and a manipulation-capable form while maintaining mechanical integrity, operational stability, and energy efficiency throughout both modes of operation.
- *Integration of opposing stiffness states:* Dual functionality necessitates the robot's ability to achieve and maintain distinct mechanical properties — rigid when mobility is prioritized and flexible when deformation is required for manipulation. The system must sustain each stiffness state reliably for extended operational periods without performance degradation or mechanical fatigue. Crucially, the stiffness transition mechanism must be designed to minimize switching time between states, enabling rapid adaptation to changing task requirements without significant operational delays that would compromise the robot's responsiveness and overall efficiency.
- *Active deformation capabilities:* Effective full-body grasping requires not merely passive flexibility but controlled, actively-actuated deformation. The robot must incorporate actuation mechanisms that enable precise morphological changes while providing sufficient force to manipulate a range of objects.
- *Shape retention and stability:* In its rigid state, the robot must reliably maintain its current configuration against external forces, ensuring consistent locomotion performance and positional accuracy without unwanted deformation or mechanical drift.
- *Self-contained autonomous operation:* All necessary components — including actuation systems, stiffness-modulation mechanisms, power supplies, processing units, and sensing elements — must be fully integrated onboard within strict size and weight constraints while providing sufficient operational endurance.
- *Size and weight constraints:* The system must be compact while incorporating all necessary components for both functions.

Another important issue lie in the actuation and control strategies that enable operation across both intended stiffness states. The actuation method must ensure both efficient mobility when the robot is rigid and precise active deformation when it transitions to a flexible mode. Since closed-loop control is desirable for reliable

performance, we must be able to accurately identify not only the robot's location but also its current stiffness state and morphology.

Morphological computation presents a significant challenge in this context. With a variable shape, we must be able to estimate the robot's configuration at any given time, requiring the integration of distributed sensing systems while maintaining system compactness. This introduces complex trade-offs between sensing capabilities and overall system size.

Finally, control becomes a multi-layered problem with coupled complexities. The stiffness regulation operates in a discrete state space with distinct rigid and flexible modes, while motion and deformation control require continuous dynamic modeling. This necessitates integrating discrete stiffness transitions with continuous motion dynamics within a unified control framework, with the added complexity that the robot's behavioural characteristics may vary significantly between stiffness states. The **actuation and control challenges** can be summarized as follows:

- *Multi-modal actuation requirements:* The actuation system must effectively drive both rigid-body locomotion and compliant morphological changes.
- *State estimation across variable morphology:* Developing sensing strategies that can accurately determine the robot's configuration, position, and stiffness state despite changing physical properties and geometries.
- *Hybrid control architecture:* Creating a control framework that seamlessly integrates discrete state transitions (between stiffness states) with continuous motion control while accounting for changing dynamic properties.
- *Dynamic model adaptation:* Developing models that can adapt to the significant changes in mechanical properties between rigid and flexible states, including potentially nonlinear behaviours in the compliant state.
- *Transition management:* Ensuring smooth, controlled transitions between stiffness states without introducing instabilities or compromising the robot's interaction with its environment.
- *Energy-efficient control strategies:* Implementing control approaches that minimize power consumption during both locomotion and manipulation tasks especially during stiffness transitions.

- *Real-time computation constraints:* Balancing computational complexity and the need for real-time performance on embedded systems with limited processing capabilities.
- *Fault tolerance and robustness:* Developing control strategies that can compensate for potential sensor limitations, actuator uncertainties, and environmental disturbances across variable stiffness states.

Finally, planning presents substantial challenges that encompass both the robot's internal configurations and its interactions with the environment. Planning must address motion and morphology on the robot's state level, as well as navigation, grasping, and manipulation on the functional level. The inclusion of variable stiffness and morphology significantly expands the robot's configuration space, making planning much more complex and potentially computationally prohibitive.

This expanded complexity necessitates the development of sophisticated, unconventional planning methods that effectively balance planning objectives against computational time and resource constraints. Additionally, variable morphology introduces intriguing new capabilities that we wish to explore, particularly for navigation through highly cluttered environments where adaptive deformation becomes essential for obstacle avoidance. The **planning challenges** can be summarized as follows:

- *High-dimensional configuration space:* Planning must account for both conventional position variables and morphological variables, creating a substantially larger search space than traditional robot planning problems.
- *Stiffness state sequencing:* Determining the optimal sequence of stiffness transitions to efficiently accomplish complex tasks that require both locomotion and manipulation capabilities.
- *Deformation planning:* Developing algorithms that can compute optimal body deformations for object grasping and obstacle avoidance while considering physical constraints.
- *Task decomposition across morphologies:* Breaking complex tasks into subtasks that leverage the distinct advantages of each morphological state, with appropriate transitions between stiffness states.

- *Multi-objective optimization:* Balancing competing objectives such as energy efficiency, operation speed, manipulation capability, and mechanical stability throughout planned trajectories.
- *Environmental interaction predictions:* Anticipating how the robot's variable morphology will interact with different environmental features and incorporating these predictions into planning decisions.
- *Computational efficiency:* Developing planning approaches that can operate within the computational constraints of an onboard system while handling the increased complexity of morphological planning.
- *Uncertainty management:* Accounting for uncertainties in state estimation, environmental conditions, and physical interactions, which are amplified by the variable morphology.
- *Planning horizons and hierarchies:* Establishing appropriate planning hierarchies that combine long-term strategic planning with short-term reactive adjustments across both locomotion and manipulation domains.

1.4 Research Objectives

Given the described complex challenges, this research aims to pioneer a new class of mobile multifunctional robots with advanced full-body grasping and manipulation capabilities. This ambitious vision is structured around the following comprehensive research objectives:

- **To design and prototype a hybrid robotic system** that integrates the complementary advantages of traditional hard robotics and flexible technologies, creating a versatile platform capable of efficient land-based mobility, rapid stiffness transitions, and effective full-body grasping across diverse object geometries. This design will balance mechanical robustness, actuation efficiency, and system compactness while maintaining the capacity for both locomotion and manipulation within a unified structure.
- **To develop control and planning methods** that synchronously manage the robot's pose, stiffness state, and morphological configuration throughout operational sequences. This includes implementing coordinated full-body

grasping (approaching objects, transitioning to flexible state, and actively enveloping targets), and creating navigation strategies that leverage the robot's adaptive morphology to traverse cluttered environments and transporting grasped objects to desired locations.

- **To validate the proposed multifunctional design** through systematic experimental evaluation across diverse operational scenarios, establishing quantitative performance metrics for locomotion efficiency, stiffness transition speed, grasping versatility, and manipulation precision. This validation will demonstrate the advantages of our integrated approach compared to conventional single-function systems and establish design principles for future multifunctional robots with variable stiffness capabilities.

1.5 Methodology

In this dissertation, the author presents a comprehensive framework of solutions addressing the stated research objectives through several innovative approaches:

- **Dual Locomotion Unit Architecture:** The robot employs two specialized locomotion units connected by a variable stiffness bridge. Each locomotion unit functions as an autonomous mobile robot with integrated electronics and onboard power, ensuring the system remains untethered throughout operation. The redundant wheel configuration enables planar motion regardless of the robot's overall shape and configuration. Additionally, these units serve a dual purpose by providing active, controlled deformation of the bridge when it transitions to a flexible state, allowing for precise morphological adaptations during object manipulation tasks. This architecture creates a symbiotic relationship between mobility and manipulation functions, with each component contributing to both operational modes.

- **Advanced Variable Stiffness Mechanism:** A sophisticated variable stiffness bridge endows a robot with adaptive morphology and versatile behaviour through the strategic incorporation of low melting-point alloy (LMPA). This material transitions between solid and liquid phases upon controlled heating or cooling relative to its melting point, corresponding directly to the robot's desired stiffness states: liquid LMPA enables flexibility for defor-

mation and full-body grasping, while solid LMPA provides rigidity for efficient locomotion. The bridge features multiple independently controllable segments, increasing the available degrees of freedom for complex shape formation. A novel modular design approach significantly decreases stiffness transition time while maintaining optimal mechanical properties, addressing one of the key challenges in variable stiffness robotics. This mechanism includes real-time stiffness monitoring through non-linear state estimation techniques and a robust finite-state machine framework that manages reliable transitions between stiffness states.

- **Hierarchical Hybrid Control Framework:** The control system integrates stiffness management with motion planning through a unified kinematic model that encompasses both rigid and flexible states. This model is derived from the robot's geometry and incorporates cardioid-based motion patterns of the locomotion units when one or more bridge segments are in a flexible state. The framework implements high-level decision-making algorithms that synchronously coordinate stiffness transitions, locomotion parameters, and morphological adaptations based on environmental conditions and task requirements. Model-predictive control schemes optimize performance in each operational mode, defined by the specific stiffness states of the various bridge segments, enabling smooth transitions between mobility and manipulation functions while maintaining system stability.

- **Advanced Navigation Systems:** Navigation capabilities are enhanced through two complementary motion planning approaches optimized for different environmental conditions. For environments with sparse obstacles that the robot can navigate in its default configuration, a hybrid algorithm combines rapidly exploring random tree (RRT*) with artificial potential field (APF) to efficiently generate optimal paths. When facing highly cluttered environments requiring morphological adaptations, the system employs a sophisticated multi-step Voronoi-based optimization method. This approach identifies narrow passages, determines required morphological configurations, and plans appropriate stiffness transition sequences, enabling the robot to navigate through confined spaces by leveraging its variable morphology. These navigation systems integrate seamlessly with the stiffness control and motion planning components to create a cohesive operational framework.

1.6 Contributions

In this doctoral project, the author has developed a proof-of-concept mobile hybrid robot with variable stiffness and adaptive morphology *from scratch*. This dissertation introduces the full-stack development of the system, including comprehensive robot design and fabrication, mathematical modeling, control system architecture, experimental validation, and practical applications. The author presents five significant contributions that advance the field of multifunctional robotics:

1. Design and fabrication of compact modular units capable of rapid, reversible transitions between rigid and flexible states. These LMPA-based units can be assembled into diverse structures with controllable stiffness and shape, establishing a foundation for adaptive robotic platforms.
2. Development of a hybrid mobile robot that combines conventional mobility with flexible manipulation capabilities. The dual-locomotion platform combined with a special bridge with incorporated variable stiffness modular units demonstrates seamless switching between functioning as an omnidirectional robot for efficient navigation and as a flexible manipulator for complex grasping tasks through coordinated stiffness control.
3. Derivation of a comprehensive hybrid kinematic model that characterizes the robot's behaviour across both rigid and flexible states. This unified model identifies four distinct locomotion modes emerging from the robot's variable stiffness and morphological adaptability.
4. Implementation of an Model Predictive Control (MPC)-based decision-making framework that optimizes real-time mode switching based on environmental conditions and task requirements. This controller simultaneously manages the robot's motion parameters and morphological reconfiguration while maintaining system stability throughout operational modes.
5. Creation of motion planning and optimal control algorithms that enable full-body grasping of arbitrarily shaped objects and navigation through highly cluttered environments. These algorithms strategically modify the robot's stiffness and shape to perform manipulation tasks and traverse confined spaces inaccessible to conventional rigid platforms.

The concerning results have been partially submitted to several peer-reviewed journals and peer-reviewed conference proceedings, as listed in Appendix A.

1.7 Outline

This dissertation is organized as follows:

Chapter 1 introduces the research context, highlights limitations of conventional hard robots, presents the concept of adaptive morphology, identifies key challenges in developing multifunctional machines, and establishes the research objectives, utilized methodology, and contributions.

Chapter 2 reviews state-of-the-art morphologically adaptive systems and variable stiffness technologies, analyzing current approaches and identifying opportunities for advancement in versatile robot development.

Chapter 3 details the design and fabrication methodology of our hybrid mobile robot with variable morphology, comparing unitary versus modular approaches while providing guidelines for system customization across diverse applications.

Chapter 4 describes the stiffness control mechanisms, including thermal management systems, state estimation techniques, and finite-state machine implementation for robust transitions between rigid and flexible states.

Chapter 5 establishes a hybrid kinematic framework encompassing both rigid and flexible states, analyzes four distinct locomotion modes, and presents the hierarchical MPC strategies for optimal stiffness transitions and motion control.

Chapter 6 explores the robot's manipulation capabilities, detailing control strategies for full-body grasping of objects with arbitrary geometries and their transport to target locations.

Chapter 7 presents advanced navigation strategies, including a hybrid RRT*-APF algorithm and a multi-step Voronoi-based optimization method for efficient planning with adaptive shape deformation in cluttered environments.

Chapter 8 summarizes key contributions, validates the initial claims, and outlines promising directions for future research and applications.

Chapter 2

Related Work

2.1 Adaptive Morphology in Robotics

The concept of adaptive morphology has emerged as a groundbreaking principle in robotics, drawing inspiration from nature's diverse solutions to locomotion [87–89] and environmental adaptation. This approach leverages the interplay between form and function, recognizing that an organism's or robot's physical structure significantly influences its behavioural and locomotion strategies. Recent research has demonstrated that adaptive morphological changes can not only enhance dynamic performance by mitigating tradeoffs during locomotion but also introduce novel functionalities [37].

This biological inspiration stems from numerous examples in nature, where organisms demonstrate remarkable abilities to alter their physical form to adapt to changing environments. From the way octopuses can modify their body shape to squeeze through tight spaces [90], to how cats adjust their posture for different types of movement [91], these natural adaptations have provided valuable insights for robotic design. The implementation of such principles in robotics represents a significant shift from traditional hard designs toward more adaptive systems.

The rise of adaptive morphology in robotics has been facilitated by advancements in materials science and engineering, particularly the development of soft, variable-stiffness, and functional materials and structures. These innovations have opened new avenues for creating robots that can alter their physical form to meet varying

environmental demands and task requirements. The ability to adapt morphology presents several key advantages:

- **Enhanced Versatility**: Robots with adaptive morphology can effectively navigate diverse terrains and transition between different substrates, accommodating opposing dynamic requirements such as maneuverability, stability, efficiency, and speed.
- **Multifunctionality**: Morphological adaptation enables robots to reconfigure their shape on-the-fly, potentially serving multiple purposes without the need for separate, specialized machines.
- **Improved Efficiency**: By altering their form to suit specific tasks or environments, adaptive robots can optimize their energy consumption and performance.
- **Increased Safety**: Soft and morphing structures can enhance human-robot interaction safety, making these robots more suitable for collaborative environments.

The field of terrestrial robotics [92] has witnessed remarkable advancements in adaptive morphology implementation. A groundbreaking example is the Whegs series, which ingeniously incorporates principles from insect locomotion to develop highly mobile robots with hybrid leg-wheel appendages [93]. Through systematic design evolution, the Whegs platform has significantly improved its capability to traverse challenging terrain through passive morphological adaptations. A key innovation in recent models is the integration of a passive body flexion joint, directly inspired by cockroach biomechanics [94]. This joint enables the robot's front section to flex downward during obstacle encounters, effectively preventing the robot from becoming stranded during climbing sequences - a common problem known as high-centering [95].

The success of the Whegs design prompted further innovations in adaptive locomotion systems. Kim et al. [96] advanced this concept by developing a sophisticated robot featuring wheels with passive morphological adaptation capabilities, as illustrated in Fig. 2.1(a). These innovative wheels exhibit dual functionality: maintaining their circular geometry for efficient rolling on smooth surfaces while automatically transforming into leg-like structures when encountering obstacles.

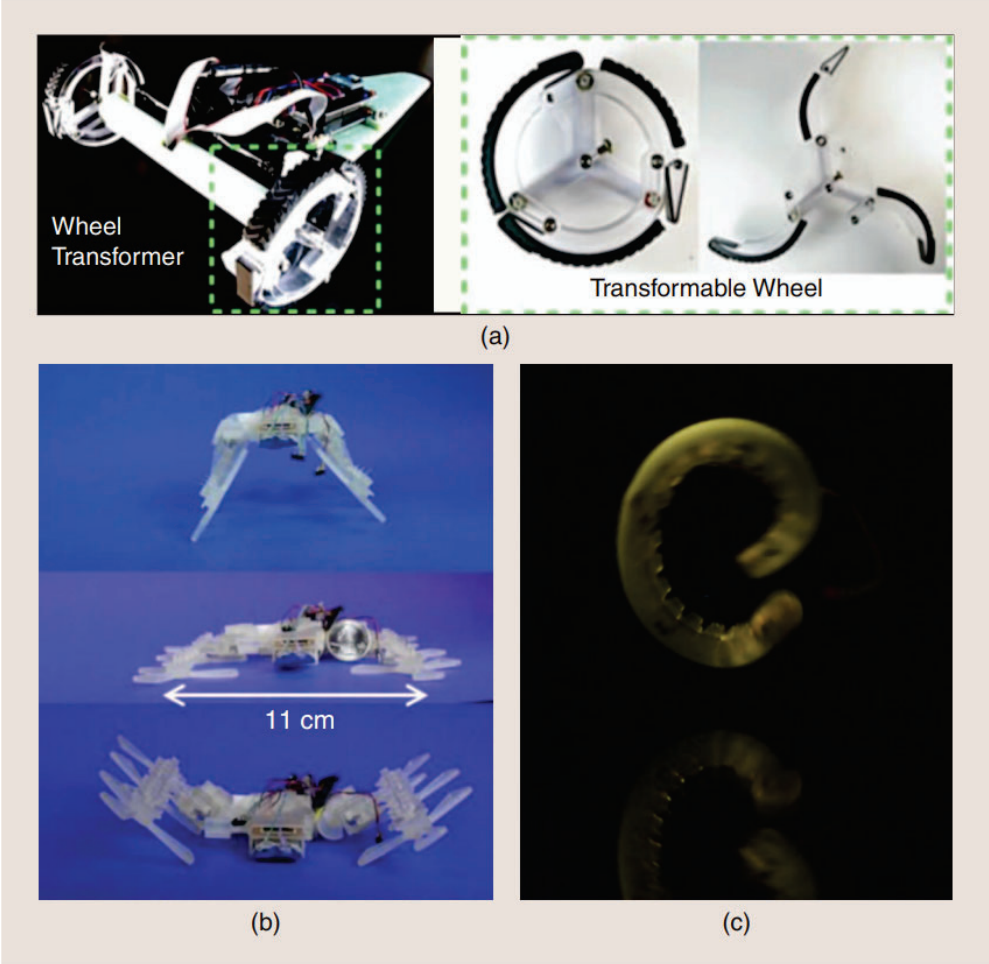

Figure 2.1: Innovative terrestrial robots demonstrating adaptive morphology: (a) Adaptive wheel-leg robot featuring morphing wheels that transform to overcome obstacles [96]; (b) STAR platform showcasing adjustable sprawl angles for optimized vertical and planar movement [97]; (c) Bio-inspired GoQBot exhibiting dynamic rolling configuration transformation [75].

This intelligent design approach effectively addresses the traditional performance trade-offs associated with different terrain types. The robot achieves optimal energy efficiency during flat-surface locomotion through conventional wheel rotation, while seamlessly transitioning to more aggressive leg-like movements when navigating challenging obstacles. This adaptive mechanism represents a significant advancement in creating versatile mobile robots capable of efficiently operating across diverse environmental conditions.

The implementation of passive adaptation mechanisms in both the Whegs series and Kim's design demonstrates a crucial principle in adaptive morphology: the ability to achieve complex behavioural changes through relatively simple mechani-

cal solutions. These systems respond to environmental interactions without requiring complex sensing or control systems, offering a robust and reliable approach to adaptive locomotion. This passive adaptation strategy has proven particularly effective in scenarios where rapid response to terrain changes is essential, and where the added complexity of active control systems might be disadvantageous.

Building upon the Whegs concept, Kim et al. [96] developed a robot with wheels capable of passive morphological changes, see Fig. 2.1(a). These wheels maintain a circular shape on flat surfaces but can transform into leg-like structures when encountering obstacles. This adaptive design minimizes performance trade-offs across varying terrain types, enabling efficient movement on flat surfaces while maintaining the ability to navigate rough terrain effectively.

The development of adaptive locomotion systems has continued to accelerate through innovative design approaches. She et al. [98] pioneered the integration of advanced manufacturing techniques with adaptive morphology, developing a sophisticated platform featuring additively manufactured wheels capable of active transformation into articulated leg structures. This advancement in fabrication methodology enabled complex geometric transformations while maintaining structural integrity. In parallel, the Quattroped system [99] demonstrated a novel approach to hybrid mobility, incorporating four independently actuated wheel-leg units that seamlessly transition between rolling and walking configurations, representing a significant advancement in reconfigurable locomotion systems.

The RHex platform [100] presents another breakthrough in bio-inspired robotics, drawing upon cockroach locomotion principles to create a highly versatile mobile system. Its distinctive design features six synchronized, compliant rotating legs that generate efficient propulsion across challenging terrain. The platform's evolution has produced several sophisticated variants, each introducing novel morphological adaptations. The Sprawl-Hex [101] and its successor, the STAR platform [97], illustrated in Fig. 2.1(b), showcase an innovative approach to locomotion through variable geometry. These systems incorporate dynamically adjustable sprawl angles, enabling a remarkable range of locomotion capabilities. During low-sprawl configurations, the robots achieve stability and forward velocity metrics comparable to traditional wheeled platforms. Conversely, high-sprawl configurations enhance traction and obstacle negotiation capabilities through increased

ground clearance and improved leg engagement. This geometric adaptability extends to confined space navigation, where minimal sprawl angles enable the robot to significantly reduce its vertical profile.

Building upon the RHex architecture, Galloway et al. [102] introduced an innovative variable compliance mechanism in the leg design. This advancement enabled dynamic adjustment of leg stiffness, allowing the robot to optimize its mechanical impedance based on terrain characteristics and locomotion requirements. In a dramatic departure from these designs, the GoQBot [75] demonstrates an extreme implementation of morphological adaptation inspired by caterpillar mechanics [103]. This unique platform combines a flexible silicone body structure with strategically positioned shape-memory alloy (SMA) actuators, enabling dramatic morphological transformations. The robot can rapidly reconfigure from an elongated, serpentine form into a compact, wheel-like configuration, as shown in Fig. 2.1(c). This transformation facilitates a distinctive ballistic rolling locomotion mode, representing a novel approach to achieving high-speed movement through extreme morphological adaptation.

These examples underscore the potential of adaptive morphology to revolutionize mobile robotics. By incorporating soft technologies and leveraging advanced manufacturing processes, engineers can create more flexible, efficient, and adaptable robotic systems. The future of adaptive morphology in robotics holds promise for:

- Intelligent machines that can dynamically balance conflicting locomotion requirements.
- Multifunctional robots capable of on-the-fly reconfiguration.
- Soft wearable robots that adapt to user needs and environmental conditions.
- Exploration robots that can navigate and adapt to unknown terrains.

As research in this field progresses, we can anticipate the development of increasingly sophisticated adaptive robots that blur the lines between rigid and soft structures, potentially leading to a new paradigm in robotic design.

2.2 Variable-Stiffness Mechanisms and Control

The advancement of robotic systems capable of safe and effective interaction within complex, unstructured environments has driven significant research into stiffness modulation techniques [104–106]. These approaches are fundamental to enhancing compliance and adaptability in soft robotics, offering solutions that bridge the gap between rigid and soft structural elements. The following overview examines the most prominent thermally-actuated materials that have demonstrated particular promise in robotics applications.

Thermally Actuated Materials have emerged as a versatile solution for achieving variable stiffness properties:

- **Wax-based composites**: These innovative materials [107–109] exhibit remarkable stiffness variability, ranging from several kilopascals to approximately 1 MPa through thermal modulation 2.2(a). Particularly noteworthy are wax-impregnated polyurethane foams and additively manufactured lattice structures, which exhibit exceptional characteristics including substantial modifications in volume, morphology, and elastic modulus across accessible temperature ranges. A distinctive advantage of these composites is their inherent self-healing capability, which enhances their durability and operational lifespan [110].

- **Thermoplastic-polycaprolactone (PCL)**: Recent experimental investigations have revealed PCL's [111, 112] remarkable transformation capabilities, demonstrating a transition from a rigid state with a Young's modulus of 190 MPa to a compliant state measuring 2.2 MPa when heated from ambient temperature (20°C) to 50°C 2.2(b). This property has been successfully implemented in robotic manipulation, enabling three-fingered grippers to execute precise grasp-and-hold operations while achieving passive mechanical locking without continuous energy input [113].

- **Polyethylene terephthalate (PET)**: This material [114–116] exhibits distinct phase transitions, characterized by a glass transition temperature range of approximately 65°C to 70°C, with full transition to a rubbery state occurring around 80°C. Advanced variable stiffness mechanisms incorporating PET medical tubing, combined with internal stainless-steel heating elements,

have demonstrated remarkable stiffness modulation capabilities. These systems achieve stiffness variations of up to 47-fold, spanning from 0.47 MPa to 22.22 MPa 2.2(c), representing a significant advancement in controllable compliance [117].

The implementation of these thermally-actuated materials in robotic systems represents a significant advancement in achieving controllable, variable stiffness properties. Their ability to undergo substantial mechanical property changes in response to thermal stimuli provides engineers with powerful tools for developing adaptive and responsive robotic structures. These materials enable the creation of systems that can dynamically modify their mechanical characteristics to meet varying task requirements and environmental conditions.

Smart Materials [118, 119] have revolutionized variable stiffness applications through their unique phase-change properties and significant mechanical transformations:

- **Shape Memory Polymers (SMP):** These smart materials can memorize a permanent shape, be deformed and fixed into a temporary shape, and then recover their original form when exposed to an external stimulus such as heat, light, or chemical triggers [120–122] SMP's combine the structural properties of conventional polymers with the ability to undergo controlled, reversible transformations between different configurations, making them valuable for applications ranging from biomedical devices to aerospace structures. Their integration in robotic hand design has achieved remarkable stiffness modulation capabilities, demonstrating enhancement ratios exceeding 120-fold when thermally activated between room temperature (25°C) and 70°C 2.2(d). This significant property variation maintains essential flexibility characteristics, enabling precise manipulation tasks while providing structural rigidity when required. The implementation has proven particularly effective in adaptive gripping applications, where variable compliance is crucial for handling diverse objects [123].

- **SMP-metal composites:** These advanced hybrid materials [124,125] represent a breakthrough in variable stiffness technology, achieving an exceptional rigid-to-soft modulus ratio of approximately 1500:1. The incorporation of metallic particulates serves a dual purpose: enhancing the material's rigid-

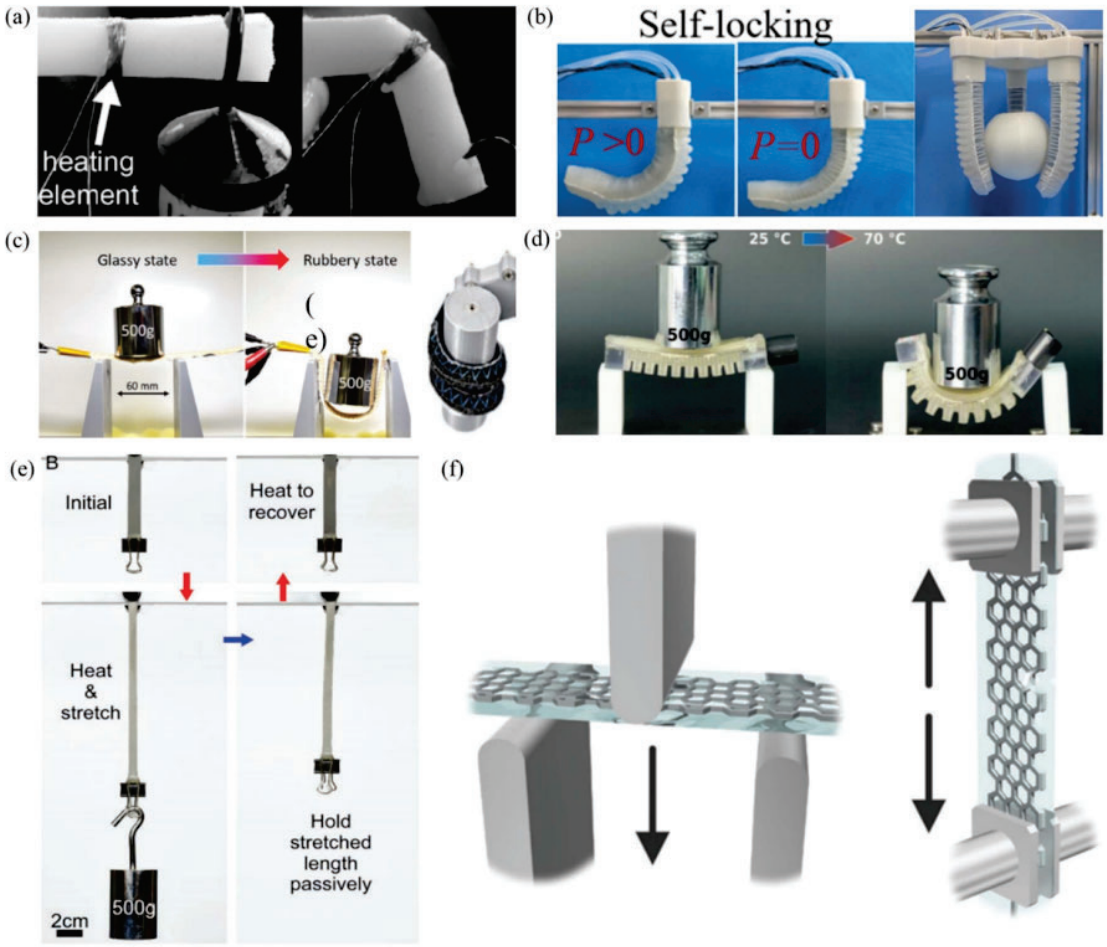

Figure 2.2: Variable stiffness mechanisms: (a) Wax; (b) Thermoplastic-polycaprolactone (PCL); (c) Polyethylene terephthalate (PET); (d) Shape memory polymers (SMP); (e) SMP composites with metal; (f) Hydrogel composites with metal.

state stiffness at lower temperatures while simultaneously reducing the composite's hot-state stiffness when the metallic components transition to their melted state 2.2(e). This dramatic stiffness variation enables unprecedented levels of mechanical adaptability in robotic applications.

- **Low-melting-point alloys (LMPAs):** These innovative materials exhibit remarkable phase transition properties, transforming from solid to liquid states within a narrow temperature range $< 400°C$ [126–128]. In their solid state, LMPAs demonstrate impressive mechanical properties with stiffness values exceeding 1.4 GPa [129]. When incorporated into hydrogel composite structures, these materials enable dramatic and reversible stiffness modu-

lation through controlled solid-liquid phase transitions 2.2(f). This property has been particularly well-demonstrated in composite systems where the LMPA components provide structural support in their solid state while enabling complete compliance when liquefied [130].

The integration of these smart materials into robotic systems represents a significant advancement in achieving controllable mechanical properties. Their ability to undergo dramatic property changes in response to thermal stimuli provides designers with powerful tools for developing highly adaptive structures. These materials enable the creation of robotic systems that can dynamically modify their mechanical characteristics across several orders of magnitude, adapting to diverse task requirements while maintaining structural integrity. The combination of high stiffness ratios and controllable transition temperatures makes these materials particularly suitable for applications requiring precise modulation of mechanical properties, from soft robotics to adaptive manipulation systems.

Magnetic/Electric Field-Based Approaches have emerged as dynamic solutions for real-time stiffness modulation:

- **MR fluid-based gripper**: Magnetorheological fluid systems [131,132] show remarkable versatility in robotic manipulation tasks. In their default low-viscosity state, these systems excel at conforming to and carefully handling delicate objects with irregular geometries. Upon magnetic field application, they undergo rapid transformation to a rigid state, enabling secure grip of substantial loads. Advanced implementations in multijoint manipulator systems have achieved elastic modulus enhancement ratios of approximately 5.3 under controlled magnetic field conditions. This adaptive behaviour enables a single system to handle both precision manipulation and high-load tasks effectively.

- **ER fluid-based actuators**: These kind of actuators utilize special fluids that rapidly and reversibly transform from liquid to solid-like states when exposed to electric fields, enabling precise, fast-responding, and voltage-controlled mechanical systems with minimal moving parts [133–135]. Electrorheological fluid integration in soft pneumatic systems has yielded significant improvements in manipulation performance. Comparative analysis shows these systems achieve a 62.3% reduction in vibration amplitude and

a 48.3% decrease in decay time relative to conventional pneumatic actuators [113]. In specialized applications such as flexible fin designs, ER fluid systems demonstrate stiffness modulation ratios of 1.86 when subjected to electric field strengths ranging from zero to 1.5×10^6 V m^{-1}. This capability enables precise control over system dynamics and improved operational stability.

Solid Structures and Soft Materials represent another frontier in variable stiffness technology:

- **Electrostatic attraction-based soft finger**: These innovative systems achieve substantial bending stiffness variation through electrostatically induced friction mechanisms [136, 137]. Multilayer designs incorporating dielectric elastomer (DE) units demonstrate remarkable stiffness modulation capabilities, achieving variation ratios of approximately 39-fold under controlled electric field conditions. This significant range of adjustment enables precise control over manipulation tasks requiring varying degrees of compliance and force application.

- **Polyvinyl chloride (PVC) gel actuator**: These systems exhibit sophisticated stiffness modulation capabilities influenced by multiple parameters including DC field intensity, DBA40 weight ratio, gel thickness, and anode mesh characteristics [138–140]. Advanced implementations utilizing 15-layer configurations demonstrate impressive stiffness ranges, transitioning from 20 kPa at zero field strength to 240 kPa at 1200 V m^{-1}, achieving a stiffness modification ratio (ω) of 11. This tunability enables precise control over mechanical properties in response to varying operational requirements.

While each of these approaches presents unique advantages in achieving variable stiffness properties, they also face distinct challenges that warrant ongoing research attention. The selection of an appropriate mechanism depends heavily on specific application requirements, including response time, power consumption, operational environment, and required stiffness range. Future developments in these technologies will likely focus on addressing current limitations while expanding their practical applications in soft robotics.

Key areas for future investigation include:

- Enhancing response times and control precision
- Reducing power consumption and improving efficiency
- Expanding operational temperature ranges
- Developing more robust and durable implementations
- Improving integration methods with existing robotic systems
- Addressing scalability challenges for different applications.

Summary

Variable stiffness mechanisms have evolved significantly through diverse technological approaches. Thermally actuated materials include wax-based composites that exhibit stiffness variations from kilopascals to 1 MPa, thermoplastic-polycaprolactone that transitions from 190 MPa to 2.2 MPa when heated, and polyethylene terephthalate systems that achieve 47-fold stiffness variations (0.47-22.22 MPa). Smart materials show even more impressive capabilities, with shape memory polymers demonstrating 120-fold stiffness enhancement and SMP-metal composites achieving exceptional 1500:1 rigid-to-soft ratios. Low melting point alloys offer remarkable phase transitions with solid-state stiffness exceeding 1.4 GPa. Field-responsive systems include magnetorheological fluids with 5.3× modulus enhancement and electrorheological actuators that provide precise, rapid-response stiffness control.

We conducted a comprehensive comparison of the most well-established variable stiffness technologies, evaluating their performance across five critical parameters: relative stiffness changes, number of distinct absolute stiffness states, transition speed, complexity of untethered design implementation, and fabrication complexity, see Table 2.1. The analysis revealed significant trade-offs among these technologies. Shape memory alloys offer modest stiffness changes with medium transition speeds, though they benefit from simple fabrication and implementation. Shape memory polymers deliver high stiffness variation but with slow transition dynamics and challenging fabrication processes. Jamming-based systems provide high stiffness changes with impressive response times but present substantial challenges for untethered applications due to their pneumatic requirements. Low melting point

alloys demonstrated superior overall performance with their combination of high stiffness variation (solid-state stiffness exceeding 1.4 GPa), the greatest number of distinct stiffness states (4), reasonable transition speeds, and remarkably low complexity in both untethered implementation and fabrication processes.

	Relative stiffness changes	Distinct absolute stiffness states	Speed of stiffness transitions	Complexity of untethered design	Complexity of fabrication
SMA	Low	1	Medium	Low	Low
SMP	High	2	Slow	Medium	High
Jamming	High	3	Fast	High	Medium
LMPA	High	4	Medium	Low	Low

Table 2.1: Comparison of variable stiffness technologies.

Based on this comparison, LMPA's provide the best overall trade-off among the technologies evaluated. Its advantages make LMPA the optimal choice for our robot's design, balancing performance capabilities with practical implementation considerations. The combination of significant stiffness modulation, multiple discrete states, reasonable transition times, and straightforward fabrication process establishes LMPA as the most suitable variable stiffness technology for the proposed robotic application.

Chapter 3

Design and Fabrication of 2SR Robot

In this chapter, we delve into the design and fabrication of a mobile robot with variable stiffness (VS) and adaptive morphology, which we refer to as the *2SR (Self-Reconfigurable Soft-Rigid) robot*. This innovative design approach is not limited to a single robot but represents a *new class of robots* with unique features and functions. The 2SR robot is equipped with components and mechanisms that enable it to transition between rigid and flexible states, significantly enhancing its performance and capabilities. These capabilities, such as shape fitting, grasping, and manipulating objects using the robot's body, will be explored in detail later in this chapter.

When in its rigid state, the 2SR robot can navigate a planar substrate like a conventional omni-robot. Conversely, in a flexible state, it can adapt its shape similarly to soft manipulators, allowing for a diverse range of applications. We will discuss the design features, operational principles, and fabrication procedures employed to bring this versatile robot to life.

We derived two versions of the robot's design, with the first one serving as a proof of concept to test its performance and capabilities. Following this, we introduced the concept of modularity at several levels, which enhanced the robot's performance and robustness to failure as well as provided significant design flexibility. This modular approach allows for numerous variations of the robot, tailored

to meet specific requirements. The modular structure used in the 2SR robot can be also applied to other fields beyond mobile robotics, as the modular units can be assembled into different materials and structures with variable stiffness and shape. Compared to the initial design, the modular version demonstrated faster stiffness transitions, higher resistance to failure, more economical use of materials, and easier fabrication.

The following chapter details the 2SR robot's design and fabrication, including:

1. Methods and mechanisms selected to implement adaptive behaviour.
2. Materials and hardware components used.
3. Fabrication processes and techniques.
4. Guidelines for adapting the 2SR design approach to other applications.

By the end of this chapter, readers will understand the philosophy of the 2SR robot's design, its key components, and fabrication methods. This knowledge will provide context for the subsequent chapters on kinematics, control, and practical applications of a 2SR robot.

3.1 Conceptual Design of 2SR Robot

Modern mobile robots have shown significant advancements over the years, particularly in control strategies, localization, and navigation. However, they are fundamentally limited by their hardware design, which primarily focuses on the ability to traverse long distances quickly and accurately. This capability has been instrumental in transitioning mobile robots from laboratory settings to real-world applications, such as managing warehouses and delivering goods. Despite these successes, current design approaches have inherent limitations that restrict their potential. These limitations can be summarized as follows:

- *Limited Locomotion Modes*: Robots typically exhibit only one mode of locomotion, which restricts their versatility in various environments.
- *Inability to Adapt to Changing/Cluttered Environments*: Robots often struggle to navigate and operate in dynamic or cluttered settings.

- *Minimal Interaction with Surroundings*: Robots generally have limited means of interacting with their environment and often require external equipment to do so.

These challenges have shaped the *primary goal* of this research: to design a mobile robot with enhanced adaptive skills and the ability to interact with other objects without additional instruments. Before commencing the design process, the following conditions and prerequisites were established to guide the development of a 2SR robot:

- **Preservation of Conventional Mobile Robot Features**:
  - Efficient planar mobility
  - Complete autonomy with onboard power and processing
  - Precise motion control across operational modes
- **Enhancement of Adaptive Features**:
  - Real-time morphological reconfiguration
  - Reversible reshaping with consistent performance across multiple cycles
  - Stable maintenance of adopted configurations for extended periods
  - Retention of omnidirectional movement capabilities regardless of shape

Existing design strategies in robotics often present mutually exclusive features. Traditional hard robotics excel in mobility, autonomy, and precision but lack adaptability. On the other hand, soft robotics offers excellent adaptability but faces significant challenges, such as the lack of sophisticated flexible sensors and electronics to make soft robots self-contained. Soft robots often require bulky external actuators, which compromise their mobility. Additionally, they tend to be slow and complex in terms of modeling and control.

Therefore, the development of a *hybrid robot* that combines the advantages of both rigid and soft robotics while eliminating their drawbacks is essential. The main challenge lies in integrating these two concepts to create a robot that maintains the mobility, autonomy, and precision of rigid robots while incorporating the adaptability and interaction capabilities of soft robots.

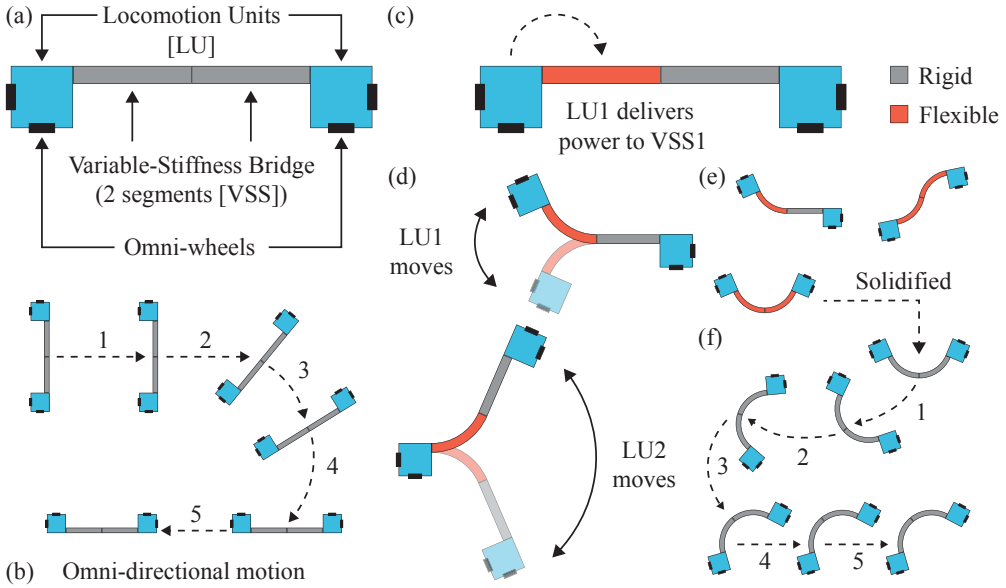

Figure 3.1: Conceptual design of a 2SR robot: (a) Schematic representation of a 2SR robot in its default configuration (rigid state, straight variable-stiffness segments[VSS]). (b) Omni-directional motion in a rigid state. (c) Transition of one VSS into a flexible state. (d) Example deformation with either locomotion unit (LU) as an actuator. (e) Various altered shapes achievable by the 2SR robot. (f) Omni-directional motion of a robot in the new solidified configuration.

To address these challenges and achieve *multifunctionality*, we propose a novel 2SR robot design comprising two *Locomotion Units* (LU) connected by a *Variable Stiffness Bridge* (VSB), as shown in Fig. 3.1(a). Each locomotion unit operates as a self-contained mobile robot with two omni-wheels and integrated electronics and power systems on-board. The central innovation is the variable stiffness bridge, which incorporates phase-changing materials to transition between rigid and flexible states. The VSB can be divided into independently controllable variable stiffness segments (VSS), with the basic configuration featuring two segments, each connected to its adjacent LU both mechanically and electrically.

When the VSB is rigid, the entire system functions as a conventional omni-directional mobile robot (Fig. 3.1(b)). The bridge itself lacks active actuators; instead, the coordinated movement of the LUs defines the shape of a flexible VSB (Fig. 3.1(c)(d)). To transition a specific VS segment to a flexible state, its corresponding LU delivers power and control signals, enabling controlled deformation. Once the desired configuration is achieved, the VSB can resolidify, maintaining the new shape (Fig. 3.1(e)). The strategic placement of two omni-wheels on adjacent

sides of each locomotion unit ensures the robot maintains omnidirectional mobility regardless of its current configuration (Fig. 3.1(f)). This reshaping process can be repeated multiple times without significant material fatigue.

This design effectively satisfies our established requirements: self-contained locomotion units provide autonomy, mobility, and precise motion control, while the variable-stiffness bridge serves as a passive shape-altering element, enabling real-time adaptability. The modular architecture allows for customization according to specific application needs, including variations in segment length and quantity. For proof-of-concept, we implemented a bridge with two independently controlled segments, where each LU manages its adjacent segment's stiffness transitions while both units collectively determine the shape of any flexible segment through coordinated movement.

3.2 Structure of Locomotion Units

The 2SR robot's mobility and actuation heavily rely on its locomotion units. These LUs are engineered as compact, autonomous, non-holonomic robotic modules, each measuring 47 × 47 × 75.5 mm. Their characteristics are crucial to the overall performance and versatility of a 2SR robot.

Each LU features two custom-designed omni-wheels (10 mm radius) positioned on adjacent sides and oriented outwards. This configuration creates a diagonal velocity vector that passes between the wheels. A castor wheel completes a stable triangular base, while internal steel reinforcements enhance structural integrity and ensure consistent ground contact.

This strategic wheel arrangement serves two purposes: when the bridge is flexible, the LUs can precisely deform it into desired shape (Fig. 3.1(d)). Conversely, when the bridge is rigid, the LUs and bridge collectively form a traditional omnidirectional robot. This configuration preserves three degrees of freedom, irrespective of the bridge's shape, allowing for versatile movement across planar surfaces.

Each LU is equipped with a suite of components to enable autonomous operation and precise control, see Fig. 3.2(c):

- **AS5600 encoders** for wheels' position and rotation sensing

- **Li-ion battery** (3.7V, 1000mAh) with voltage boost to 9.6V
- **STM32-based controller** for real-time processing and decision-making

The STM32 controller manages multiple critical functions:

1. Driving brushless DC motors for wheel actuation
2. Controlling phase transitions in the adjacent bridge segment
3. Exchanging control commands and state information with the ground server

To facilitate coordination and higher-level control, each LU is fitted with a wireless serial board. This enables seamless communication with the ground serverr, allowing for complex, synchronized movements and operations of the entire 2SR robot system.

The integration of these components results in locomotion unots that are not only capable of independent movement but also work in tandem to manipulate the variable stiffness bridge, thereby enabling the unique rigid-flexible transitions that characterize a 2SR robot.

3.3 Rigid-Flexible Transitioning Mechanism

As discussed in Related Work (Chapter 2), various methods for implementing controllable stiffness have been explored in the research field. These methods include the use of electro-rheological and magneto-rheological fluids, shape memory polymers (SMPs), and low melting point alloys (LMPAs).

In selecting the appropriate technology for our application, we focused on the requirement for only two distinct stiffness states: *rigid* and *flexible*. In the rigid state, the material must be sufficiently stiff to maintain its shape while the locomotion units are active. Conversely, in the flexible state, the structure must be deformable enough, with minimal or no restoring force, to allow the LUs to easily deform the bridge. In addition, the stiffness transitions should be as rapid as possible to allow the robot to respond immediately to environmental changes.

After careful consideration, we selected LMPAs for the following reasons:

- *Magneto-rheological fluids* rely on external high-voltage activators and continuous energy consumption to maintain a solid state. Given that the rigid state is the default and is expected to occur more frequently than the soft state, this would be inefficient.
- *Shape memory polymers* have relatively slow phase transitions due to their low thermal conductivity, making them less suitable for applications requiring fast responsiveness.
- *LMPAs* possess higher thermal conductivity compared to the other materials mentioned, allowing them to undergo phase transitions much faster.
- *LMPAs* are significantly stiffer than magneto-rheological fluids and SMPs when in their solid state ([141–143]), providing the necessary rigidity for our application.

LMPAs exhibit two phases: solid and liquid. At room temperature, they are typically in a solid state. External or direct heating can be used to melt them, transitioning them to a liquid state. For our purposes, we adopted the approach introduced in [144, 145]. They developed a variable stiffness fiber composed of an LMPA core, a tubular encapsulation made of silicone rubber, and a conductive wire used as a heater to melt the alloy. Their research demonstrated that such fiber could become over 700 times softer and over 400 times more deformable when heated above the LMPA melting temperature. The bridge returns to a solid state by cooling down the alloy. Thus, the VS fiber is rigid when the LMPA is solid and flexible when the alloy is liquid. The compliance of the fiber when the alloy is liquid is defined by the properties of the encapsulating silicone layer.

3.4 VSB: Monolithic Approach

Our initial design for the 2SR robot's variable stiffness bridge consisted of two distinct segments (VSS), with each adjacent to one of the locomotion units. This design choice was driven by the presence of two locomotion units (LUs), allowing each LU to control its adjacent segment. This configuration provides the robot with greater degrees of freedom and a wider range of achievable shapes, while maintaining a manageable level of complexity in both control and fabrication.

In our first implementation, we adopted what we term a *monolithic approach*, where each VS segment was conceived as a single, unified component that could be connected to another segment to form a complete bridge. This approach featured an integrated design where the stiffness-changing mechanism, structural elements, and thermal management systems were combined within a single structure.

The monolithic design offered several potential advantages:

- Structural integrity through continuous construction
- Uniform thermal distribution throughout each segment
- Reduced complexity in the initial control architecture

However, as our research progressed, we identified several limitations inherent in this approach that prompted our transition to a *modular approach*, where each segment comprises multiple smaller, interchangeable units. This evolutionary step in our design philosophy represented a fundamental shift in how we conceptualized and implemented variable stiffness mechanisms.

The following sections provide a comprehensive analysis of both approaches, detailing the technical specifications, performance characteristics, and design trade-offs that informed our ultimate decision to adopt a modular architecture for enhanced functionality and performance.

3.4.1 General Structure and Components

Figure 3.2(a) illustrates the variable stiffness bridge and its internal architecture. Each bridge segment is fabricated as an independent unit and then assembled into a complete structure using two specialized connection systems:

1. **VSS-to-VSS clamps** join adjacent segments, ensuring structural integrity at intersegmental junctions.
2. **LU-to-VSS clamps** secure segments to locomotion units, providing both mechanical stability and electrical connectivity.

Within the non-deformable region concealed by the LU-to-VSS clamp, we incorporate plastic fillers. They serve dual purposes: containing the phase-change alloy

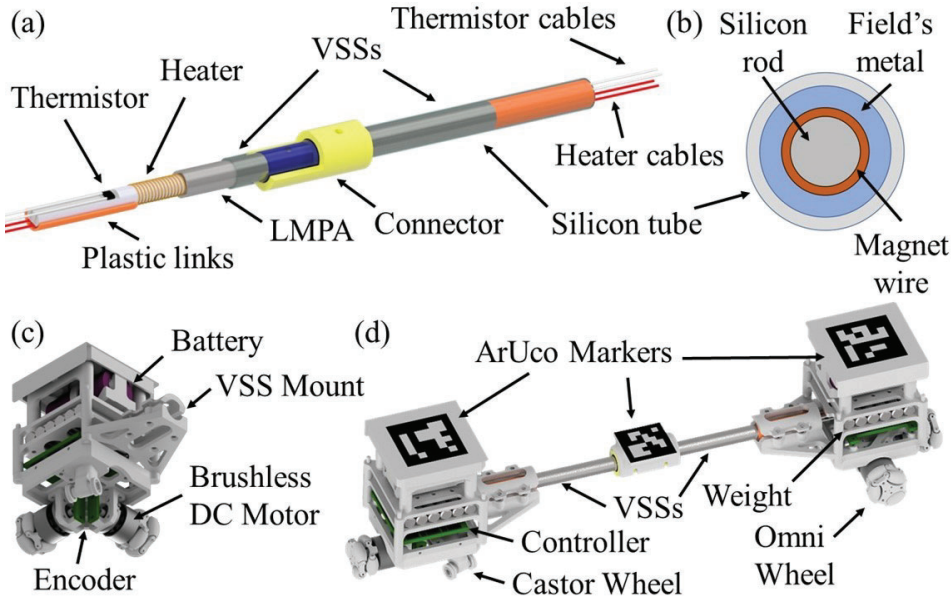

Figure 3.2: Variable stiffness bridge (VSB) with two segments: (a) Perspective view; (b) Cross-sectional view. (c) Locomotion unit (LU). (b) Assembled 2SRA.

within its designated chamber and protecting embedded sensors and wiring from mechanical stress and environmental exposure.

Each VSS features a sophisticated multi-layered construction (Fig. 3.2(b)) engineered to achieve controlled variable stiffness:

- **Silicone Rod** (5 mm diameter): Functions as the structural core and scaffold for subsequent layers.
- **Enameled Wire**: Precision-wound heating element that delivers uniform thermal energy to the phase-change material.
- **Silicone Tube** (7 mm internal diameter, 1 mm wall thickness): Provides thermal insulation and hermetic containment for the liquid-state alloy.
- **Low Melting Point Alloy**: Phase-change material distributed within the annular cavity.
- **NTC Thermistor**: High-precision temperature sensor for closed-loop thermal regulation.

The *active region* of each segment (containing LMPA) extends 40 mm, while each connector spans 30 mm, resulting in a total bridge length of 170 mm. These

dimensional parameters were established through rigorous analysis of several interdependent factors and finding trade-off between them:

1. *Operational Range vs. Material Efficiency*: Optimizing segment dimensions requires balancing increased workspace (favoring longer segments) against material consumption and weight considerations.

2. *Energy Consumption and Thermal Dynamics*: The volume of LMPA directly impacts power requirements and phase-transition response times. Larger volumes (in long and wide segments) necessitate greater heating capacity and exhibit longer thermal equilibration periods.

3. *Actuation Force Requirements*: Segment length critically influences the force required for deformation. According to beam theory, the actuation force (F) scales inversely with the cube of segment length (L):

$$F = \frac{3EI\delta}{L^3}, \tag{3.1}$$

   where E is Young's modulus of the material, I is the area moment of inertia of the beam's cross-section, and δ is the beam's deflection. This means that shorter segments require bigger bending force from LUs.

4. *Fabrication Constraints*: The minimum achievable thickness of the LMPA layer is fundamentally limited by fluid mechanics phenomena. As the annular gap narrows, capillary forces increasingly impede uniform alloy distribution. This relationship is quantified by the Young-Laplace equation:

$$\Delta P = \frac{2\gamma}{r}, \tag{3.2}$$

   where ΔP represents the pressure differential required to overcome surface tension effects, γ is the alloy's surface tension coefficient, and r is the effective gap radius.

Development of the variable stiffness bridge represents a careful optimization across multiple design domains. By balancing geometric parameters, material properties, thermal characteristics, and manufacturing constraints, we have created a system that achieves the desired variable stiffness performance while maintaining practical fabrication and operational requirements.

3.4.2 Operational Principle

The operational mechanism of the variable stiffness segment hinges on a carefully designed thermal control system that manipulates the phase state of the low melting point alloy. The alloy layer envelops the enameled wire wrapped around the silicone rod. Both terminations of this heating element are connected to the PCB within the adjacent locomotion unit, forming a closed electric circuit.

When current (0.8-1 A) flows through the wire, Joule heating generates thermal energy that transfers conductively to the surrounding LMPA. This thermal transfer induces a phase transition in the alloy (melting point is $T_m = 62°\text{C}$ for Field's metal), resulting in two distinct operational states:

1. **Rigid State**: When the LMPA temperature is below T_m, the *solid alloy* provides structural integrity and load-bearing capacity throughout the VSS.
2. **Flexible State**: When the LMPA temperature exceeds T_m, the *liquid alloy* permits unrestricted deformation, allowing the segment to conform to various configurations.

We implemented a pulse-width modulation (PWM) control system to regulate thermal distribution during the flexible state. A temperature-based PID controller actively maintains alloy at an optimal temperature slightly above its melting threshold while preventing thermal degradation of surrounding components. Real-time temperature monitoring employs an NTC thermistor positioned within the segment. To minimize measurement interference, resistance readings are acquired exclusively during PWM low states, when heating current is momentarily suspended. Temperature calculation employs the thermistor characteristic equation:

$$T = \frac{1}{\frac{1}{\beta}\ln\frac{R}{R_0} + \frac{1}{T_0}}, \tag{3.3}$$

where β is the thermistor's coefficient, $T_0 = 298.15\text{K}$ is the based temperature point (equivalent to 25°C), and R_0 is the corresponding resistance at T_0.

The *flexible-to-rigid transition* occurs through natural cooling when power is discontinued. During solidification, minimizing mechanical disturbances is critical to prevent structural defects in the alloy matrix that could compromise mechanical integrity.

The two states exhibit dramatically different mechanical characteristics:

- In the flexible state, the segment behaves as a compliant, liquid-filled elastic tube with minimal internal resistance to deformation, enabling complex shape adaptation.
- In the rigid state, the segment transforms into a structural element with beam-like properties, capable of withstanding and transmitting significant compressive and tensile forces throughout the robot's body.

This controlled phase-change mechanism enables the robot to dynamically transition between rigid locomotion and adaptive morphological states, providing the foundation for its multifunctional capabilities.

3.4.3 Fabrication Process and Materials

Fabrication of the variable stiffness segments is a critical process that directly influences the performance and reliability of the 2SR robot. This subsection details the materials selection, preliminary calculations, and step-by-step fabrication process.

The first crucial step is to choose a suitable low-melting point alloy. We selected *Field's metal* (composition by weight: 16.5% tin, 32.5% bismuth, 51% indium) for its advantageous properties:

1. *Low melting temperature* ($T_m = 62°$C), allowing for easy phase transitions.
2. *High absolute stiffness* when solid (Young's modulus > 3 GPa), providing robust structural support.
3. *Low viscosity* when liquid, enabling smooth transitions and deformations.
4. *Safety and simple utilization* in standard laboratory conditions.

While alternatives like Cerrolow 11 ($T_m = 47°$ C) offer lower temperature thresholds, their composition (45% bismuth, 23% lead, 19% indium, 8% tin, and 5% cadmium) includes toxic elements like lead, necessitating strict safety measures and specialized handling environments.

The materials utilized in the fabrication process include:

- **Silicone rod** ($r = 2.5$ mm): Forms the core structure

- **Enameled wire** ($r = 0.05$ mm): Serves as the heating element
- **Field's metal** (RotoMetals, USA): Provides variable stiffness
- **NTC thermistor** (MF52AT, Sourcingmap, China, B-value: 3950): Enables temperature sensing
- **High-temp silicone hose** (BLING, China, $r_i = 3.5$ mm, $r_o = 4$ mm): Encapsulates the VSS assembly
- **Platinum-cured liquid silicone** (Smooth-On Dragonskin 30, USA): Used for sealing and protection
- **30 AWG wrapping wires**: Used for electrical connections

Before fabrication, preliminary calculations were conducted. Given that the maximum voltage output from locomotion units is 9.6V, the heater's resistance (R) is constrained to 9.6Ω. From the relationship between the resistance and wire dimensions, we can determine how tightly to coil the wire around the core:

$$R = \frac{\rho l}{\pi r^2}, \tag{3.4}$$

where ρ is the wire's resistivity, l is its total length, and r is its cross-sectional radius. For instance, for a copper wire with a radius of 0.05 mm, the maximum length is calculated to be 4.45 m. Based on this length, we can determine the target pitch p using the helix length formula:

$$l = \frac{h}{p}\sqrt{(\pi d)^2 + p^2}, \tag{3.5}$$

where h is the helix height (equal to the active length of the VS segment) and d is the wire's diameter.

Figure 3.3 illustrates the fabrication process of a monolithic variable stiffness segment. We begin with core preparation, using a silicone rod as the foundation. A carefully dimensioned cavity is machined at one end to house the temperature sensor and associated wiring. The heating element is constructed by winding enameled copper wire around the rod at a predefined pitch. To align both wire terminals and connect them to the controller board within a locomotion unit, we employ a bidirectional winding technique where the wire returns along the active

region with several additional turns from the end opposite the sensor cavity. To prevent electrical contact between the heating element and conductive alloy, we apply a layer of high-temperature Teflon tape, providing both electrical insulation and thermal transfer efficiency.

Then, the electrical connections are established. Both ends of the heater wire are extended using 30 AWG wrapping wires and securely fixed within the prepared cavity. Similarly, the NTC thermistor, also extended with wrapping wires, is carefully inserted into the cavity and fixed in place with adhesive. This arrangement ensures stable electrical connections and accurate temperature sensing. To protect these delicate components and secure the connections, the cavity is sealed with Smooth-On Dragonskin 30 silicone. Once cured, this silicone layer prevents component movement and shields the assembly from external damage. Further protection is provided by applying a plastic filler over the sealed cavity, extending up to the start of the heater. This encapsulates all components, creating a smooth transition between the sensing and heating sections.

The core assembly is then inserted into the silicone tube, leaving extra space at both ends for future sealing. After that, small pieces of Field's metal are carefully inserted into the space between the heater core and the hose. To ensure even distribution of the alloy, the heater is periodically activated, melting the metal and allowing it to distribute and fill the available space. This process is repeated multiple times until the hose is completely filled with the alloy.

The fabrication sequence concludes with terminal sealing, where both ends of the silicone tube are carefully sealed with additional Dragonskin silicone, creating a fully encapsulated and environmentally isolated variable stiffness segment. The completed segments are then integrated with the locomotion units to form the assembled 2SR robot, as shown in Figure 3.2(d).

This fabrication methodology ensures consistent performance across manufactured segments while maintaining the precision required for reliable thermomechanical operation.

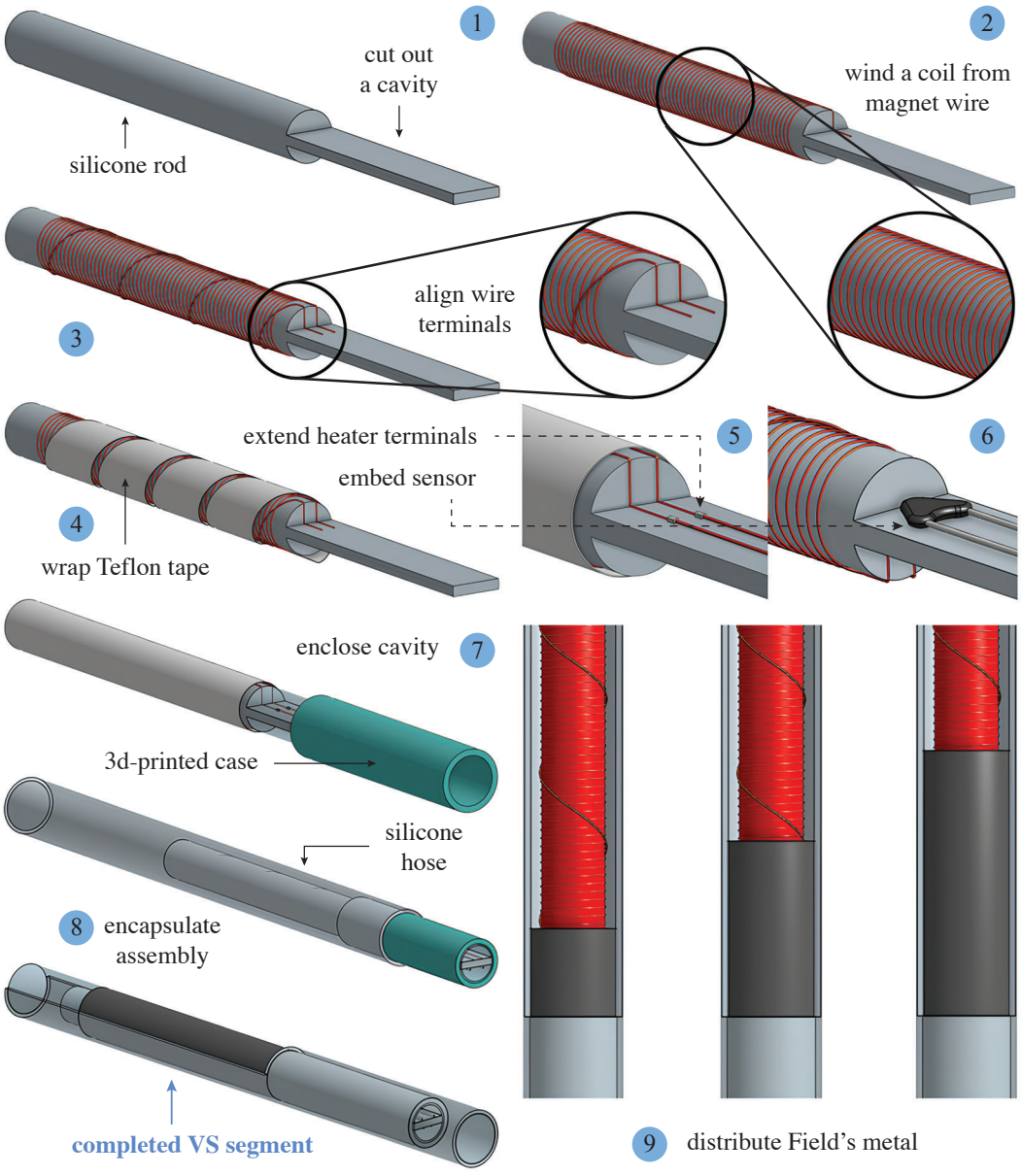

Figure 3.3: Fabrication steps of a monolithic variable stiffness segment.

3.5 VSB: Modular Approach

3.5.1 Motivation and Conceptual Architecture

Our initial monolithic variable stiffness bridge design successfully validated the foundational concept of an adaptive mobile robot capable of simultaneous locomotion and object manipulation. The performance of this system has been evaluated through multiple experiments including shape formation and full-body grasping. For further details refer to Chapter 5. While these tests confirmed the viability of our approach, they also revealed several significant performance limitations that necessitated architectural reconsideration.

Problem 3.5.1. *The monolithic design demonstrated prolonged phase transition times exceeding 100 seconds, substantial power requirements (approximately 9V per segment), and constrained bending capabilities due to a rigid 30 mm connector between segments.*

These operational constraints stemmed from design characteristics inherent to the monolithic architecture:

- *Excessive Material Volume*: The continuous LMPA core required substantial quantities of Field's metal, increasing system mass, thermal inertia, and material costs
- *Thermal Response Limitations*: The large thermal mass resulted in extended heating and cooling cycles, restricting operational responsiveness
- *Energy Inefficiency*: Maintaining the entire segment in a flexible state demanded continuous high power input
- *Non-uniform Thermal Distribution*: Achieving consistent temperature profiles throughout the elongated segments proved challenging
- *Fabrication Complexity*: The manufacturing process required precise control over LMPA distribution within extended cavities
- *Compromised Maintainability*: Component failures necessitated complete segment replacement rather than targeted repair

To address these limitations, we developed a novel modular architecture that

preserves the core variable stiffness principles while introducing significant performance enhancements. This revised approach centers on a custom 3D-printed cable chain that serves dual functions as a structural backbone and protective housing for compact variable stiffness modules, see Fig. 3.4.

The cable chain features strategically designed flat anterior and posterior surfaces that enable conformable environmental interaction, while an integrated cylindrical channel houses a series of independently controllable *modular units* (MUs). The cable chain design limits total bridge bending to π radians ($\frac{\pi}{2}$ per segment), preventing locomotion unit collision while maintaining sufficient deformation range for effective manipulation tasks. This constraint ensures that while the robot maintains full capability to form useful configurations like U-shapes, it cannot bend to potentially dangerous angles that might cause self-damage.

Our modular system architecture offers several critical advantages:

1. Reduced LMPA volume per module, enabling faster phase transitions
2. Lower power consumption through more efficient thermal management
3. Improved robustness (to failure) through easy MU replacement
4. Consistent bending characteristics throughout the cable chain structure
5. Simplified manufacturing and assembly processes
6. Scalable design allowing for bridge length customization

3.5.2 Variable Stiffness Modular Units

Variable stiffness modular units (MUs) represent a significant advancement over our previous monolithic architecture, preserving the fundamental phase change principles while considerably improving thermal efficiency, power consumption, and maintainability through miniaturization and refined engineering.

Each MU features a precision-engineered layered construction: a central silicone rod (3 mm diameter) extends through a cylindrical Field's metal element (10 mm length, 3 mm inner diameter, 5 mm outer diameter), with the entire assembly encapsulated by custom-designed plastic end caps and housed within a protective silicone shell (5 mm inner, 6 mm outer diameter). A key innovation in this design

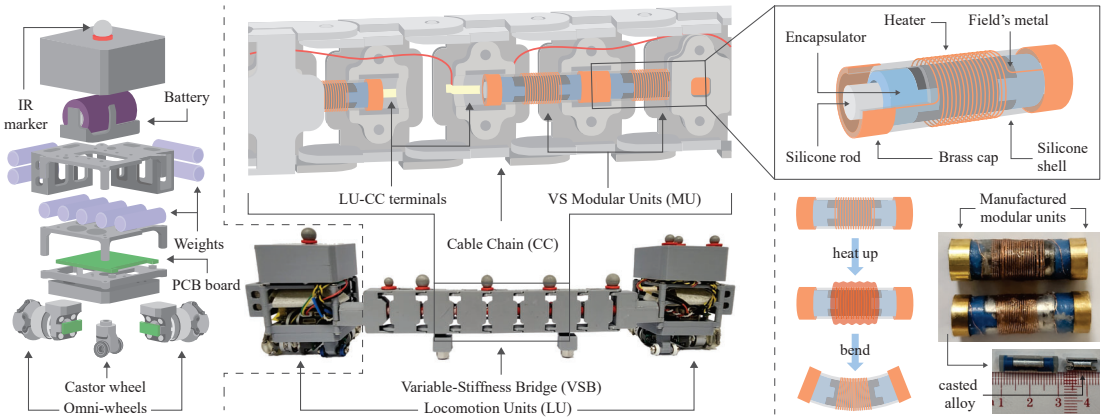

Figure 3.4: Structural overview of the upgraded 2SR robot: exploded view of the locomotion unit showing its internal architecture; composition of the assembled variable-stiffness (VS) bridge with modular units forming a cable chain backbone; detailed view of a single VS modular unit showing its components and operating principle; photographs of manufactured components including the cast alloy layer and fully assembled module.

involves the repositioning of the heating element — a fine copper wire (0.1 mm diameter) — to the exterior of the silicone shell rather than between the core and alloy layer. This critical modification serves multiple purposes: it eliminates potential wire damage during the fabrication process, simplifies the manufacturing sequence, and enables non-destructive heater replacement without compromising the alloy-containing section.

The electrical interfacing strategy has been completely redesigned, replacing vulnerable external wiring with robust brass cap terminals directly soldered to the heating element and mounted at the unit's extremities. This approach improves electrical reliability while simplifying the integration process.

Through precision manufacturing techniques, we achieved a highly compact modular unit measuring approximately 20 mm in length and 7 mm in diameter. The fabrication process begins with the precise formation of the Field's metal component — small alloy fragments are melted in a temperature-controlled syringe and injected into a high-resolution 3D-printed mold, producing a hollow cylindrical element with engineered notches at both ends that ensure secure mechanical coupling with the plastic encapsulators. After the alloy layer is prepared, a silicone rod is passed through the molded cylinder, after which this assembly is inserted into the encapsulating silicone hose. Both sides are then sealed with curable silicone.

The heating element is applied using an automated precision coiling device that wraps the copper wire around the silicone shell at a consistent 0.26 mm pitch. This configuration yields a total resistance of 1.7Ω, a value carefully optimized through thermal modeling to achieve rapid phase transitions at 1A current (the maximum safe current for the wire) while limiting the required voltage to 1.7V, thereby minimizing power consumption. A protective layer of Dragon Skin™ 30 curable silicone is applied over the heating element to prevent mechanical damage and provide electrical insulation. Components and tools used during fabrication are illustrated in Fig. 3.5.

The complete bridge incorporates two independently controlled segments, each containing four modular units, requiring a maximum of 6.8V per segment. The length of each segment constituted to 80 mm resulting in a total bridge length (including LU-to-VSS connectors) of approximately 22 cm. Modules are positioned between chain nodes, with their brass terminals making direct contact with copper conductors embedded within the node channels, establishing reliable electrical connectivity throughout the structure. At the junction between segments (middle chain node), modules are designed without outward-facing brass caps to maintain electrical isolation between the independently controlled segments.

Terminal modules positioned at the locomotion unit junctions incorporate NTC

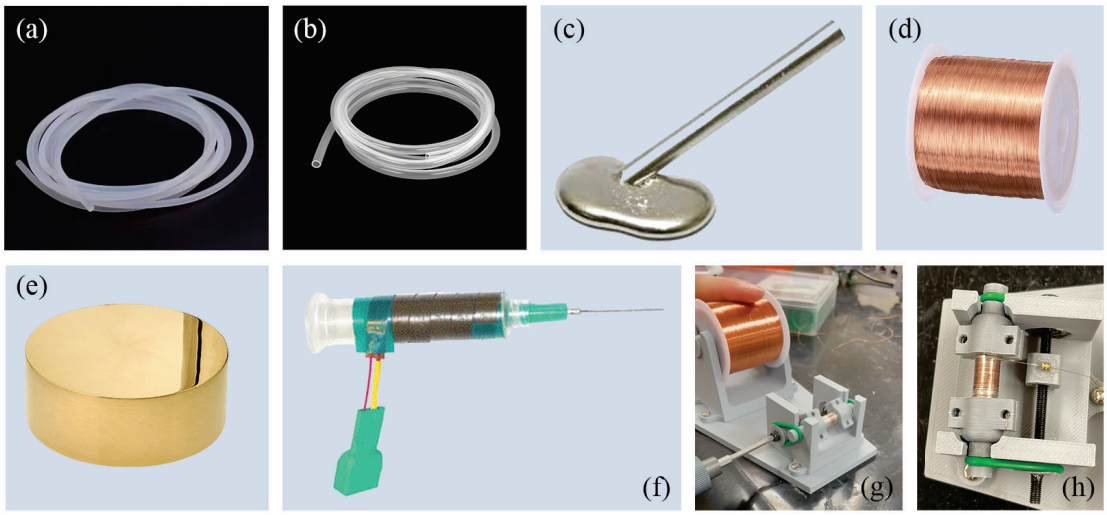

Figure 3.5: Components and tools used in fabricating variable stiffness modular units. (a) Silicone rod. (b) Silicone hose. (c) Field's metal. (d) Enameled copper wire. (e) Brass cap. (f) Syringe with embedded heater. (g) Automated precision coiling device. (h) Modular unit with winded enameled wire.

thermistors for real-time temperature monitoring and feedback control, see Fig. 3.6. Each variable stiffness segment connects to its adjacent locomotion unit through a four-conductor interface: two conductors for the temperature sensor and two for the heating circuit (one from the terminal module, another from the middle node contact), establishing a complete control loop.

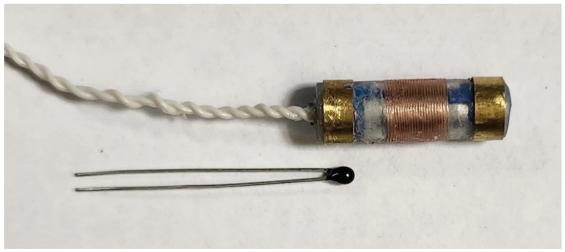

Figure 3.6: Terminal modular unit with embedded NTC thermistor for temperature monitoring of the Field's metal.

This modular architecture significantly enhances system maintainability — individual failed units can be readily extracted and replaced without requiring complete segment reconstruction, reducing maintenance complexity and operational downtime compared to the monolithic design. Performance evaluation of the modular variable stiffness segment, detailed in Chapter 4, revealed a 2.5-fold improvement in stiffness transition time compared to the monolithic design.

3.6 Summary

In this chapter, we have introduced the design and fabrication methodologies for the 2SR (Self-Reconfigurable Soft-Rigid) robot, representing a novel class of mobile robots with adaptive morphology and variable stiffness capabilities. The 2SR robot combines the precision mobility of conventional hard robots with the adaptability of soft robotics, creating a versatile hybrid platform capable of navigating planar environments and manipulating objects through body deformation.

The core design consists of two locomotion units (LUs) connected by a variable stiffness bridge (VSB). Each LU functions as a self-contained omnidirectional robot with two strategically positioned omni-wheels, integrated electronics, and power systems. This configuration enables both conventional mobility when rigid and controlled deformation when flexible.

We presented two evolutionary implementations of the variable stiffness bridge.

The initial *monolithic design* established proof-of-concept with a continuous variable stiffness segment containing Field's metal, a low melting point alloy (LMPA) with a transition temperature of 62°C. This design featured a silicone rod with a heating element wrapped around it and encapsulated within a silicone tube containing the phase-change material. While functional, this approach revealed significant limitations in transition speed, power consumption, and maintenance complexity.

Our refined *modular design* addressed these limitations through a fundamental architectural shift, incorporating a 3D-printed cable chain housing discrete variable stiffness modules. Each modular unit contains a significantly reduced volume of LMPA and features an optimized heating system with the heating element repositioned outside the alloy layer. This innovation enabled faster phase transitions (2.5× improvement), reduced power requirements, enhanced maintainability through replaceable units, and more uniform thermal distribution.

The modular approach offers numerous additional advantages:

- *Scalability* - bridge length can be customized by adding or removing modules
- *Design flexibility* - module characteristics can be varied within a single bridge
- *Resource efficiency* - uses significantly less Field's metal while maintaining performance
- *Simplified assembly* and *disassembly* processes
- Potential for *mass production* through standardized components

The fabrication processes for both designs were detailed, highlighting material selection criteria, dimensional optimization balancing operational range against power consumption, and the precise manufacturing techniques required for reliable thermomechanical performance. Particularly noteworthy is the optimization of the modular units' electrical characteristics to achieve efficient heating with minimal power consumption.

The described fabrication steps for both designs include:

- Material selection based on thermal, mechanical, and safety properties

- Dimensional optimization balancing operational range against power consumption
- Precise manufacturing techniques required for reliable thermomechanical performance
- Electrical characteristics optimization to achieve efficient heating with minimal power consumption
- Strategic integration of sensing elements for closed-loop thermal control

This chapter has established the foundational design principles and fabrication methodologies that enable the 2SR robot's unique adaptive capabilities. The evolution from monolithic to modular architecture demonstrates how iterative design refinement can substantially enhance performance while maintaining core functionality. The modular approach not only improves operational characteristics but also provides flexibility for future adaptations and applications beyond mobile robotics.

The developed 2SR robot represents a significant advancement in adaptive mobile robotics, bridging the gap between traditional rigid systems and compliant soft robotics. By combining omnidirectional mobility with controllable stiffness, the platform establishes new possibilities for robots that can seamlessly transition between efficient locomotion and versatile environmental interaction.

Chapter 4

Stiffness Control

The ability to modulate stiffness in robotic systems opens new possibilities for adaptive behaviour and enhanced interaction capabilities. This chapter focuses on the control system design for our novel mobile robot equipped with variable-stiffness components. The robot's unique architecture features two segments, each with independently controllable stiffness, presenting both distinctive opportunities and considerable challenges in control system development.

Each VS segment comprises compact modular units that incorporate low-melting point alloy and heating elements for stiffness control. We use Field's metal as the LMPA, characterized by a melting temperature of approximately 62° Celsius. Below this temperature, the alloy is solid, providing structural stability to the segment. At or above the melting temperature, the alloy transitions to a liquid phase, making the unit flexible and allowing for morphological adaptation.

Electrical design of the system implements a simplified control architecture where all units within a segment are connected in series within a common circuit. This means that units within each segment are controlled collectively – they all transition between rigid and flexible states simultaneously. To reduce circuit complexity and minimize the number of components, we incorporate just one temperature sensor per segment, rather than monitoring each unit individually.

This design choice, while offering practical advantages in implementation, introduces several significant limitations and requirements:

1. *Indirect Temperature Monitoring*:
    - The temperature sensor is not in direct contact with the metal
    - A single sensor must represent the state of multiple units
    - Manufacturing variations between units (different unit lengths, varying amounts of metal, and slight differences in heater coil lengths) create inconsistencies in their heating and cooling behaviour
2. *State Transition Management*:
    - The transition to the flexible state requires active heating of the alloy
    - The return to the rigid state relies on passive cooling
    - Accurate state estimation is crucial despite limited sensing capabilities
3. *System Integration*:
    - Motion dynamics is continuous while the stiffness states are discrete
    - Robot behaviour directly depends on the stiffness state of its segments
    - Control strategies must account for both motion and stiffness transitions

These challenges lead to two major problems that must be addressed:

Problem 4.0.1 (Stiffness Estimation)**.** *With only a single temperature sensor per segment and indirect temperature measurements, we cannot directly observe the LMPA's physical state throughout the structure. This limitation is compounded by asymmetric thermal behaviour during heating versus cooling cycles, creating a complex, nonlinear relationship between sensor readings and actual segment stiffness that cannot be resolved through simple threshold-based approaches.*

Problem 4.0.2 (Hybrid Control Integration)**.** *The robot operates across fundamentally different control domains that must be seamlessly integrated: the discrete stiffness states of each segment (rigid or flexible) and the continuous dynamics of robot motion. This integration is particularly challenging because the robot's kinematic and dynamic properties change dramatically between stiffness states. The control system must manage stiffness transitions in real-time while simultaneously*

maintaining stable motion and positioning — all while accounting for the significant time delays inherent in thermal state changes.

4.1 Temperature Estimation

Temperature monitoring in our system is implemented using NTC thermistors, which exhibit an inverse relationship between temperature and resistance. The raw temperature measurement is obtained through a series of conversions. First, the thermistor resistance is calculated using the voltage divider, see Fig. 4.1:

$$R_{out} = R_{ref} \left(\frac{1023}{V_{out}} - 1 \right). \tag{4.1}$$

The temperature is then derived using the Steinhart-Hart equation, simplified to the β-parameter equation:

$$T = \frac{1}{\frac{1}{\beta} \ln(\frac{R_{out}}{R_0}) + \frac{1}{T_0}}, \tag{4.2}$$

where R_0 and T_0 are the base values for the thermistor. Finally, the temperature is converted to Celsius:

$$T_c = T - 273.15. \tag{4.3}$$

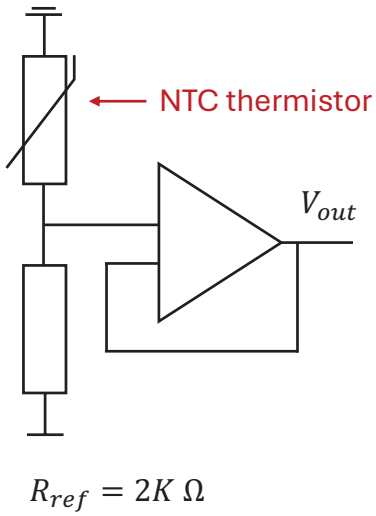

Figure 4.1: NTC thermistor circuit diagram.

However, direct application of raw temperature measurements proves inadequate for accurate system state estimation. Experimental observations revealed significant discrepancies between the measurements and the system's actual behaviour.

Remark 1. *Segments were observed to transition to flexible states more rapidly than indicated by temperature measurements, and readings continued to increase even after heating power was disabled. These differences can be attributed to various factors including heat transfer delays in the sensor and thermal gradients between sensor location and LMPA.*

These discrepancies might be attributed to several factors:

- Thermal mass effects
- Heat transfer delays in the sensor
- Residual heat in the surrounding area
- Thermal gradients between the sensor location and the LMPA

To compensate for these effects, we implement a nonlinear estimation model:

$$\begin{cases} T_{norm} = \frac{T - T'}{\overline{T}_{sns} - T'}, \\ T_{estim} = T' + T_{norm}(\overline{T}_{lmpa} - T'), \end{cases} \tag{4.4}$$

where $T' = 22°\text{C}$ is the ambient temperature in the lab, $\overline{T}_{sns}$ is the maximum temperature reading from the sensor, and $\overline{T}_{lmpa}$ is the maximum observed temperature of the alloy. These model parameters were empirically calibrated by manually testing segment stiffness.

4.2 Finite-State Machine

The integration of temperature and motion control presents a significant challenge in our system. While temperature is managed at the lower level through PID control with a conservative setpoint of 64°C, a higher-level control strategy is required to coordinate stiffness transitions with robot motion. The Finite-State Machine (FSM) approach provides an elegant solution for managing these discrete state transitions while maintaining system stability and reliability.

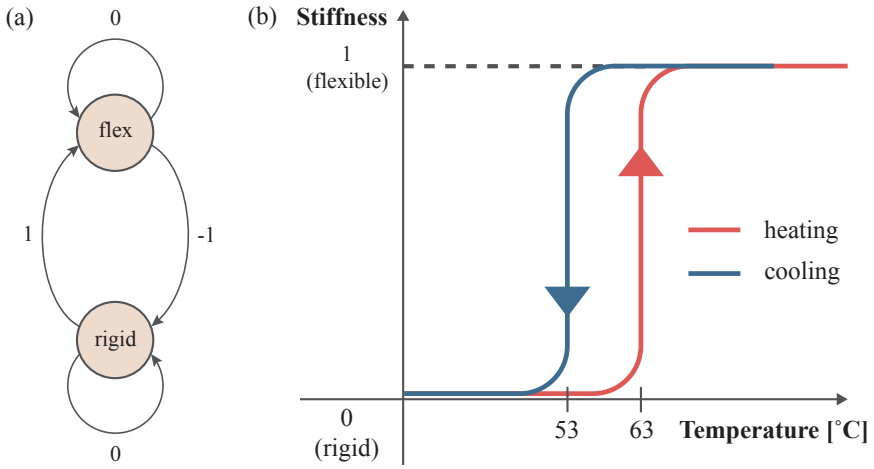

Figure 4.2: (a) Finite-state Machine (FSM)diagram showing the rigid (0) and flexible (1) states with corresponding transitions. (b) Hysteresis curve illustrating the relationship between temperature and stiffness during phase transitions.

In our robot's variable-stiffness core, each modular unit can exhibit two discrete states: *rigid* and *flexible*. Since units within a single fiber segment receive identical commands and share approximately the same stiffness state, we can simplify its representation by considering stiffness at the segment level rather than individual units. For our 2SR robot with two segments, we define the discrete state space as:

$$\mathbf{s} = [s_1, s_2]^\intercal, \tag{4.5}$$

where s_i is a boolean value representing the stiffness state (0 for *rigid* and 1 for *flexible*) of the $i-$th segment.

The Finite-State Machine approach is particularly well-suited for controlling and handling stiffness changes in our robot for several reasons:

1. **Discrete Nature**: The binary stiffness states of a 2SR robot (rigid or flexible) align perfectly with the FSM's discrete state representation.

2. **Event-Driven Transitions**: FSMs excel at modelling systems where state changes occur in response to specific events or inputs, which is precisely how our robot's stiffness changes are triggered.

3. **Clear Logic**: The FSM provides a clear and intuitive way to define the rules for state transitions, making the control logic easy to understand, implement, and debug.

4. **Scalability**: As we potentially add more segments or states to our robot, the FSM can be easily extended to accommodate these additions.

5. **Efficient Implementation**: FSMs can be implemented with minimal computational overhead, which is crucial for real-time control of our mobile robot.

The stiffness transitions in our robot occur at discrete intervals triggered by control decisions. To manage these transitions systematically, we implement a Finite-State Machine with clearly defined states, inputs, and transition functions. The FSM operates with two possible states (rigid or flexible), and accepts three types of inputs as shown in Fig. 4.2(a):

$$\begin{aligned} \textbf{States}: &\ S : 0, 1 \\ \textbf{Inputs}: &\ \Sigma : 0, 1, -1 \\ \textbf{Transition function}: &\ \delta : S \times \Sigma \to S \\ \textbf{Next state law}: &\ s_i(k+1) = \delta(s_i(k), a_i), \end{aligned} \tag{4.6}$$

where a_i represents the discrete action to change the stiffness of segment i, k represents the discrete time step. Action $a = 0$ means to stay in the current stiffness state, $a = 1$ means to start LMPA melting, and $a = -1$ means to cool down LMPA. The transition function $\delta(s, a)$ is elaborated in Table 4.1:

State	Input	Next State	Output
Rigid (0)	0	Rigid (0)	None
	1	flexible (1)	Melts LMPA → VSS turns flexible
	-1	Rigid (0)	None
flexible (1)	0	flexible (1)	None
	1	flexible (1)	None
	-1	Rigid (0)	Solidifies LMPA → VSS turns rigid

Table 4.1: State-transition table of the FSM stiffness controller.

State transitions in our variable stiffness system are not instantaneous but rather gradual changes that occur over time. When the FSM receives a command to change state, it initiates either the melting or cooling of the low-melting-point alloy within all modular units of a segment. These phase transitions are inherently time-dependent due to the thermal properties of the materials involved. To monitor these transitions, the robot is equipped with temperature sensors that

continuously provide feedback about the thermal state of the VS core. The stiffness controller uses this real-time temperature information to make decisions about state transitions and ensure that the desired stiffness change has been achieved.

The state transition process is handled by FSM as follows:

1. **Temperature Monitoring**:
    - Continuous sensor feedback monitors the thermal state
    - Real-time temperature information guides transition decisions
    - System ensures complete phase transitions before state updates
2. **Transition Thresholds**:
    - Field's metal nominal melting point: 62°C
    - Conservative softening threshold: $T_s = 63$°C
    - Operating setpoint: 64°C (safety margin)
3. **Rigid-to-Flexible Procedure**:
    (a) FSM activates a segment heater via low-level controller
    (b) LMPA temperature increases under PID control
    (c) Temperature sensors provide continuous feedback
    (d) FSM confirms transition to flexible when $T \geq T_s$

This approach ensures that the LMPA has fully melted before the system considers the segment to be in the flexible state. The slight increase in the threshold temperature (from 62°C to 64°C) provides a safety margin to guarantee complete melting across all modular units in the segment, accounting for potential minor variations in heating distribution or sensor accuracy. It's important to note that even after the FSM has transitioned to the flexible state, the actual physical properties of the segment may continue to change slightly as the temperature potentially rises further or as the melted alloy distributes more evenly throughout the modular units. However, for control purposes, these minor changes are considered negligible once the flexible state has been reached.

The transition from the flexible to rigid state presents a more complex scenario than its counterpart. This complexity arises from various factors related to the mechanical properties of the adaptive bridge and its modular units, as well as the thermal dynamics of the system:

1. **Non-uniform Alloy Distribution**: During the fabrication process, slight variations in the amount of LMPA encapsulated within each modular unit are inevitable. These variations, while minor, lead to differences in melting/cooling rates across units. Units with more alloy will take longer to cool and solidify completely, potentially leading to non-uniform stiffness across the segment during the transition phase.

2. **Thermal Inertia and Non-uniform Solidification**: When the heating elements are turned off, the high temperature doesn't immediately dissipate. Instead, it persists for several moments before gradually declining. This thermal inertia results in a non-uniform solidification process across the LMPA segment. As cooling begins, some parts of the LMPA may start to solidify while others remain liquid, creating a complex, partially solidified state that is neither completely flexible nor fully rigid.

3. **Limited Sensor Distribution**: Our current design incorporates only one temperature sensor per segment. While this approach minimizes complexity and cost, it also means that we're relying on a single point of measurement to infer the thermal state of the entire segment. This limitation can lead to potential discrepancies between the measured temperature and the actual thermal state of all units within the segment.

4. **Indirect Temperature Measurement**: The temperature sensor is not in direct contact with the LMPA but instead measures the ambient temperature within the modular unit. The environment within the MU retains heat longer than the LMPA itself, potentially leading to an overestimation of the alloy temperature. Additionally, the sensor itself has thermal mass and requires time to cool down, introducing a delay in temperature readings.

5. **Measurement Noise**: Like all sensor systems, our temperature measurements are subject to noise. This noise can come from various sources, including electromagnetic interference and thermal fluctuations. While individual

noise instances might be small, they can accumulate and affect the accuracy of state determination, especially near the transition thresholds.

Remark 2. *These factors collectively contribute to a phenomenon known as hysteresis. Hysteresis is a characteristic where the system's output (in our case, the stiffness state) depends not only on the current input (temperature) but also on the system's previous state and history. In the context of our variable stiffness robot, hysteresis manifests as a difference between the melting and solidification temperatures of the LMPA, as illustrated in Fig. 4.2(b). While the alloy begins to melt at around* $62°C$*, it doesn't immediately solidify when cooled back to this temperature. Therefore, to ensure complete solidification across all modular units, the system needs to be cooled further. Through empirical testing, we've determined a lower temperature threshold as* $T_r = 53°C$.

This conservative approach ensures the reliability and consistency of our variable stiffness system, albeit at the cost of a longer transition time from flexible to rigid compared to the reverse process. The complete FSM stiffness controller is summarized in Algorithm 1.

Algorithm 1: FSM Stiffness Controller

Input: $\mathbf{s}_0$, $\mathbf{s}_d$
Result: $\mathbf{s}$
Initialize $\mathbf{a}$, T_1, T_2, $T_s = 63$, $T_r = 53$;
$\mathbf{s} = \mathbf{s}_0$;
Function `ControlLoop()`**:**
  while $\boldsymbol{a} \neq (0, 0)$ **do**
    $T_1, T_2 \leftarrow$ `ReadTemperature(`$\boldsymbol{s}_d$`)`;
    $\mathbf{a} \leftarrow$ (`GetAction(`*0*`)`, `GetAction(`*1*`)`);
    `SendCommandsToRobot(`$\boldsymbol{s}_d$`)`;
    `ApplyAction(`*0*, $\boldsymbol{a}[0]$, T_1`)`;
    `ApplyAction(`*1*, $\boldsymbol{a}[1]$, T_2`)`;
Function `GetAction(`i`)`**:**
  if $\mathbf{s}[i] = \mathbf{s}_d[i]$ **then return** 0;
  else if $\mathbf{s}[i] = 0$ **and** $\mathbf{s}_d[i] = 1$ **then return** *1*;
  else return *-1*;
Function `ApplyAction(`i, a, T`)`**:**
  if $a = 1$ **and** $T \geq T_s$ **then** $\mathbf{s}[i] \leftarrow 1$;
  else if $a = -1$ **and** $T \leq T_r$ **then** $\mathbf{s}[i] \leftarrow 0$;

4.3 Experiment: Stiffness Characterization of the Modular VSS

To validate the effectiveness of our robot's design and the proposed stiffness control system, we conducted a stiffness characterization experiment. The experimental setup was deliberately simplified to focus on the fundamental capabilities of the variable-stiffness mechanism. We mounted a single variable-stiffness segment to a platform equipped with a microcontroller and battery. The segment was positioned horizontally, parallel to the floor, with its initial configuration being straight and rigid, see Fig. 4.3. The experiment was conducted in a laboratory environment with a controlled ambient temperature of approximately 23°C.

The experimental protocol consisted of three complete state transition cycles, with each cycle comprising three distinct phases:

- *Heating phase:* transition from rigid to flexible state.
- *Sustained flexibility phase:* maintaining flexibility for one minute.
- *Cooling phase:* transition from flexible to rigid state (by cooling down to 42°C in order to get a better picture of the solidification process).

In order to demonstrate the variable stiffness capabilities of the bridge segment, we attached a lightweight test load (a 9.7g toy cat) to the distal end of the segment. This provided a visible indicator of the segment's mechanical state. When rigid, the segment maintained its straight configuration despite the load. Upon heating and transitioning to the flexible state, the segment visibly deformed under the combined weight of itself and the test load, demonstrating its increased compliance.

During the sustained flexibility phase, we manually manipulated the segment in both upward and downward directions to verify its pliability. In one cycle, we deliberately held the segment in an upward-curled position during the cooling phase, allowing it to solidify in this deformed configuration. Notably, when heated again in the subsequent cycle, the segment naturally uncoiled and returned to its initial straight, hanging state due to gravity.

The experimental results confirmed several key aspects of our design:

- Successful bidirectional transitions between rigid and flexible states.

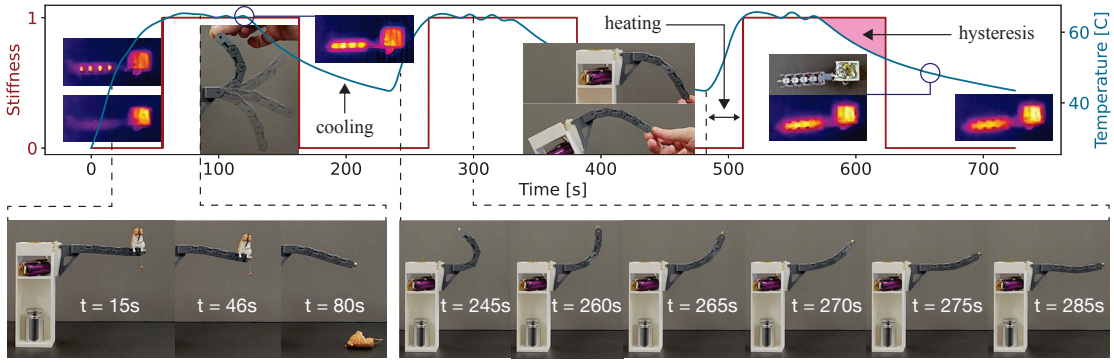

Figure 4.3: Graphical representation of a variable-stiffness segment (VSS) alternating between rigid and flexible states. The VSS undergoes three complete state transition cycles, each comprising three distinct phases: heating (transition from rigid to flexible), maintaining sustained flexibility, and cooling (transition from flexible back to rigid). The blue line in the graph indicates the temperature profile. The red line illustrates the segment's stiffness.

- High flexibility in the flexible state allowing significant deformation.
- Sufficient rigidity in a rigid state to maintain arbitrary shapes.
- Repeatability of the state transitions across multiple cycles.

The transition characteristics showed significant improvements over the previous monolithic design. The average flexible-to-rigid transition time was 47.1 seconds, with complete cooling to 42°C requiring 142 seconds. The rigid-to-flexible transition time varied with initial temperature: 35.9 seconds when heating from 42°C and 22.4 seconds from 53°C. These transition times represent a 2.5-fold improvement compared to the previous non-modular design, demonstrating that the modular architecture substantially enhances the phase transition performance of the variable-stiffness segment. These timing characteristics are important considerations for practical applications and motion planning.

The conducted experiment demonstrated that the modular variable stiffness segment successfully achieves its design objectives, providing controllable transitions between rigid and flexible states while maintaining the desired mechanical properties in each state. The ability to hold arbitrary shapes when rigid, combined with high deformability when flexible, confirms the potential utility of this design in adaptive robotic applications.

4.4 Summary

This chapter addressed the critical challenge of stiffness control in our variable-stiffness hybrid mobile robot. We developed a robust control system to manage the robot's ability to transition between rigid and flexible states, which is essential for its multifunctional capabilities.

We began by identifying two fundamental problems inherent in the system design: accurate stiffness estimation with limited sensing capabilities, and integration of discrete stiffness states with continuous motion control. Our solution comprised two key components:

First, we implemented a nonlinear temperature estimation model to compensate for the limitations of having only a single temperature sensor per segment. This model addresses the complex thermal behaviour during heating and cooling cycles, accounting for factors such as thermal mass effects, heat transfer delays, and thermal gradients between the sensor location and the LMPA material.

Second, we developed a Finite-State Machine (FSM) approach that elegantly manages the discrete stiffness transitions while integrating with the robot's continuous motion dynamics. The FSM handles the hysteresis phenomenon observed during phase transitions, implementing different temperature thresholds for melting (63°C) and solidification (53°C) to ensure reliable operation.

Experimental validation demonstrated the effectiveness of our stiffness control system, showing successful bidirectional transitions between rigid and flexible states, high deformability when flexible, and sufficient rigidity to maintain arbitrary shapes when rigid. Our modular design achieved a 2.5-fold improvement in transition times compared to the previous non-modular approach.

This stiffness control framework provides the foundation for the robot's advanced capabilities, enabling the seamless integration of mobility and manipulation functions that will be explored in subsequent chapters.

Chapter 5

Motion and Morphology Control

A 2SR robot presents a unique fusion of hard and soft capabilities. This dual nature significantly expands its potential applications, from traditional mobile robot tasks to complex manipulation scenarios requiring adaptive morphology. However, this versatility introduces substantial challenges in developing a unified control framework that can effectively manage both operational modes.

The primary challenge lies in reconciling two fundamentally different behavioural states: when rigid, the robot functions as a conventional mobile platform with omnidirectional movement capabilities; when flexible, it behaves as a deformable manipulator requiring precise shape control. These distinct operational modes necessitate different approaches to kinematic modelling and control strategy development.

In this chapter, we present a comprehensive control framework that addresses these challenges through a *hybrid kinematic model*. Our approach begins by separately analyzing the kinematics for both rigid and flexible states, then integrates these analyses into a unified model. This hybrid model accounts for:

1. The discrete nature of stiffness states and their impact on robot behaviour
2. The continuous dynamics of motion in both rigid and flexible configurations
3. The additional complexity of shape control when segments are flexible
4. The coordination between locomotion

Before delving into the detailed analysis, we establish several *key assumptions* that frame our control approach:

- The stiffness state of each bridge segment is represented by a boolean variable s_i, where $s_i = 0$ indicates a rigid state and $s_i = 1$ indicates a flexible state. During state transitions, the robot remains stationary, allowing us to disregard transition dynamics in our kinematic model.
- Bridge segments maintain constant length throughout all operations, simplifying our kinematic calculations.
- Flexible segments deform exclusively into circular arcs with constant curvature, allowing for predictable and controllable shape modifications.
- The locomotion units can operate independently when segments are flexible, enabling sequential movement strategies where one unit remains fixed while the other moves.
- The omnidirectional capability of the robot is maintained in a rigid state through the strategic placement of four omni-wheels (two per locomotion unit), regardless of the robot's configuration.

These assumptions provide a foundation for developing our control framework while maintaining practical applicability. The remainder of this chapter details the development of our *Motion & Morphology Controller*, which successfully manages the robot's dual nature while ensuring precise control in both stiffness states.

5.1 Hybrid Kinematics

Development of a comprehensive kinematic model for the 2SRA (2SR agent) presents unique challenges due to its variable morphology and dual-state nature. Unlike traditional robots with fixed geometry, our robot's shape can dynamically change through the deformation of its VS bridge. This characteristic requires a more sophisticated approach to state space definition and kinematic modeling.

The key to our hybrid kinematic framework lies in effectively describing the robot's configuration while accommodating both rigid and flexible states. Each bridge segment, when flexible, deforms into a circular arc with constant curvature,

following our simplifying assumptions. This behaviour allows us to parameterize the segment's shape using three key elements:

1. The position of one endpoint
2. The tangent direction at this endpoint
3. The segment's curvature

Given the mechanical coupling between the two segments at their shared connection point, we establish a body reference frame $\{B\}$ at this junction as illustrated in Fig. 5.1. This frame is strategically aligned with the tangent at the connection point, providing a natural reference for describing the robot's overall configuration. This choice of frame placement offers several advantages:

- It creates a consistent reference point regardless of segment states
- It simplifies the description of segment curvatures
- It represents continuity between segments

Based on the chosen reference state, the complete configuration of the robot can thus be captured by a five-dimensional vector of generalized coordinates:

$$\mathbf{q} = [x_b, y_b, \theta_b, \kappa_1, \kappa_2]^\intercal, \tag{5.1}$$

where (x_b, y_b) represents position of the $\{B\}$ frame in the global coordinate system, θ_b is its orientation, κ_i denote the curvature of the $i-$th segment.

Remark 3. *A 2SR robot has distinct front and back sides. The variable stiffness bridge is offset from the center of the locomotion units toward one face, creating a continuous smooth surface across both LUs and the bridge. This design maximizes potential contact between the robot and its surroundings when needed. We refer to this smooth side as the "front" and the opposite side as the "back." Additionally, we designate the left (first) locomotion unit as the "head" and the right (second) locomotion unit as the "tail."*

This formulation provides a unified way to describe the robot's configuration regardless of its segment states, while maintaining the ability to represent both rigid ($\kappa_i = 0$) and flexible ($\kappa_i \neq 0$) states within the same mathematical framework.

5.1.1 Rigid Mode

When both segments are in a rigid state ($s_1 = s_2 = 0$), a 2SR robot functions as a conventional omnidirectional mobile platform. In this configuration, the robot's shape remains constant, and its motion can be fully described by the velocities of the body frame $\{B\}$. Kinematics in this case is much simpler compared to the flexible mode, since the curvatures rate remains fixed ($\dot{\kappa}_1 = \dot{\kappa}_2 = 0$).

The rigid mode kinematics can be expressed through a straightforward relationship between the generalized coordinate velocities and the control inputs:

$$\dot{\mathbf{q}} = \underbrace{\overline{(s_1 \vee s_2)} \begin{bmatrix} \mathbf{R}_z(\theta_b) \\ 0 \end{bmatrix}}_{\mathbf{J}_r} \mathbf{u}_r, \tag{5.2}$$

where $\mathbf{R}_z(\theta_b) \in \mathbb{R}^3$ is a rotation matrix around the vertical axis of the global frame and $\mathbf{u}_r = [v_{bx}, v_{by}, \omega_b]^\intercal$ is a vector of robot's "rigid" control velocities associated with the $\{B\}$ frame.

Remark 4. *The zero elements in the bottom of* $\mathbf{J}_r$ *reflect the constant curvature rates during rigid operation.*

This formulation provides a direct mapping between the desired motion commands and the resulting changes in the robot's configuration, enabling straightforward implementation of motion control strategies in the rigid state.

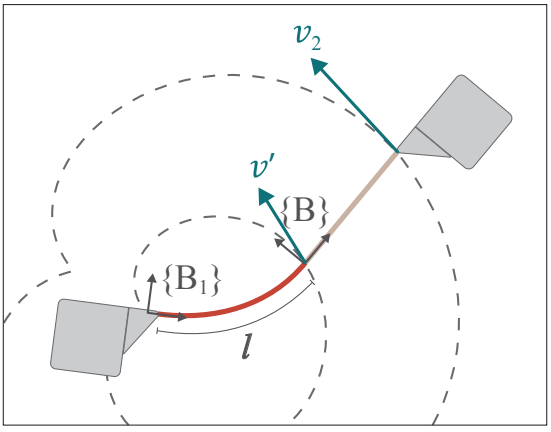

Figure 5.1: Schematic representation of the 2SR robot's geometry and reference frames.

5.1.2 Flexible Modes

The kinematic behaviour of the 2SRA robot becomes more complex when one or both segments transition to their flexible state ($s_1 = 1$ and/or $s_2 = 1$). In these configurations, the locomotion units operate independently, creating distributed bending patterns along the flexible segments. The uniform distribution of identical nodes in the adaptive bridge results in approximately constant curvature deformation, allowing us to model each flexible segment as a circular arc. To prevent collisions between locomotion units, the cable chain bending is restricted to a half-circle, constraining segment curvatures to $-\frac{\pi}{2l} \leq \kappa_i \leq \frac{\pi}{2l}$.

Remark 5. *A key insight in understanding the flexible mode kinematics comes from observing the motion patterns of the LUs. During bridge bending, LUs trace a distinctive curve. Initially, we employed logarithmic spirals to model this motion due to their apparent resemblance to the observed paths, see Fig. 5.2. However, this approach required separate functions with different parameters for positive and negative curvatures, creating discontinuities at boundary conditions. Subsequently, we adopted a cardioid model, which provides a single mathematical shape that effectively approximates LU paths across all permissible curvature values. The following kinematics derivation is based on this cardioid representation.*

Cardioid curve is described by the following parametric model:

$$\begin{cases} x(\phi) = \rho \cos \phi \\ y(\phi) = \rho \sin \phi \\ \rho = 2r(1 - \cos \phi), \end{cases} \tag{5.3}$$

where $0 \leq \phi \leq 2\pi$ is the rolling angle, ρ is the cardioid's radius at ϕ, and r is the common radius of the two generating circles of the cardioid.

To fully comprehend the kinematics of the robot in a flexible state, we categorize the operational modes into three distinct scenarios where different combinations of bending and motion occur. Each scenario is associated with a unique cardioid, as illustrated in Fig. 5.3:

I: **Flexible-Rigid Configuration with Actuated Flexible End**

- One segment is flexible while the other maintains rigidity

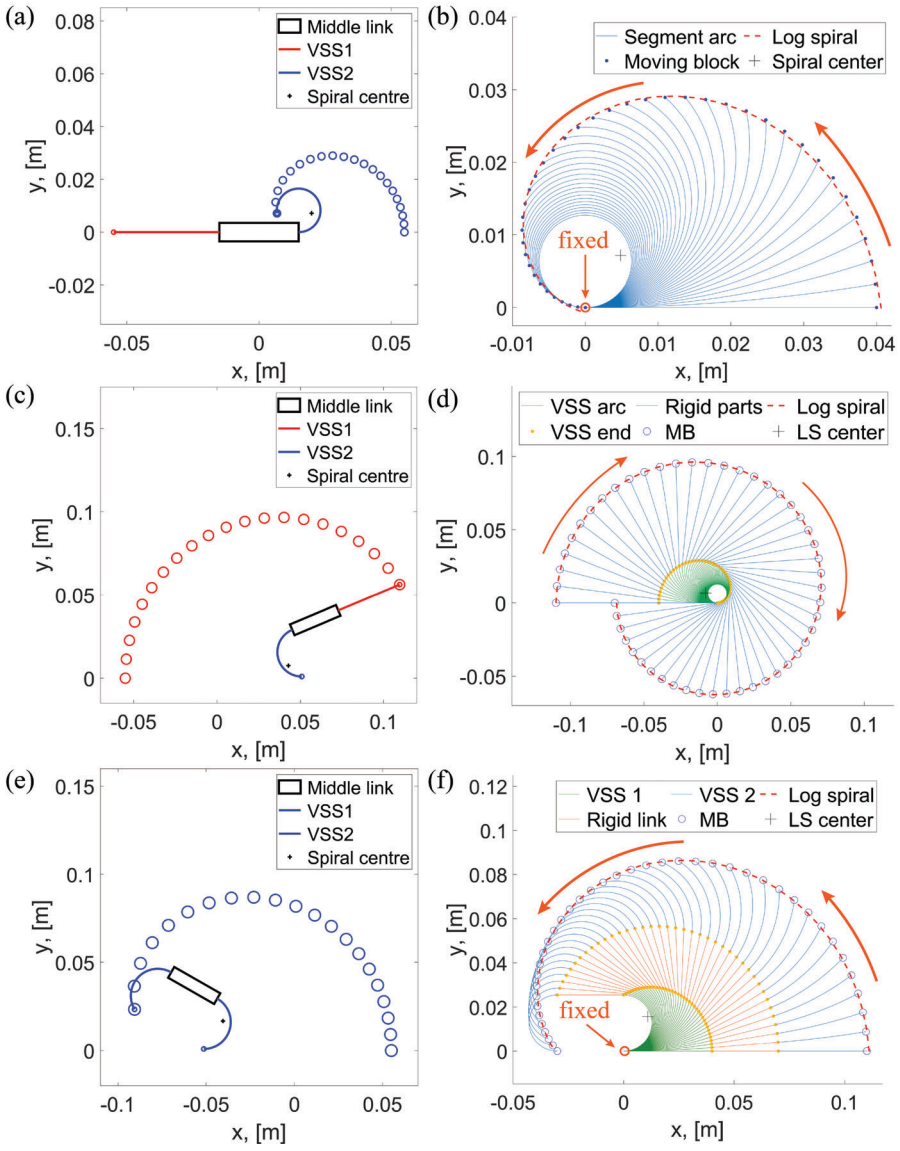

Figure 5.2: Shape deformation of a 2SR robot and corresponding logarithmic spirals when: (a), (b) one soft VSS is bent by an adjacent LU (Case 1); (c), (d) one soft VSS is bent by the opposite LU (Case 2); (e), (f) both segments are soft (Case 3).

- Motion is initiated by the LU connected to the flexible segment

II: **Flexible-Rigid Configuration with Actuated Rigid End**

- Similar to Case I but with motion initiated by the LU adjacent to the rigid segment
- The resulting spiral differs due to the altered motion constraints

III: **Dual-Flexible Configuration**

- Both segments are flexible
- Either LU can initiate movement
- The spiral parameters accommodate the increased degrees of freedom

Through path analysis and curve fitting, we determine the cardioid radius r and the corresponding ϕ range for each scenario, as listed in Table 5.1. The VSS curvature exhibits an inverse linear relationship with the rolling angle ϕ, enabling reliable tracking of the robot's frame displacement using the cardioid equations. The robot's motion in flexible states is controlled through "soft" velocities $\mathbf{u}_s = [v_1, v_2]^T$, where v_j represents the velocity of the j-th locomotion unit traversing a specific cardioid path.

Remark 6. *This control approach differs fundamentally from the rigid state. By examining each scenario in isolation, we can elucidate the individual contributions to the robot's overall kinematic behaviour. Integrating these insights into a cohesive model yields the kinematic equations that govern the robot's movement.*

Table 5.1: Cardioids Parameters

Cardioid	r	ϕ^{min}	ϕ^{max}
1	0.021	2.42	3.87
2	0.049	2.19	4.09
3	0.043	1.73	4.56

Cardioid 1

The first flexible scenario is characterized by the motion of the j-th LU along a cardioid with velocity v_j, causing an adjacent flexible segment to bend while $\{B\}$ remains stationary. The other locomotion unit is fixed in place and the curvature of the rigid VSS does not change, that is $\dot{x}_b = \dot{y}_b = \dot{\theta}_b = \dot{\kappa}_{3-i} = 0$. Hence, in this scenario, we only need to determine the rate of change in curvature of the flexible segment.

This configuration can be formally described through the following conditions:

- *VS bridge states*: $s_i = 1$, $s_{3-i} = 0$

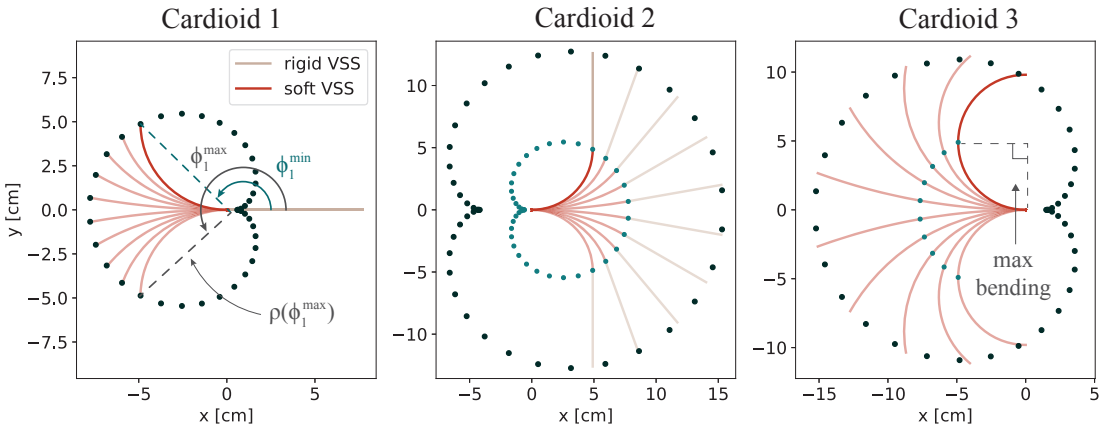

Figure 5.3: Kinematic representation of the soft robot deformation and locomotion unit motion approximated by three distinct cardioid trajectories.

- *LU velocities*: $v_j \neq 0$, $v_{3-j} = 0$
- *Indices*: $i, j \in [1, 2]$, $i = j$.

Curvature of the flexible segment can be derived through the rolling angle of *Cardioid 1* by mapping their corresponding ranges:

$$\begin{aligned} \kappa_i &\approx -\frac{\pi}{2l} + \frac{\pi}{l\Delta\phi_1}\left(\phi_1^{max} - \phi_1\right) \\ \phi_1(\kappa_i) &\approx \phi_1^{min} + \frac{l\Delta\phi_1}{\pi}\left(\frac{\pi}{2l} - \kappa_i\right), \end{aligned} \tag{5.4}$$

where $\Delta\kappa = \frac{\pi}{l}$ and $\Delta\phi_1 = \phi_1^{max} - \phi_1^{min}$.

Remark 7. *The rolling angle rate is proportional to the speed of the object tracing the curve. Note that LU2 is located on the positive side of the x-axis of the frame, while LU1 is on the negative side. Therefore, a positive velocity of LU2 increases the curvature (and decreases ϕ), while a positive velocity of LU1 decreases the curvature (and increases ϕ).*

Differentiating curvature in (5.4) with respect to ϕ_1, we get:

$$\dot{\phi}_1 = (-1)^{j-1}\frac{v_j}{\rho_1} \;\Rightarrow\; \dot{\kappa}_i = (-1)^j \underbrace{\frac{\pi}{l\Delta\phi_1\rho_1}}_{K_1(\kappa_i)} v_j. \tag{5.5}$$

Cardioid 2

The second operational scenario presents a more complex behaviour pattern where motion is initiated by the locomotion unit (LU) connected to the rigid segment, while the other segment remains flexible. Unlike Case I, this configuration results in movement of the robot's central frame $\{B\}$, creating an intricate relationship between the LU motion and the overall robot configuration.

When the LU connected to the rigid VSS moves, it generates bending force that causes the flexible segment to deform. This bending, in turn, forces the robot's body frame to follow a curved path. The locomotion unit in motion traces Cardioid 2, while the body frame traverses Cardioid 1 with its origin at the stationary LU.

This configuration can be formally described through the following conditions:

- *VS bridge states*: $s_i = 1$, $s_{3-i} = 0$
- *LU velocities*: $v_j \neq 0$, $v_{3-j} = 0$
- *Indices*: $i, j \in [1, 2]$, $i \neq j$

The body frame can be localized through its position on Cardioid 1 using (5.3):

$$\begin{bmatrix} \mathbf{p}_b \\ 1 \end{bmatrix} = \mathbf{T}_{bi} \begin{bmatrix} (-1)^{j-1}\rho_1 \cos\phi_1 \\ \rho_1 \sin\phi_1 \\ 1 \end{bmatrix}, \tag{5.6}$$

where $\mathbf{p}_b = [x_b, y_b]^T$ is the body frame's position vector and $\mathbf{T}_{bi}$ represents the coordinate transformation from the stationary LU frame $\{B_i\}$ to global coordinates.

The orientation of the frame $\{B_i\}$ is calculated as:

$$\theta_{bi} = \theta_b + (-1)^i \kappa_i l. \tag{5.7}$$

Figure 5.3 illustrates that the body frame traverses Cardioid 1 with velocity v', which differs from the LU velocity v_j along Cardioid 2. We can establish the relationship between these velocities by leveraging the fact that the curvature rate

remains constant regardless of which cardioid we use for its derivation:

$$\dot{\kappa}_i = -\frac{\pi}{l\Delta\phi_1}\dot{\phi}_1 = -\frac{\pi}{l\Delta\phi_2}\dot{\phi}_2. \tag{5.8}$$

Then, using the definition of the rolling angle velocity from (5.5) we obtain:

$$v' = \underbrace{\frac{\Delta\phi_1}{\Delta\phi_2\rho_2}}_{\lambda_2(\kappa_i)}\rho_1 v_j. \tag{5.9}$$

Now, differentiating (5.6) with respect to ϕ_1 and substituting rolling angle's derivative with (5.9), we find the rate of body frame's displacement:

$$\begin{bmatrix}\dot{x}_b \\ \dot{y}_b\end{bmatrix} = \underbrace{(-1)^{j-1}\frac{\partial \mathbf{p}_b}{\partial \phi_1}\lambda_2(\kappa_i)}_{\mathbf{J}_{j2}(\kappa_i,\theta_b)} v_j. \tag{5.10}$$

The orientation of frame $\{B\}$ changes proportionally to the variation in segment curvature:

$$\Delta\theta_b = (-1)^i \Delta\kappa_i l. \tag{5.11}$$

Consequently, using the previously derived relationships for curvature rate in (5.5), we obtain:

$$\dot{\theta}_b = lK_2(\kappa_i)v_j. \tag{5.12}$$

This mathematical framework captures the complex interplay between the LU motion, segment deformation, and body frame movement, providing a foundation for precise control in this operational mode. The motion patterns in this case differ significantly from Case 1, as the robot exhibits both translational and rotational movements while maintaining a specific segment in its flexible state.

Cardioid 3

The third scenario represents the most versatile configuration of a 2SR robot, where both segments transition to their flexible state simultaneously. This dual-flexible mode enables the robot to achieve more sophisticated shape transformations and

movements, as both segments can actively participate in the deformation process.

In this configuration, when one LU initiates motion, it creates a synchronized bending pattern where both segments deform with *equal curvature rates*: $\dot{\kappa}_1 = \dot{\kappa}_2$. This symmetric behaviour arises from the mechanical coupling between the segments and the uniform distribution of forces through the robot's bridge.

This configuration can be mathematically expressed as:

- *VS bridge states*: $s_i = 1$, $s_{3-i} = 1$
- *LU velocities*: $v_j \neq 0$, $v_{3-j} = 0$
- *Indices*: $i, j \in [1, 2]$

The synchronized deformation of both segments creates a motion pattern where the moving locomotion unit follows Cardioid 3 and the robot's body frame follows Cardioid 1. The generalized coordinates and their derivatives follow the same principles established in the previous cases, with the key distinction being the simultanious bending of both segments. The frame position and orientation can be determined using the previously derived equations, accounting for the combined effect of dual segment flexibility.

Remark 8. *The key distinction in this scenario is that the robot exhibits enhanced compliance and increased degrees of freedom in its movement, allowing for more complex maneuvers while maintaining symmetric deformation patterns. This property can be particularly advantageous in scenarios requiring adaptive shape changes or navigation through constrained environments.*

5.1.3 Unified Kinematic Model

The culmination of our kinematic analysis leads to a unified model that elegantly captures all possible configurations of the 2SR robot through a single comprehensive Jacobian matrix. This unified framework synthesizes the relationships derived from all three cases, providing a complete mathematical description of the robot's behaviour across different operational modes.

The unified model combines the curvature derivatives, body frame motion equations, and orientation changes into a structured Jacobian matrix that adapts to

different soft states of the robot. This adaptability is achieved through the use of binary state variables s_1 and s_2, which act as switches to activate or deactivate different components of the model based on the current configuration.

Assembling equations (5.5)-(5.12), we can express the kinematics of all soft states through the following unified Jacobian matrix:

$$\begin{gathered}
\mathbf{q} = \mathbf{J}(\mathbf{q}, \mathbf{s})\mathbf{u} \\
\mathbf{J}(\mathbf{q}, \mathbf{s}) = [\mathbf{J}_r, \mathbf{J}_s]^\intercal, \quad \mathbf{u} = [\mathbf{u}_r, \mathbf{u}_s]^\intercal \\
\mathbf{J}_s = \begin{bmatrix} s_2 & s_1 \\ s_2 & s_1 \\ s_2 & s_1 \\ s_1 & s_1 \\ s_2 & s_2 \end{bmatrix} \circ \begin{bmatrix} \mathbf{J}_{1n}(\kappa_2, \theta_b) & \mathbf{J}_{2n}(\kappa_1, \theta_b) \\ lK_n(\kappa_2) & lK_n(\kappa_1) \\ -K_m(\kappa_1) & K_n(\kappa_1) \\ -K_n(\kappa_2) & K_m(\kappa_2) \end{bmatrix} \\
(m, n) = \begin{cases} (3,3) & \text{if } s_1 \wedge s_2, \\ (1,2) & \text{otherwise.} \end{cases}
\end{gathered} \tag{5.13}$$

This unified model serves several important purposes:

1. Establishes a single comprehensive mathematical framework that automatically adapts to all possible stiffness states of the robot
2. Captures the complex coupling between bridge segments bending and body frame displacement
3. Enables straightforward computation of both robot's motion and morphological deformation given the LU velocities
4. Facilitates the development of advanced control strategies that can seamlessly transition between different operational modes without discontinuities

The structure of the Jacobian reflects the robot's mechanical architecture, where the Hadamard product (denoted by $\circ$) with the binary state matrix ensures that only the relevant terms are activated based on the current configuration. This mathematical elegance translates to practical advantages in both analysis and control implementation.

5.2 Baseline Controller

The unique capability of the 2SR robot to dynamically transition between rigid and flexible states opens up new possibilities for locomotion control. This section describes a baseline control strategy designed for obstacle-free environments, leveraging the robot's ability to reconfigure its segments in real-time to form various planar shapes.

A block diagram in Fig. 5.4(b) shows that the proposed algorithm comprises three primary components:

- Motion Planner
- Wheel Drive
- Stiffness Controller

Central element of this control system is the **Motion Planner**, which determines the optimal sequence of locomotion modes from the four possible configurations represented by the set $\mathbf{S} = [[0,0],[0,1],[1,0],[1,1]]^\intercal$, where each element defines a unique combination of rigid and flexible states for the two segments.

Remark 9. *This Motion Planner was implemented using a hybrid kinematics framework based on logarithmic spirals and simplified temperature control.*

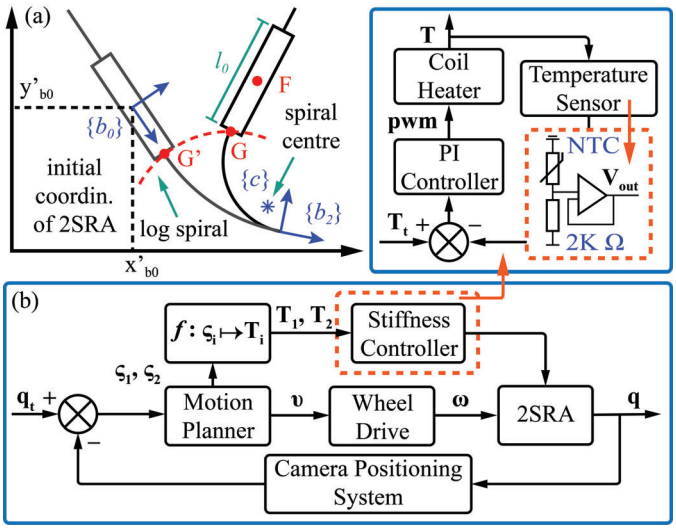

Figure 5.4: (a) The relationship between 2SR robot coordinates and the geometry of the logarithmic spiral I. (b) 2SRA control strategy.

The planning process works as follows:

1. For each possible configuration in $\mathbf{S}$, the system:
   - Calculates the corresponding unified Jacobian matrix
   - Solves the inverse kinematics equations
   - Evaluates the Euclidean distance between the resulting configuration and the target state.
2. The planner selects the configuration that minimizes this distance. However, there's an important practical consideration: frequent transitions between rigid and soft states must be avoided due to the time required for the Field's metal to undergo phase transitions.
3. To address this, the controller maintains the current stiffness configuration as long as the robot is making progress toward its target. Configuration changes are only triggered when the intermediate configuration stops updating effectively.

Algorithm 2: 2SR Robot Motion Planner

Input: Initial configuration $\mathbf{q}_0$, desired configuration $\mathbf{q}_d$
Output: List of optimal stiffness values $\mathbf{S}^*$, list of optimal velocities $\mathbf{V}^*$

$\mathbf{S} \leftarrow$ set of possible VSB stiffness values
$\mathbf{S}^*, \mathbf{V}^* \leftarrow$ empty lists
while $||\mathbf{q}_d - \mathbf{q}|| > 0$ **do**
  for $i = 1$ **to** 4 **do**
    $\mathbf{J} \leftarrow \text{hybridJacobian}(\mathbf{q}_0, \mathbf{q}, \mathbf{S}[i])$
    $\mathbf{v}[i] \leftarrow \mathbf{J}^{-1}\lambda(\mathbf{q}_d - \mathbf{q})$ // λ - feedback gain
    $\dot{\mathbf{q}} \leftarrow \mathbf{J}\mathbf{v}[i]$
    $\mathbf{q}^*[i] \leftarrow \mathbf{q} + \dot{\mathbf{q}}dt$
  $\Delta\mathbf{q}^* \leftarrow ||\mathbf{q}_d - \mathbf{q}^*||$
  $i^* \leftarrow \arg\min_i \Delta\mathbf{q}^*$
  if $i^* \neq i_{prev}$ **then**
    if $||\mathbf{q} - \mathbf{q}^*[i_{prev}]|| > 0$ **then**
      $i^* \leftarrow i_{prev}$
  $\mathbf{q} \leftarrow \mathbf{q}^*[i^*]$
  Add $\mathbf{S}[i^*]$ to $\mathbf{S}^*$; Add $\mathbf{v}[i^*]$ to $\mathbf{V}^*$

The complete **Motion Planner** pseudocode is given in Algorithm 2. The **Wheel Drive** component translates the planned motions into actual wheel velocities using the kinematic model established earlier. This control strategy balances the need for efficient motion with the practical constraints of the phase-transition mechanism, ensuring smooth and effective locomotion while minimizing unnecessary state transitions.

5.3 Experiments

The experimental validation of the proposed control system employed a comprehensive setup designed to track both the robot's kinematics and thermal states, see Fig. 5.5(a). At the core of the experimental platform was a 2SR agent equipped with three Aruco markers strategically positioned - two on the locomotion units and one on the VSB connector. This marker configuration enabled precise tracking of the robot's state and movement throughout the experiments.

Remark 10. *These experiments were conducted using the first generation of the 2SR robot, which featured a monolithic variable stiffness bridge design.*

The tracking system utilized a RealSense camera that captured the positions of all markers in the workspace. The VSB marker served as a reference point for the robot's frame $\{B\}$ position coordinates, while the LU markers provided data for curvature estimation. For analytical simplicity, the system assumed uniform bending along the segments. Additional Aruco markers at the platform corners clearly defined the workspace boundaries, ensuring controlled experimental conditions. Complementing the position tracking, a thermal camera monitored the temperature states of the variable stiffness segments, providing crucial insights into the robot's thermal-mechanical performance. A ground computer handled all data processing and control computations, coordinating the various components of the experimental setup.

5.3.1 Simulation of the Motion Planner

Prior to physical implementation, we conducted simulations in a Python-based environment. The simulation study focused on evaluating two main components of the 2SRA motion model: Forward Kinematics (FK) and Motion Planner (MP).

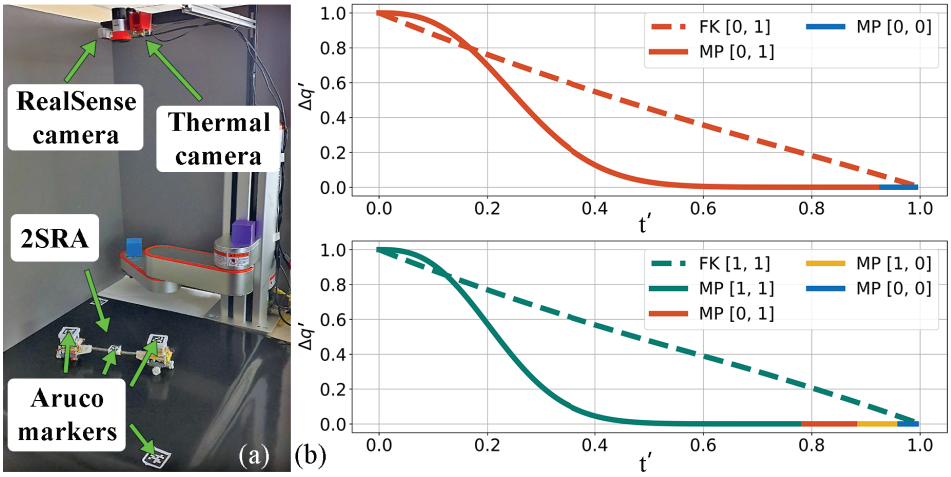

Figure 5.5: (a) Experimental setup. (b) Comparison of error minimization in Forward Kinematics (FK) and Motion Planner (MP) trajectories. Time t and error Δq are normalised with min-max scaling: $t' = (t - t_{min})/(t_{max} - t_{min})$ and $\Delta q' = (\Delta q - \Delta q_{min})/(\Delta q_{max} - \Delta q_{min})$. The last section of the MP graph shows that a 2SR agent sometimes has to switch motion modes to fit into the target: one time (top figure); three times (bottom figure).

Figure 5.5(b) illustrates the error reduction $\Delta q = ||q_t - q||$ in trajectories generated by both methods. For FK testing, we initialized the system with random configurations and applied constant velocity and VSB stiffness settings. This produced linear coordinate progression, establishing baseline trajectories. FK end states then served as target configurations for evaluating the MP's performance.

The Motion Planner exhibited strong asymptotic stability, with the error metric Δq showing consistent exponential decrease across all test cases. During convergence, we observed that curvature parameters typically reached their target values more rapidly than positional coordinates — an expected outcome given the different scales of these parameters.

Our comprehensive evaluation comprised 100 simulation runs, revealing remarkable behavioural consistency. Each trajectory required at most four distinct motion mode transitions to reach its target, invariably concluding in Case 0 (the fully rigid state). This pattern demonstrates an efficient balance between configuration accuracy and minimizing state transitions.

The simulation results confirmed the effectiveness of our control strategy, showing both reliable convergence to target configurations and efficient utilization of the robot's various motion modes. The consistent transition patterns indicate that

the planner successfully manages the system's inherent complexity while respecting practical operational constraints.

5.3.2 Curvature Estimation of the VSS

The hybrid kinematic model of the 2SR agent relies on a constant curvature (CC) approximation for variable stiffness segments. To validate this assumption, we conducted a systematic experimental analysis of the actual curvature distribution along segments under various bending conditions.

Our experimental procedure involved fixing one VSS in its rigid state with its adjacent locomotion unit secured to the plane. The other segment, maintained in the flexible state, was methodically deformed through a comprehensive range of curvatures from $-\pi$ to π, allowing us to characterize the segment's behaviour across its complete motion range.

Thermal imaging provided crucial insights, as illustrated in Figure 5.6(a), where bright-colored regions clearly indicate high-temperature zones of molten LMPA within the segment's shell. Using the OpenCV library, we developed an image processing pipeline that generated binary images highlighting segment contours and constructed a median curve, as shown in Figure 5.6(b).

Our analysis compared three different representations of the segment's shape, depicted in Figure 5.6(c): the raw median curve extracted from imaging data, its smoothed version, and the constant curvature approximation. By calculating the gradient at each point along the smoothed median curve, we obtained a detailed distribution of curvatures throughout the segment. Each test configuration was repeated five times to ensure statistical reliability.

Results presented in Figure 5.7(a) reveal the relationship between the mean curvature (MC) of the VSS median curve and the constant curvature calculated from Aruco marker positions. For small deformations, these measurements showed strong agreement, while larger bending angles introduced more pronounced differences. Quantitative analysis yielded a mean square error of 9.09 m^{-1} between CC and MC measurements, with an average standard deviation of 14.39 m^{-1} in curvature distribution along the segment.

Significantly, curvatures in the range of 0-15 m^{-1} exhibited relatively small vari-

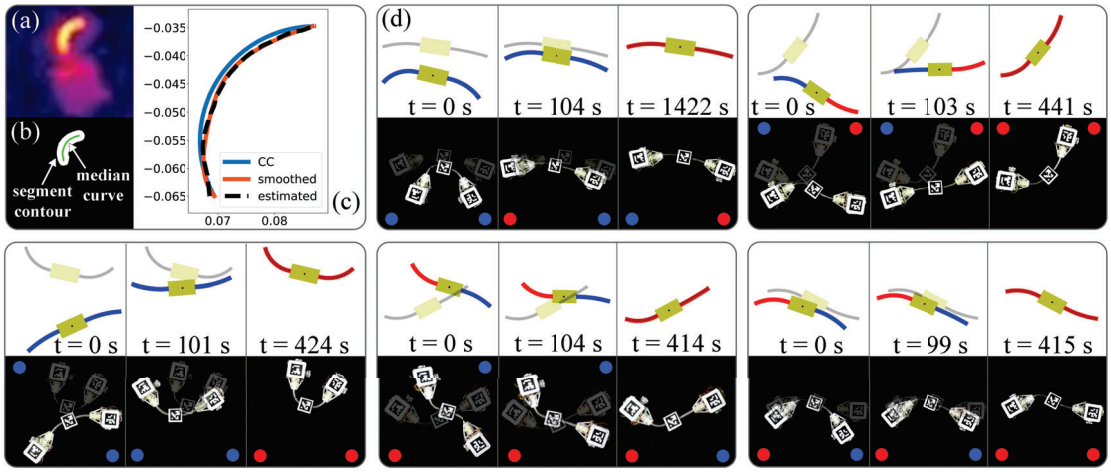

Figure 5.6: (a) Thermal image of a soft VSS. The bright-coloured area shows the high-temperature zone of the molten LMPA inside the segment's shell. (b) Contours and a median curve of the bent segment extracted from a thermal image. (c) Comparison of the median curve, its smoothed version and the approximated curve with constant curvature. (d) Five scenarios of the pose-shape formation when a robot has a task to reach a target configuration. The top row shows the 2SRA simulation, and the bottom row is the real-case motion. Blue colour represents a soft segment while a rigid segment is red. A faded image shows a target; the bright one is the current configuration. The first case takes more time because the agent switched stiffness more than one time.

ations relative to segment lengths. This finding strongly supports the validity of the CC assumption for representing VSS bending within this operational range, confirming the appropriateness of our modeling approach for practical applications.

These results not only validate our modeling assumptions but also provide valuable insights into the mechanical behaviour of variable stiffness segments under different deformation conditions.

5.3.3 Pose-Shape Formation

The culmination of our experimental validation focused on Pose-Shape Formation tasks, where the 2SR robot needed to achieve specific target configurations through coordinated planar motion and segment deformation. These experiments comprehensively tested the system's ability to manage multiple degrees of freedom while orchestrating transitions between rigid and flexible states.

We conducted five distinct experiments with varied initial and target configurations. Target positions were established through manual robot deformation, with precise configuration measurements captured via the RealSense camera system.

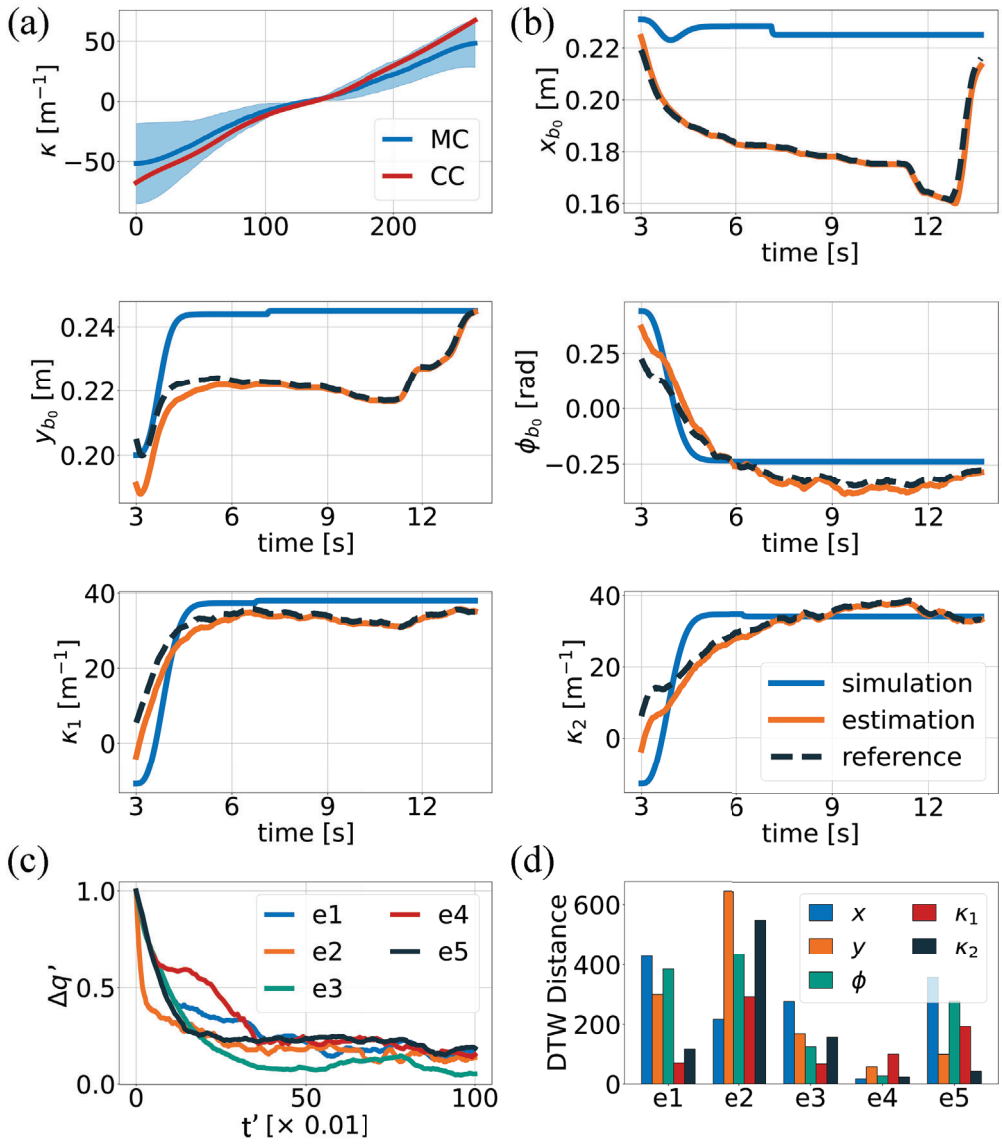

Figure 5.7: (a) Comparison of the VSS constant curvature (CC) approximation and mean curvature (MC) of the segment arc extracted from thermal images. The solid-coloured area demonstrates curvature distribution along the segment arc. (b) Comparison of the configuration trajectories obtained during the Pose-Shape Formation experiment (third case) and the corresponding simulation. Reference is the configuration returned by a Motion Planner and further supplied to the robot; the Estimated value is the configuration measured via camera and Aruco markers. (c) Minimization of the normalised error $\Delta q'$ during the task execution. (d) Quantified difference (DTW distance) between the configuration trajectories from the Pose-Shape Formation experiments and corresponding simulations.

To enable rigorous comparison between theoretical predictions and practical performance, identical scenarios were first simulated and then implemented on the physical platform.

As visualized in Figure 5.6(d), the trials demonstrated diverse motion patterns and execution durations. Simulated and physical implementations exhibited similar movement sequences, despite some inevitable practical differences. Throughout each trial, we continuously monitored two key configurations: the reference configuration determined by the Motion Planner and the estimated configuration measured through the camera system.

The detailed trajectory comparison presented in Figure 5.7(b), revealed significant insights into system behaviour. A particularly notable observation concerned the locomotion units during deformation phases. When VSB segments transitioned into a flexible state, the resulting slack and tilt in the LUs occasionally compromised wheel-surface contact, causing deviations from simulated trajectories. This effect was especially prominent in positional coordinates due to their smaller scale relative to curvature measurements.

The system's convergence behaviour, illustrated in Figure 5.7(c), demonstrated consistent progression toward target configurations. To optimize performance and prevent unnecessary state transitions, we implemented termination thresholds:

- Position coordinates ($\langle x_{b_0}, y_{b_0} \rangle$): < 0.01
- Curvature values ($\langle \kappa_1, \kappa_2 \rangle$): < 4.

We quantified overall performance across all experiments using Dynamic Time Warping (DTW) distance between simulated and experimental trajectories, as shown in Figure 5.7(d). Despite observed deviations, error margins remained within acceptable bounds, confirming the effectiveness of our hybrid model in practical applications.

The wheel slip phenomenon suggests potential mechanical refinements, particularly in locomotion unit design. Increasing the mass or incorporating additional steel bars within the LUs could enhance ground contact stability during deformation phases, potentially reducing trajectory deviations and improving system precision.

These experimental results validate the practical viability of our proposed hybrid model and control strategy while identifying specific areas for mechanical optimization in future iterations.

5.3.4 Manual Object Manipulation

The 2SRA's unique combination of variable stiffness and mobile locomotion enables a diverse range of manipulation tasks that showcase the system's versatility. The robot's ability to dynamically transition between rigid and flexible states makes it particularly well-suited for adaptive object interaction and manipulation scenarios.

As demonstrated in Figure 5.8(a), the 2SRA exhibits remarkable adaptability when interacting with curved surfaces. The robot can approach a cylindrical object and selectively soften one segment, allowing it to conform precisely to the object's curvature. This capability demonstrates a key advantage over traditional rigid mobile robots, which typically lack the ability to adapt their shape to irregular objects or surfaces.

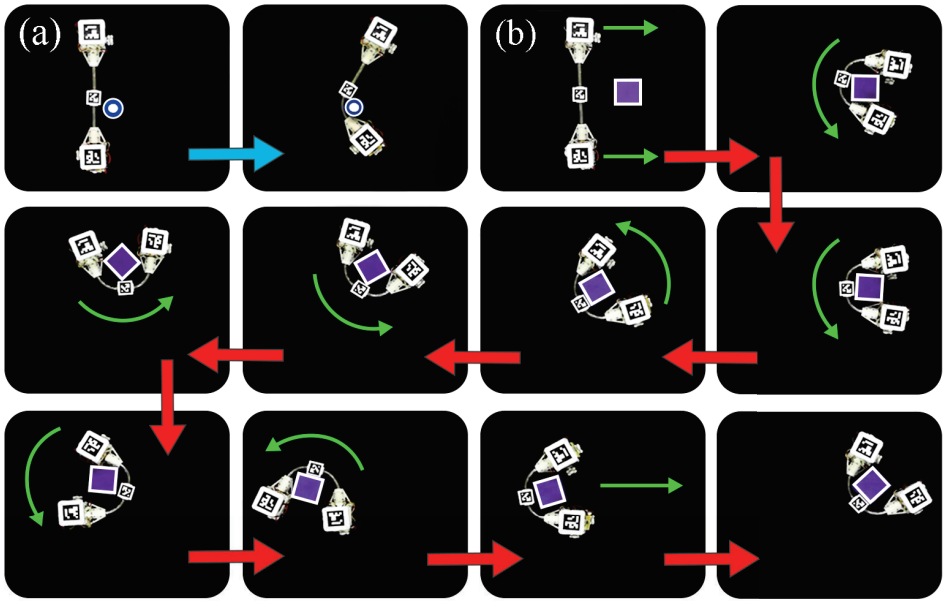

Figure 5.8: 2SR agent performing objects handling tasks: (a) conforming to an object with a cylindrical shape. (b) gripping and moving a cube on the plane.

The sequence shown in Figure 5.8(b) illustrates a more complex manipulation task involving multiple state transitions. The process follows several distinct phases:

1. Initial approach to the target object
2. Transition of both segments to the flexible state
3. Conformable grasping of the cubic object

4. Return to the rigid state while maintaining the grasp
5. Free planar movement while securely holding the object

Remark 11. *The object grasping and manipulation demonstrated here were performed using manual control inputs.*

This demonstration highlights the robot's ability to seamlessly combine soft manipulation with hard mobility, enabling it to not only grasp objects but also transport them effectively across the workspace.

The demonstrated capabilities represent only a fraction of the 2SRA's potential applications. By bridging the gap between conventional rigid robots and soft robotics, the system opens up possibilities across various domains. The ability to dynamically alternate between rigid and soft states, combined with mobile capabilities, suggests applications in:

- Adaptive manufacturing environments
- Search and rescue operations
- Confined space exploration
- Delicate object handling
- Collaborative human-robot interaction scenarios.

5.4 Multi-Modal Motion and Shape Control

The development of an advanced controller for the 2SRA required a sophisticated approach capable of handling both continuous dynamics and discrete stiffness transitions. Model Predictive Control (MPC) emerged as an ideal choice for this application due to several key advantages:

1. *Constraint Handling*: the 2SR robot operates under multiple physical constraints, including wheel speed limitations and actuator bounds. MPC naturally incorporates these constraints into the optimization problem.
2. *Multi-Variable Control*: The system requires simultaneous control of position, orientation, and segment curvatures. MPC's ability to handle Multiple

Input Multiple Output (MIMO) systems makes it well-suited for this task.

3. *Preview Capability*: By optimizing over a prediction horizon, MPC can anticipate future state trajectories, particularly valuable during mode transitions and complex maneuvers.

Having established the robot's operational modes through hybrid kinematics, we implement a comprehensive control strategy comprising four distinct model predictive controllers (MPC) corresponding to each possible stiffness configuration $\mathbf{s} \in \mathbf{S}$, where $\mathbf{S} = \{[0,0],[1,0],[0,1],[1,1]\}$:

- **MPC1** (Rigid Mode): both segments are rigid
- **MPC2** (Flexible Mode 1): first segment flexible, second rigid
- **MPC3** (Flexible Mode 2): first segment rigid, second flexible
- **MPC4** (Flexible Mode 3): both segments are flexible

For a prediction horizon N, the *MPC optimization problem* is formulated as:

$$\begin{aligned} \text{minimize} \quad & \sum_{k=0}^{N} \tilde{\mathbf{q}}_k^\intercal \mathbf{Q} \tilde{\mathbf{q}}_k + \sum_{k=0}^{N} \mathbf{u}_k^\intercal \mathbf{R} \mathbf{u}_k \\ \text{subject to} \quad & \tilde{\mathbf{q}}_k = \mathbf{q}_k - \mathbf{q}_{ref} \\ & \mathbf{q}_{k+1} = \mathbf{q}_k + \mathbf{J}(\mathbf{q}_k, \mathbf{s}_k)\mathbf{u}_k \\ & |w_i| \leq w_{max},\ i = 1...4, \end{aligned} \tag{5.14}$$

where

- $\mathbf{q}_k$ is the robot's state vector
- $\mathbf{q}_{ref}$ is the robot's reference state
- $\mathbf{u}_k$ is the control velocity vector
- $\mathbf{Q}$ and $\mathbf{R}$ are positive definite weighting matrices
- $\mathbf{s}_k$ is the stiffness configuration
- $\mathbf{J}(\mathbf{q}_k, \mathbf{s}_k)$ is the Jacobian defined in (5.13)
- w_i represents individual wheel velocities bounded by w_{max}

Remark 12. *Each controller follows the same general MPC framework while utilizing mode-specific kinematics derived from the hybrid cardioid-based model.*

The MPC implementation utilizes the GEKKO optimization framework, solving the constrained optimization problem at each time step and applying the first control input of the optimal sequence. The prediction horizon and weighting matrices are tuned for each motion mode to achieve the desired performance characteristics.

Remark 13. *To balance computational efficiency with control performance, we implemented a relatively short prediction horizon (11 steps) for each MPC controller. It was empirically determined that this value maintains sufficient predictive capability while enabling real-time execution on our hardware platform.*

The derived control formulation allows for:

- Explicit handling of state and input constraints
- Preview of future trajectory evolution
- Smooth transitions between different motion modes
- Balance between tracking performance and control effort

While the mode-specific MPC controllers handle the continuous dynamics and optimization, a higher-level control structure is needed to manage the discrete transitions between different stiffness states and coordinate the overall robot behaviour. This led to the development of a comprehensive **Motion & Morphology Controller (MMC)** that orchestrates both the continuous motion control and discrete stiffness state transitions.

The integrated control framework combines motion planning with morphology adaptation through a hierarchical structure. The controller continuously evaluates the target configuration to determine optimal stiffness and corresponding motion commands. This supervisory framework operates through two key mechanisms:

1. *Stiffness State Management*: Determines required segment stiffness based on target configuration. When the shape error between current and target curvatures exceeds a predetermined threshold $\Delta\kappa_{min}$, the controller initiates selective softening of the appropriate segments.

2. *Motion Coordination*: Activates the appropriate MPC controller based on the current stiffness state.

Remark 14. *This approach optimizes system performance by maintaining segment rigidity by default and initiating transitions only when necessary for shape control.*

The complete controller formulation is provided in Algorithm 3.

Algorithm 3: Motion & Morphology Control (MMC)

Input: current configuration $\mathbf{q} = [x, y, \theta, \kappa_1, \kappa_2]^T$, target configuration $\mathbf{q}_t$
Result: $\mathbf{u}$

Initialize velocity vectors: $\mathbf{u}_r \leftarrow [0, 0, 0]$, $\mathbf{u}_s \leftarrow [0, 0]$
Initialize target stiffness: $\mathbf{s}_\mathrm{t} \leftarrow [0, 0]$
for $i \in 1, 2$ **do**
    if $|\kappa_i - \kappa_{i,t}| > \Delta\kappa_{min}$ **then**
        $\mathbf{s}_\mathrm{t}[i] \leftarrow 1$
while *not* ($\mathbf{s}_t = [0, 0]$ ***and*** `close2Pose`$(\mathbf{q},\ \mathbf{q}_t)$) **do**
    if $\mathbf{s}_t \neq [0, 0]$ ***and*** `close2Shape`$(\kappa_1, \kappa_2, \mathbf{q}_t)$ **then**
        $\mathbf{s}_\mathrm{t} \leftarrow [0, 0]$;
        $\mathbf{u} \leftarrow [0, 0, 0, 0, 0]$; `// reset velocities`
    if $\mathbf{s}_t = [0, 0]$ **then**
        $\mathbf{u}_r,\ \mathbf{q} \leftarrow \mathrm{mpc1}(\mathbf{q},\ \mathbf{q}_t, \mathbf{u}_r)$
    else if $\mathbf{s}_t = [1, 0]$ **then**
        $\mathbf{u}_s,\ \mathbf{q} \leftarrow \mathrm{mpc2}(\mathbf{q},\ \mathbf{q}_t, \mathbf{u}_s)$
    else if $\mathbf{s}_t = [0, 1]$ **then**
        $\mathbf{u}_s,\ \mathbf{q} \leftarrow \mathrm{mpc3}(\mathbf{q},\ \mathbf{q}_t, \mathbf{u}_s)$
    else
        $\mathbf{u}_s,\ \mathbf{q} \leftarrow \mathrm{mpc4}(\mathbf{q},\ \mathbf{q}_d, \mathbf{u}_s)$
    $\mathbf{u} \leftarrow [\mathbf{u}_r, \mathbf{u}_s]$;
    Send velocities to the robot;
    Update stiffness states via FSM Controller

The controller executes in a continuous loop, performing the following key operations:

1. Evaluates shape error to determine required segment stiffness
2. Selects appropriate MPC controller based on stiffness state
3. Generates optimal velocity commands

4. Synchronizes motion execution with stiffness transitions through FSM controller formulated in Algorithm 1

5. Monitors convergence to target configuration

This integrated approach ensures smooth coordination between shape-changing behaviours and locomotion while maintaining stability during transitions. The FSM controller manages the physical stiffness transitions, preventing motion during critical phase changes.

5.5 Summary

This chapter has presented a comprehensive control framework for the 2SR robot, addressing the unique challenges posed by its hybrid rigid-flexible nature. Our development progressed from fundamental kinematic modeling to sophisticated control strategies, culminating in the advanced *Motion & Morphology Controller*.

Key contributions and findings include:

Hybrid Kinematics

- Development of a unified kinematic model capturing both rigid and flexible stiffness states
- Identification of three distinct flexible operational scenarios based on segment stiffness combinations
- Validation of the constant curvature assumption for flexible segments within practical operational ranges
- Mathematical characterization of the robot's dynamic morphology using logarithmic spiral and cardioid path models for locomotion unit motion

Control Architecture

1. *Baseline Controller*:
    - Implementation of an efficient motion and stiffness planner for obstacle-free environments
    - Integration of wheel drive and simplified stiffness control systems

- Demonstration of reliable convergence to target configurations

2. *Advanced Controller*:
    - Development of mode-specific Model Predictive Controllers
    - Implementation of a hierarchical control framework managing both continuous motion dynamics and discrete stiffness state transitions
    - Incorporation of physical constraints and multi-objective optimization criteria

Experimental Validation

- Successful demonstration of precise pose-shape formation capabilities across multiple configurations
- Verification of object manipulation functionalities, including conformable full-body grasping and secure transport
- Quantitative performance analysis through detailed trajectory comparison and Dynamic Time Warping metrics
- Identification of practical considerations, particularly regarding wheel-surface contact during flexible mode operations

The experimental results and theoretical developments presented in this chapter demonstrate both the potential and challenges of hybrid rigid-flexible robotic systems. Our findings suggest that integrating variable stiffness elements with conventional mobile robotics creates opportunities for enhanced adaptability and manipulation capabilities beyond what purely rigid or purely soft systems can achieve independently.

The successful implementation of the hierarchical Motion & Morphology Controller, particularly its ability to manage discrete stiffness transitions while maintaining stable motion and shape control, represents a significant advancement in hybrid robot control. However, several areas for improvement emerged during our investigation. The observed wheel slip during flexible-state operations indicates that mechanical refinements could enhance system performance. Additionally, the current control framework would benefit from more sophisticated state estimation

and adaptive parameter tuning.

The developed control framework establishes a foundation for:

1. Expanded application scenarios in complex, adaptive manipulation tasks
2. Integration of advanced sensing and environmental planning capabilities
3. Optimization of mechanical design, particularly for locomotion unit stability during morphological transitions
4. Development of sophisticated manipulation strategies that fully leverage the system's hybrid nature

Limitations and Future Plans

Our analytical model operates under several significant assumptions and limitations, resulting in a kinematic framework that captures only a subset of the robot's actual dynamics. This abstraction, while effective for initial control implementation, constrains our ability to fully leverage the 2SR robot's inherent capabilities. The control framework is consequently more limited than the robot's physical potential would allow.

For instance, a 2SR robot can translate laterally in a flexible mode because very small bending forces occur along the robot's elongated axis - a capability our current model does not reflect. Similarly, the three derived cardioid-based motion patterns represent only a fraction of the possible movement and deformation available in flexible states. The rich continuum of configurations accessible through variable stiffness actuation extends far beyond our current mathematical characterization.

Additional limitations emerge from our simplified treatment of wheel-surface interactions, particularly during stiffness transitions and deformation phases. The model inadequately accounts for the complex friction and slip patterns that develop as the robot's weight distribution shifts during morphological changes. These simplified assumptions introduce discrepancies between predicted and actual behaviour, especially in scenarios involving substantial deformation.

The performance of the 2SR robot could be considerably enhanced by combin-

ing our analytical model with machine learning techniques. Reinforcement learning (RL) offers particularly promising avenues for enhancing the 2SR robot's capabilities beyond the limitations of our analytical model. Several specific implementations could address the current framework's constraints:

Hybrid Model-Based/Model-Free Architecture

The unique hybrid nature of our 2SR robot presents an ideal case for combining model-based control with model-free RL techniques. The analytical kinematics could provide a structured baseline for stable behaviour, while RL components could discover and exploit emergent dynamics not captured in our mathematical formulation:

- The model-based controller could handle well-understood rigid-state locomotion and basic shape transitions
- RL agents could progressively learn complex flexible-state behaviours, including lateral translation and intricate deformation patterns beyond the cardioid approximations
- Gaussian Process-based model learning could continuously refine the system's understanding of state transition dynamics during morphological changes

Hierarchical Reinforcement Learning Framework

The inherent structure of the 2SR robot—with its discrete stiffness states and continuous motion control—naturally maps to a hierarchical RL architecture:

- High-level RL policies could learn optimal stiffness transition sequences for different tasks and environmental conditions
- Mid-level policies could discover effective shape configurations for specific manipulation scenarios
- Low-level controllers could optimize wheel actuation patterns to minimize slip and maximize traction during flexible-state operations

This hierarchy aligns with our existing control architecture while enhancing its adaptability through learning.

Learning Physical Interaction Dynamics

A critical limitation in our current model involves wheel-surface interactions during deformation. RL could directly address this through:

- Learning contact-aware policies that anticipate and compensate for wheel slip
- Developing adaptive friction models that adjust motor commands based on detected surface conditions
- Discovering optimal weight distribution strategies during morphological transitions to maintain traction

By incorporating these RL approaches, we could transcend the limitations of our analytical model while maintaining stable, interpretable control. The resulting system would progressively discover and exploit the full spectrum of capabilities inherent in the 2SR robot's hybrid rigid-flexible design, particularly in complex manipulation scenarios requiring adaptive morphology beyond predefined motion patterns.

Chapter 6

Grasping and Manipulating Curvilinear Objects

6.1 Problem Formulation

The major advantage of a 2SR robot lies in its ability to simultaneously move and adapt its morphology by dynamically altering stiffness and motion modes. Most significantly, it possesses the unique capability of *full-body grasping* — enveloping objects with its body to create secure, conformable grasps. This distinctive characteristic establishes a natural application domain: grasping and manipulating objects of arbitrary shapes. Through its morphology-changing capabilities, the robot can reconfigure its body to envelope objects in a hugging manner, performing versatile and adaptive grasps impossible for conventional rigid manipulators.

In this chapter, we explore scenarios where the robot must grasp objects of arbitrary shapes and transport them to designated locations. This application presents several interrelated challenges that must be systematically addressed:

Problem 6.1.1 (Implementation of full-body grasping)**.** *Determine the optimal grasping configuration and procedural sequence that enables the robot to securely grasp objects while minimizing disturbance to the target. This includes identifying appropriate stiffness transitions, approach trajectories, and final morphological adaptations that ensure both grasp security and efficient configuration for subsequent manipulation.*

Problem 6.1.2 (Transport optimization)**.** *Determine the manipulation and control strategies that ensure the successful transport of grasped objects.*

A contact between a 2SR robot and a manipulandum can be described as a mapping between forces exerted by the robot at the points of contact and the resulting wrenches at the object's center of mass. This relationship captures how the robot's applied forces translate into object motion during manipulation tasks. We represent velocities and twists at both the contacts and on the object using coordinate frames attached to the contact locations and the object's reference point, with the assumption that contact points remain fixed relative to the object during manipulation.

The modeling of grasp and manipulation has been conducted based on the following *assumptions*:

1. The system operates in a planar (2D) environment, constraining all forces, torques, and velocities to the horizontal plane
2. The robot achieves manipulation through continuous environmental constraint rather than traditional firm grasping:
    - The robot cannot pull the object backwards
    - Lateral object motion is limited due to the nature of the constraint-based manipulation
    - Manipulation primarily relies on a combination of pushing forces and geometrical constraint through body envelopment
3. Surface friction is sufficient to maintain stable contact during manipulation.
4. No slippage occurs between robot and object, ensuring that contact points maintain fixed positions relative to the object's surface
5. Contact forces are effectively transmitted through the robot's variable stiffness structure without significant internal deformation that would compromise the manipulation accuracy
6. Quasi-static conditions apply throughout the manipulation process, allowing to neglect inertial effects and consider force equilibrium at each configuration

6.2 Robot-Object Contact Model

The *manipulandum* is a right prism with an arbitrarily shaped closed curve as its base. During manipulation, the 2SR robot establishes contact with this rigid object primarily through its variable-stiffness bridge, which conforms to external surfaces along its flat side, as illustrated in Fig. 6.1. This conformable interaction represents a key advantage of the 2SR platform, allowing it to adapt to diverse object geometries.

While the VSB may not achieve perfect surface contact with the object's entire contour due to geometric limitations and material properties, it establishes sufficient contact area to develop a secure, stable grasp. This adaptive contact pattern creates a mechanical constraint that effectively couples the robot and object motion. Under our assumption of no slip at the contact interface, this configuration enables a direct kinematic mapping between the desired object twists and the corresponding robot control velocities:

$$\mathbf{u}_r = \mathrm{Ad}_{\mathbf{T}_{bo}} \mathbf{u}_o, \tag{6.1}$$

where $\mathbf{u}_r \in \mathbb{R}^3$ represents the robot's "rigid" velocity vector (containing linear and angular components), $\mathbf{u}_o \in \mathbb{R}^3$ represents the object's velocity vector, and $\mathrm{Ad}_{\mathbf{T}_{bo}}$ is the adjoint transformation that maps between these two coordinate frames. This transformation is expressed as:

$$\mathrm{Ad}_{\mathbf{T}_{bo}} = \begin{bmatrix} \mathbf{R}(\theta_{bo}) & \begin{bmatrix} {}^b y_o & -{}^b x_o \end{bmatrix}^\intercal \\ 0 & 1 \end{bmatrix}. \tag{6.2}$$

In this formulation, $\mathbf{R}(\theta_{bo})$ is the rotation matrix representing the orientation difference between the robot's body frame and the object frame, while ${}^b x_o$ and ${}^b y_o$ are the Cartesian coordinates of the object's center of mass with respect to the robot's body frame. The parameter θ_{bo} captures the relative angular orientation between these frames.

This kinematic mapping is particularly important for manipulation planning, as it allows us to determine the required robot motion that will induce a desired object motion. The conformable nature of the VSB ensures that this relationship remains

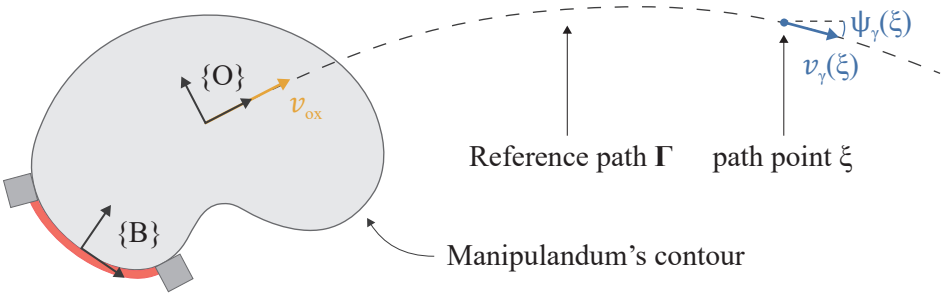

Figure 6.1: Schematic illustration of a 2SR robot transporting an object of arbitrary shape along a prescribed path..

valid across a range of object geometries, provided the contact is maintained. The efficacy of this contact model depends on maintaining sufficient normal forces at the interface to prevent slippage. This is achieved through appropriate full-body grasping and careful planning of the manipulation sequence to ensure stable contact throughout the task execution.

6.3 Three-phase Full-body Grasping Strategy

To implement *full-body grasping* ability in a 2SR robot, several aspects should be considered. First, we need to determine how the robot should be positioned relative to the object for grasping - this defines the grasp configuration. Based on this grasp configuration, we can then establish a target pose for the path planning (*navigation* is discussed in detail in Chapter 7) that allows the robot to smoothly transition into the grasping motion.

To achieve this objective, we establish a *three-phase grasping strategy*: approach with default shape, grasp without contact, and final contact. The final contact configuration $\mathbf{q}_f = [x_f, y_f, \theta_f, \kappa_{1f}, \kappa_{2f}]^\intercal$ is derived from the object geometry by satisfying several crucial conditions: maintain a suitable distance to the object for stable grasping, maximize shape conformity between the robot and the object, and ensure proper robot orientation to facilitate object's translation in the desired direction.

With object contour parameterized by $\varsigma \in \{0...1\}$, this configuration can be established through the following procedure:

1. From the object's initial position on the transport path, extend a line in the

direction opposite to the local motion direction vector.

2. Locate the intersection point ς_0 between this extended line and the object's contour: $(x_f, y_f) = (x_c(\varsigma_0), y_c(\varsigma_0))$.

3. The orientation component $\theta_f = \theta_c(\varsigma_0)$ is set to the tangent angle at the contour intersection point.

4. Each segment curvature is computed from its contact region:

$$\kappa_{jf} = \frac{1}{n} \sum_{i=1}^{n} \kappa_c(\varsigma_i), \tag{6.3}$$

where $\kappa_c(\varsigma_i)$ is the contour curvature at the point ς_i, with n points spanning VSS arc length.

Problem 6.3.1. *While the final grasp requires full conformity to the object's contour, direct approach to this configuration risks object disturbance and oscillations.*

Therefore, we additionally introduce an intermediate grasp $\mathbf{q}_g$ and pre-grasp pose $\mathbf{x}'_r$ by progressively offsetting from the final contact position by margin δ:

$$\begin{aligned} \mathbf{q}_g &= [x_f + \delta \sin(\theta_f), y_f - \delta \cos(\theta_g f), \theta_f, \kappa_{1f}, \kappa_{2f}]^\intercal \\ \mathbf{x}'_r &= [x_f + 2\delta \sin(\theta_f), y_f - 2\delta \cos(\theta_g f), \theta_f]^\intercal. \end{aligned} \tag{6.4}$$

6.4 Object Path Tracking

Once the object has been grasped by the robot, it needs to be transported along a predefined path. For this purpose, we implemented an MPC-based pure pursuit algorithm for object path tracking. The pure pursuit controller is a geometric path-tracking approach that calculates steering commands to guide the object along the reference trajectory.

Definition 6.4.1. *Let a set of points* $\mathbf{\Gamma} = \{(x_\gamma(n), y_\gamma(n)) \mid n \in [0, N]\}$ *denote the reference path, where* N *is the total number of points. Then, the trajectory state at each point* n *is defined as:*

$$\boldsymbol{\chi}_\gamma(n) = [\underbrace{x_\gamma(n), y_\gamma(n), \psi_\gamma(n)}_{pose\ \mathbf{x}_\gamma}, v_\gamma(n)]^\intercal, \tag{6.5}$$

where $x_\gamma(n), y_\gamma(n)$ are Cartesian coordinates of $\mathbf{\Gamma}(n)$, $\psi_\gamma(n)$ is the heading angle, and $v_\gamma(n)$ is the prescribed velocity.

Remark 15. *The object reference frame $\{O\}$ is assigned such that its initial orientation θ_o coincides with the heading direction at the beginning of the reference path $\psi_\gamma(0)$. Therefore, in the object control velocity vector $\mathbf{u}_o = [v_{ox}, v_{oy}, \omega_o]^\intercal$, v_{ox} represents the heading velocity that we want to keep constant.*

At each MPC update, we generate a reference trajectory over the prediction horizon of N steps. Denoting the last traversed point on the path curve as n_0, the reference trajectory is initialized with:

$$\boldsymbol{\chi}'(0) = [\mathbf{x}_\gamma(n_0), v_{ox}]^\intercal, \tag{6.6}$$

where v_{ox} is the current heading velocity of the object. For subsequent points in the prediction horizon $k \in \{1...N\}$ with time step duration Δt, we calculate the accumulated travel distance:

$$d(k) = \sum_{i=0}^{k-1} |v'(i)| \Delta t. \tag{6.7}$$

The projected path index at step k is then computed as:

$$n_k = n_0 + \left\lfloor \frac{d(k)}{L} \right\rceil, \tag{6.8}$$

where L is the lookahead distance and $\lfloor \cdot \rceil$ denotes rounding. The object's reference state is assigned according to this index:

$$\boldsymbol{\chi}'(k) = \begin{cases} \boldsymbol{\chi}_\gamma(n_k), & \text{if } n_k < N \\ \boldsymbol{\chi}_\gamma(n), & \text{otherwise.} \end{cases} \tag{6.9}$$

Having generated the reference trajectory, we linearize the object's dynamics for use in the MPC controller. The object's motion can be described by a discrete-time linear state-space model around the reference trajectory. At each time step

k, the linearized system dynamics is given by:

$$\tilde{\mathbf{x}}(k+1) = \mathbf{A}(k)\tilde{\mathbf{x}}(k) + \mathbf{B}(k)\tilde{\mathbf{u}}(k), \tag{6.10}$$

where

- $\tilde{\mathbf{x}} = \mathbf{x}_o - \mathbf{x}'$ is the object's pose error
- $\tilde{\mathbf{u}} = \mathbf{u}_o - \mathbf{u}'$ denotes the control velocity error
- $\mathbf{u}' = [v'(k), 0, 0]^\intercal$ is the reference control input that maintains forward motion along the path

The time-varying system matrices $\mathbf{A}(k)$ and $\mathbf{B}(k)$ are computed as:

$$\begin{aligned} \mathbf{A}(k) &= \begin{bmatrix} 1 & 0 & -v'(k)\sin(\psi_{ref}(k))\Delta t \\ 0 & 1 & v'(k)\cos(\psi_{ref}(k))\Delta t \\ 0 & 0 & 1 \end{bmatrix} \\ \mathbf{B}(k) &= \begin{bmatrix} \Delta t\cos(\psi_{ref}(k)) & -\Delta t\sin(\psi_{ref}(k)) & 0 \\ \Delta t\sin(\psi_{ref}(k)) & \Delta t\cos(\psi_{ref}(k)) & 0 \\ 0 & 0 & \Delta t \end{bmatrix} \end{aligned} \tag{6.11}$$

Here, $\mathbf{A}(k)$ captures how the object's state evolves over time without additional control inputs, while $\mathbf{B}(k)$ represents how control inputs affect the state. The matrices account for the nonlinear coupling between orientation and position through appropriate trigonometric terms.

Local linearization around the reference trajectory approximates the nonlinear system dynamics, allowing the MPC optimization problem to be formulated as:

$$\begin{aligned} \underset{\tilde{\mathbf{x}},\tilde{\mathbf{v}}}{\text{minimize}} \quad & \sum_{k=0}^{N-1} (\tilde{\mathbf{x}}_k^\intercal \mathbf{Q}\tilde{\mathbf{x}}_k + \tilde{\mathbf{u}}_k^\intercal \mathbf{R}\tilde{\mathbf{u}}_k + \Delta\tilde{\mathbf{u}}_k^\intercal \mathbf{R_d}\Delta\tilde{\mathbf{u}}_k) + \tilde{\mathbf{x}}_N^\intercal \mathbf{Q_f}\tilde{\mathbf{x}}_N \\ \text{subject to} \quad & \tilde{\mathbf{x}}_0 = \mathbf{x}_o - \mathbf{x}'(n_0) \\ & \tilde{\mathbf{x}}_{k+1} = \mathbf{A}_k\tilde{\mathbf{x}}_k + \mathbf{B}_k\tilde{\mathbf{u}}_k \end{aligned} \tag{6.12}$$

where $\mathbf{x}_o = [x_o, y_o, \theta_o]^\intercal$ is the current object pose.

The cost function comprises:

- Position and orientation tracking errors penalized by $\mathbf{Q}$
- Control effort penalties through $\mathbf{R}$
- Control smoothness constraints via input rate penalties $\mathbf{R_d}$
- Terminal state penalty $\mathbf{Q_f}$ that ensures stability at the prediction horizon's end

The weighting matrices $\mathbf{Q}$, $\mathbf{R}$, $\mathbf{R_d}$, $\mathbf{Q_f} \succeq 0$ are carefully tuned to balance path tracking accuracy against smooth, feasible motion that respects the physical constraints of the robot-object system.

After solving this optimization problem at each control iteration, we extract the optimal control deviation $\tilde{\mathbf{u}}$ and combine it with the reference input to obtain the commanded object velocity: $\mathbf{u}_o = \tilde{\mathbf{u}} + \mathbf{u}'$. This object velocity command is then transformed into robot control commands using the kinematic mapping established in the contact model section (Equation (6.1)), ensuring coordinated manipulation that guides the object precisely along the desired path.

The MPC-based pure pursuit approach offers several advantages for our specific application, including the ability to anticipate path curvature, optimize motion over a future horizon, and explicitly incorporate the physical constraints of the 2SR robot-object system into the control formulation.

6.5 Experiment: Transport of the Grasped Object Along the Path

To validate the proposed grasp configuration and MPC-based manipulation strategy, we conducted experimental trials involving the transport of four distinctly shaped objects along predefined paths. The experiments were designed to test both the robustness of the grasp configurations and the effectiveness of the MPC pure pursuit algorithm under varying geometric conditions. In this section, we also analyzed object grasping and transportation that occurred during experiments described in Chapter 7.

Experimental Setup

The experimental platform was constructed as a custom-designed testing environment housed within a $2.78 \times 1.4 \times 1.4$m box frame (Fig. 6.2 (left)). The frame is equipped with six OptiTrack cameras installed around its top perimeter to provide comprehensive motion capture coverage of the workspace. An RGB camera is centrally mounted on the top of the frame to provide additional visual monitoring of the experiments. To ensure reliable robot motion, the platform floor is covered with a non-slip silicone mat that prevents wheel slippage during manipulation tasks.

Figure 6.2: Left: Experimental platform.**Right**: Manipulandums of 4 different shapes: circle (yellow), ellipse (green), heart (red), bean (purple).

For the experimental trials, we fabricated four manipulandums with distinct geometric shapes: circle, ellipse, heart, and bean (Fig. 6.2 (right)). Each manipulandum is equipped with three support wheels to minimize friction with the platform floor, enabling smooth motion during manipulation. To enable precise tracking, three infrared (IR) markers are attached to the top surface of each manipulandum. The 2SR robot is equipped with nine IR markers: three on the head link unit, one on the tail link unit, and five distributed along the variable-stiffness bridge. This marker configuration allows us to accurately track not only the robot's position and orientation but also approximate the curvature of its segments during manipulation tasks.

Given a set of marker points $(x_i, y_i)_{i=1}^{n}$, we approximate the robot's shape using parametric cubic splines. The process can be formalized as follows:

1. First, we fit a parametric spline curve $\mathbf{r}(s) = (x(s), y(s))$, where $s \in [0, 1]$ is the curve parameter. This is achieved using B-splines with the following properties:

- Minimal smoothing (s=0)
- Cubic interpolation between points.

2. The arc length of the spline curve is computed as:

$$L = \int_0^1 |\mathbf{r}'(s)| ds \approx \sum_{i=1}^{N-1} \sqrt{(x(s_{i+1}) - x(s_i))^2 + (y(s_{i+1}) - y(s_i))^2} \tag{6.13}$$

where N is the number of discretization points (1000 in the implementation).

3. The curve's midpoint (x_m, y_m) is found by locating the point where the accumulated arc length equals $L/2$.

4. The heading angle θ at the midpoint is computed from the tangent vector:

$$\theta = \arctan(y'(s_m), x'(s_m)) \tag{6.14}$$

with continuity enforcement across the $\pm\pi$ boundary.

5. The curvature is computed separately for the first and second halves of the curve using the standard differential geometry formula:

$$\kappa(s) = \frac{x'(s)y''(s) - y'(s)x''(s)}{(x'(s)^2 + y'(s)^2)^{3/2}} \tag{6.15}$$

6. The mean curvatures for each half are then calculated:

$$\begin{aligned} \kappa_1 &= \frac{2}{N} \sum_{i=1}^{N/2} \kappa(s_i) \\ \kappa_2 &= \frac{2}{N} \sum_{i=N/2+1}^{N} \kappa(s_i). \end{aligned} \tag{6.16}$$

For each manipulandum, we conducted three experimental trials, each following a unique reference path $\mathbf{\Gamma}$. These paths were generated using cubic Bézier curves to ensure smooth transitions from the initial to the final configurations.

The path generation process can be formalized as follows. Given:

- *Initial pose*: $\mathbf{p}_{start} \in \mathbb{R}^2$
- *Target pose*: $\mathbf{p}_{end} \in \mathbb{R}^2$
- *Initial heading*: θ_{start}
- *Final approach angle*: θ_{end}.

The Bézier control points are defined as:

$$\begin{aligned} \mathbf{P}_0 &= \mathbf{p}_{start} \\ \mathbf{P}_1 &= \mathbf{p}_{start} + d_{exit}[\cos(\theta_{start}), \sin(\theta_{start})]^T \\ \mathbf{P}_2 &= \mathbf{p}_{end} - d_{entrance}[\cos(\theta_{start} + \beta) \;\; \sin(\theta_{start} + \beta)]^T \\ \mathbf{P}_3 &= \mathbf{p}_{end} \end{aligned} \tag{6.17}$$

where d_{exit} and $d_{entrance}$ are the exit and entrance distances that control the path curvature.

The reference path $\mathbf{\Gamma}$ is then generated using the cubic Bézier formula:

$$\mathbf{B}(t) = (1-t)^3\mathbf{P}_0 + 3(1-t)^2 t\mathbf{P}_1 + 3(1-t)t^2\mathbf{P}_2 + t^3\mathbf{P}_3, \quad t \in [0,1] \tag{6.18}$$

The path is discretized into 100 points for practical implementation, providing a dense representation while maintaining computational efficiency.

Task Execution

The transport experiment procedure began with manual positioning the 2SR robot in a pre-computed grasping configuration around each target object. This experiment was performed with all four manipulandums, with three trials per shape. Real-time state feedback was provided by the OptiTrack system, enabling the MPC-based pure pursuit controller to compute appropriate object and robot velocities. Computed velocities were then transmitted to the M&M controller for real-time robot motion execution.

Experiments presented in Chapter 7 assessed the robot's complete manipulation sequence: navigation through obstacles, object approach, grasping, and transportation. These experiments were conducted exclusively with the heart-shaped

object, with four trials per experiment. While Chapter 7 provides detailed analysis of the navigation strategies and motion planning performance, the present chapter focuses specifically on the grasping and transportation performance across all experimental trials. The crucial distinction between the pure transport experiments and the navigation-included experiments lies in their initial conditions. In the pure transport experiments, the grasping configuration was manually prepared in advance, with the robot directly beginning at the transport phase. In contrast, the navigation-included experiments evaluated the complete sequence, including autonomous approach and full-body grasping before proceeding to transport.

Analysis

Figures 6.3 and 6.6 illustrate time-lapsed sequences of transportation tasks conducted under two distinct experimental conditions: with manual pre-configured grasping and with automated full-body grasping, respectively. The orientation plots in Fig. 6.4(a) reveal distinctive manipulation characteristics across the different object geometries, highlighting how object morphology significantly influences manipulation stability and precision.

The *ellipse-shaped manipulandum* exhibited the most pronounced oscillatory behaviour during transport, characterized by periodic fluctuations in orientation tracking. This instability can be attributed to several factors:

- Its narrow profile and smaller footprint offered limited contact surface area
- The high curvature of its perimeter (exceeding the robot's maximum achievable curvature for variable-stiffness segments) prevented complete conformity of the robot's body
- The resulting loose grasp created opportunities for micro-slippage during direction changes
- The lower rotational inertia of this smaller object made it more susceptible to perturbations from uneven surface friction or minor control variations

These characteristics manifested as higher-frequency, lower-amplitude oscillations in the orientation plot, indicating continuous small adjustments by the controller attempting to maintain the desired trajectory.

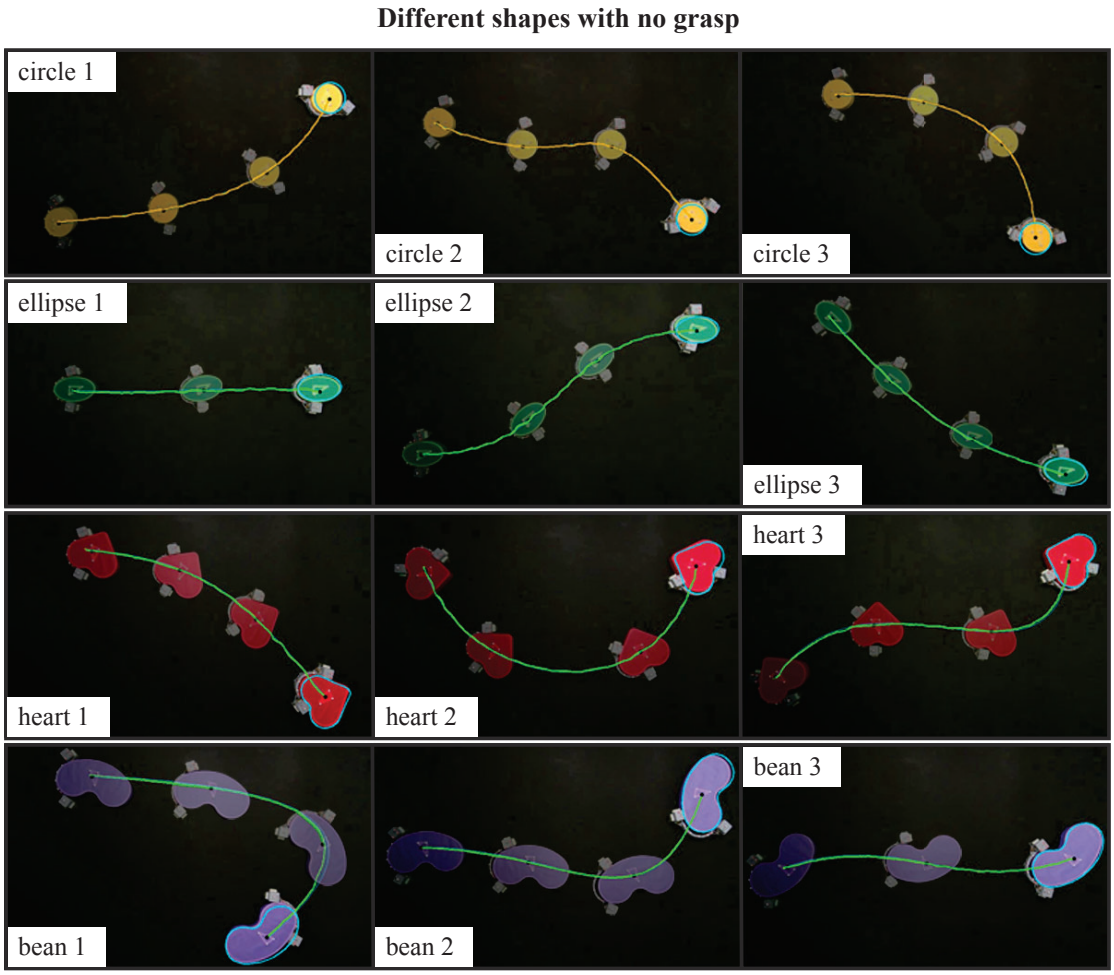

Figure 6.3: Time-lapsed sequences of transportation trials conducted with pre-configured grasping for four different object shapes. Each row represents a different manipulandum (circle, ellipse, heart, and bean), and columns show three separate trials for each object.

In stark contrast, the *bean-shaped object* demonstrated remarkably stable manipulation performance across all trials. This enhanced stability stems from several advantageous properties:

- Its larger size provided substantially more surface area for contact establishment
- Its extended length along one axis significantly enhanced rotational stability through increased moment of inertia
- The moderate curvature regions along its perimeter enabled better conformity with the robot's variable-stiffness segments

- The asymmetric shape created natural "keying" points for the robot's grasp

Particularly noteworthy was the performance in trial "Bean 1," where the robot successfully executed an exceptionally sharp turn—a maneuver not achievable with other objects. The quantitative analysis in Fig. 6.4(b) confirms the minimal slippage during this challenging manipulation. The plot reveals only minor deviations occurring precisely during the sharp turn where higher rotational forces were required to redirect the object's momentum.

This momentary slip manifests in the data as a slight orientation offset between the robot and object at the turn's completion. Notably, after this brief deviation, the orientation profiles quickly realign and maintain close correspondence for the remainder of the trajectory, indicating that the control system successfully re-established secure contact and stable manipulation without requiring explicit recovery actions. This self-stabilizing behaviour demonstrates the inherent robustness of the combined mechanical compliance and control approach.

Other objects exhibited intermediate performance characteristics, with performance quality generally correlating with:

1. The available surface area for contact establishment
2. The compatibility between object contour geometry and the robot's achievable morphological configurations
3. The object's moment of inertia, which affects rotational stability during turning maneuvers

Figure 6.4(c) shows the system responses during trial "Ellipse 3", where the plotted velocities represent control inputs. The object maintains a smooth heading velocity of $0.05\frac{m}{s}$ along straight paths, with adaptive velocity reduction proportional to path curvature. The robot's heading velocity closely tracks the object's target velocity, exhibiting corrective oscillations around the object's velocity profile.

The lateral velocity profiles demonstrate mirror symmetry with similar magnitudes but opposite signs, resulting from the configuration where the robot's $\hat{x}$-axis and object's $\hat{y}$-axis are approximately orthogonal ($\theta_{bo} \approx 90°$). The elliptical object's narrow profile facilitates precise lateral control, allowing it to closely follow the robot's lateral motions. However, this geometric advantage in lateral manip-

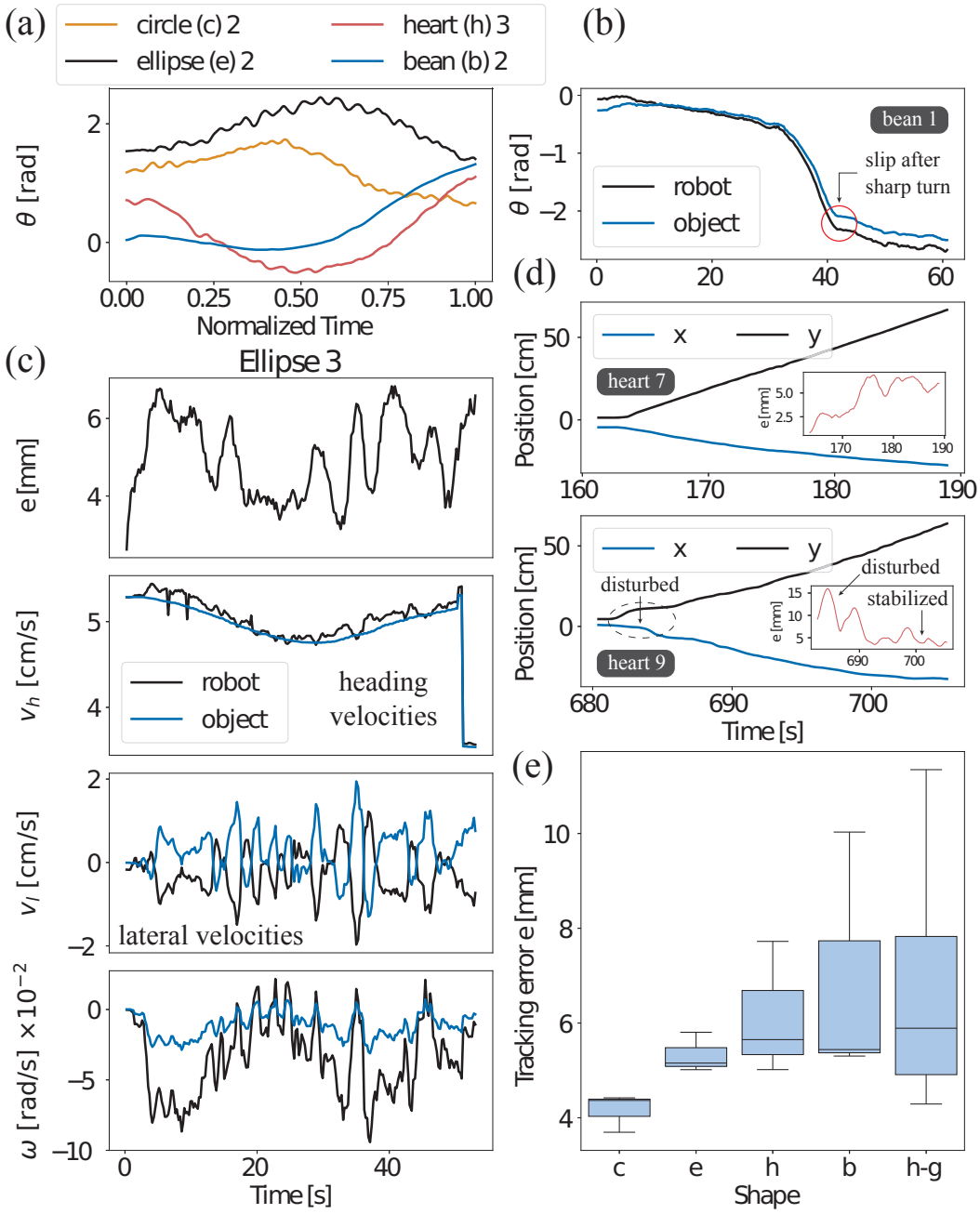

Figure 6.4: a) Comparison of orientation change over time across trials for different shapes (one representative trial per shape) during the experiment with pre-configured grasp. (b) Comparison of orientation change over time for robot and object during trial "Bean 1". (c) Tracking error evolution and system responses during trial "Ellipse 3" showing heading, lateral, and rotational velocities for both robot and object. (d) Comparison of position coordinates and tracking error evolution between trials "Heart 7" and "Heart 9". (e) Box plot summarizing tracking errors across different object shapes, where "h-g" denotes heart trials conducted with dynamic grasp.

ulation presents challenges during rotational movements. The rotational velocity profiles reveal significant corrective actions required from the robot to compensate for limited contact surface and maintain the desired object orientation. This behaviour contrasts with the bean-shaped object, which exhibits more stable forward pushing but requires greater effort for lateral adjustments.

Fig. 6.5 illustrates the time-lapsed sequences of the 2SR robot executing the final two steps of the three-phase grasping method: transitioning from pre-grasp to intermediate grasp configuration, followed by progression to final grasp contact. The quantitative plots from trial "Heart 4" provide a comprehensive view of the robot's states and control inputs throughout this process. Initially positioned in a default rigid, straight configuration at the pre-grasp pose (2-4 cm from the target object), the system begins its transformation by initiating thermal activation of both variable-stiffness segments. This phase transition from rigid to flexible states is evidenced by the increasing temperature curves and the subsequent reduction in segment stiffness.

Once sufficient flexibility is achieved, the robot employs specialized "flexible" velocity controls to deliberately adjust the curvature of both segments. This deformation process is not passive but actively controlled by locomotion units that induce specific bending patterns in the compliant structure. As the segments progressively conform to the desired morphological configuration, we observe coordinated changes in both curvature values (κ_1 and κ_2) that reflect the robot's adaptation to match the target object's contour geometry.

Upon completing the desired deformation profile, the robot initiates the solidification phase, gradually cooling the low melting point alloy within bridge modular units to lock in the acquired shape. After that, the controller makes subtle adjustments to the robot's overall pose, optimizing alignment with the object before establishing direct contact. It was observed that during this final phase minor fluctuations in bridge curvatures persist despite the intended rigidity. These fluctuations stem from the structural design's inherent mechanical compliance that is caused by small gaps between the modular units.

The phase transitions between different stiffness states are characterized by distinct waiting periods, during which locomotion controls remain inactive while thermal management continues. These deliberate pauses appear as plateaus in the

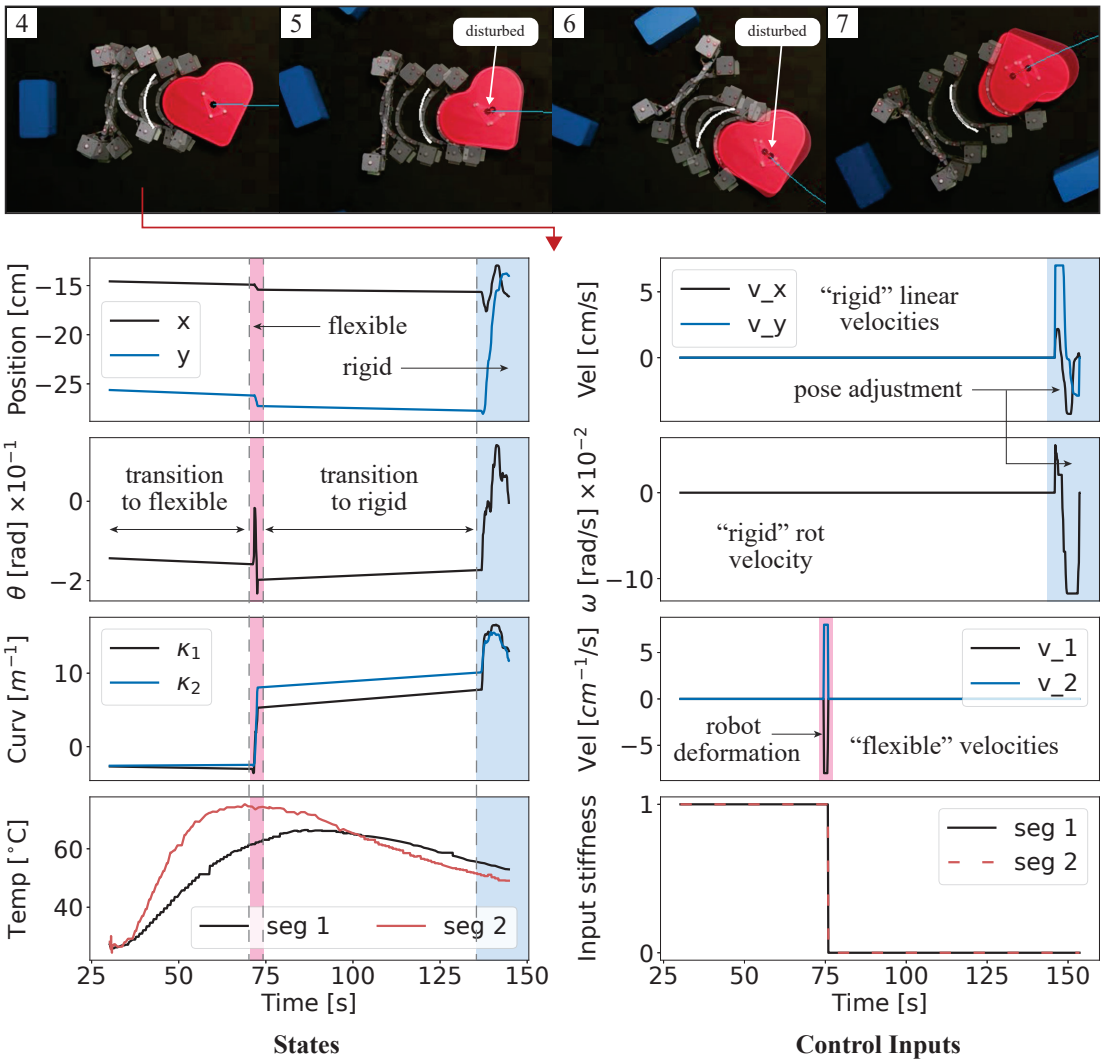

Figure 6.5: Top: Time-lapsed sequences of the 2SR robot executing full-body grasping on a heart-shaped object during the fixed-morphology experiment. **Bottom**: System responses during trial "Heart 4" showing robot states (pose, curvatures and temperature feedback) and control inputs (target velocities and stiffness transition commands) throughout the grasping process.

state and control input plots, allowing sufficient time for temperature changes to propagate through the LMPA material. A notable asymmetry is observed between the two segments' thermal responses, with the second segment consistently displaying faster temperature changes. This differential behaviour may be attributed to geometric factors (smaller accumulative alloy volume in the second segment), manufacturing variations in the embedded heating elements, or differences in heat dissipation conditions.

The quality of the final contact configuration profoundly influences subsequent

manipulation performance. Our experiments reveal that major imperfections during grasp establishment can propagate into significant challenges during transport. In several instances, the robot's locomotion units inadvertently disturbed the object during the approach and contact phases, creating initial misalignments with the intended reference path. These disturbances typically manifest when the robot fails to achieve perfect orientation or overshoots its target location at the grasp configuration.

Figure 6.6 illustrates the consequences of such grasp imperfections, showing oscillatory motion patterns that emerge during the initial transport phase. These oscillations represent the control system's continuous effort to reconcile the initial misalignment with the desired trajectory. The comparative analysis in Figure 6.4(d) provides quantitative evidence of this phenomenon, contrasting the position coordinates and tracking error evolution between trial "Heart 7" (exemplifying near-perfect grasp execution) and trial "Heart 9" (showing object disturbance during grasp).

In the disturbed case, the initial transport phase exhibits pronounced deflections and oscillatory behaviour as the controller works to accommodate the misalignment. However, despite these challenging initial conditions, the robot demonstrates satisfactory recovery capabilities. Over time, the control system successfully achieves stabilization through a combination of active corrections and the inherent mechanical compliance of the robot-object interface. This self-stabilizing behaviour highlights the robustness of our approach, which gradually attenuates initial disturbances without requiring explicit recovery actions or regrasping procedures.

The comprehensive error analysis presented in Figure 6.4(e) reveals distinct performance patterns across different object geometries. The circular manipulandum consistently demonstrates the lowest median tracking error, attributable to its uniform curvature that creates an optimal contact profile with the robot's flexible segments. This geometric compatibility allows for more uniform pressure distribution along the contact interface, reducing the likelihood of localized slip.

The bean-shaped object presents an interesting case with a lower median error than the elliptical manipulandum but substantially greater variance in its error distribution. This increased variance is primarily attributable to the challenging

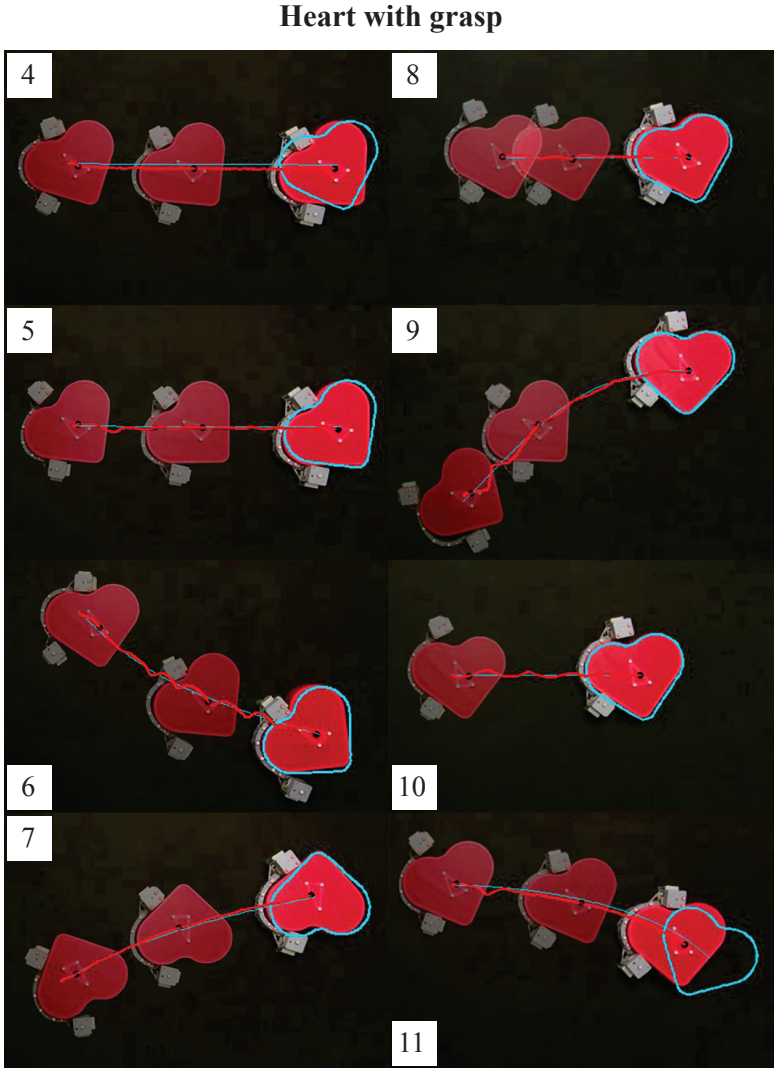

Figure 6.6: Time-lapsed sequences of transportation trials with dynamic grasping performed on a heart-shaped object (left column - fixed-morphology experiment, right column - adaptive-morphology experiment).

sharp turn executed in trial "Bean 1," where the robot momentarily exceeded the friction limits at the contact interface. Despite this transient slip event, the overall manipulation remained stable due to the object's favorable moment of inertia and extended contact area.

As anticipated, the navigation-inclusive experiments accumulate larger cumulative errors compared to the pure transport trials. This increased error stems from the cascading effects of grasp-related disturbances that create initial condition deviations. Nevertheless, a key finding is that these larger initial errors do

not prevent successful task completion. The 2SR robot successfully executed all assigned manipulation tasks across all experimental conditions, demonstrating the fundamental robustness of our variable-stiffness manipulation approach even under non-ideal grasping conditions.

This resilience to initial condition variations represents a significant advantage for practical robotic manipulation applications, where perfect grasping cannot always be guaranteed. The system's ability to gradually stabilize and complete transport tasks despite initial misalignments suggests that our combined morphological adaptation and control approach offers a promising direction for robust manipulation in unstructured environments.

6.6 Summary

This chapter explored the unique capabilities of the 2SR robot for full-body grasping and manipulation of objects with arbitrary shapes. The robot's variable stiffness structure enables it to conform to diverse geometries in ways impossible for conventional mobile robots, creating an adaptive interface for secure manipulation.

We began by formulating two key challenges: implementing effective full-body grasping configurations and developing optimal transport strategies for manipulandum control. We established a contact model that maps robot and object twists, enabling coordinated manipulation through a direct kinematic relationship between robot and object velocities. This model operates under assumptions including planar operation, continuous environmental constraint, sufficient friction, no-slip conditions, effective force transmission, and quasi-static conditions.

A three-phase strategy for full-body grasping with the 2SR robot was introduced. It includes the following steps: approach, grasp without contact, and final contact. The robot's final contact configuration is derived from the object geometry by ensuring appropriate distance, maximizing shape conformity, and maintaining proper orientation for subsequent object transport. To prevent object disturbance during approach, the strategy incorporates both an intermediate grasp configuration and a pre-grasp pose by progressively offsetting from the final contact position. This graduated approach allows the robot to achieve stable, conforming grasps of objects with arbitrary geometries while minimizing the risk of unintended object

movement during the grasping process.

For object path tracking, we developed an MPC-based pure pursuit algorithm that generates reference trajectories over a prediction horizon, linearizes object dynamics around this reference, and solves a quadratic optimization problem to determine optimal control inputs. This approach balances tracking accuracy against smooth, feasible motion while anticipating path curvature.

Experimental validation assessed the system's performance with four differently shaped objects (circle, ellipse, heart, and bean) under two experimental conditions: pre-configured grasping and autonomous full-body grasping. Key findings include:

1. *Object geometry significantly influences manipulation stability:*
    - Circular objects demonstrated the most consistent performance due to uniform curvature
    - Bean-shaped objects provided excellent rotational stability through extended contact area
    - Elliptical objects presented challenges due to limited contact surface and high curvature
2. *The three-phase grasping method effectively adapts to object shapes:*
    - Thermal transitions enable strategic alternation between flexibility for morphological adaptation and rigidity for force transmission
    - Controlled deformation allows deliberate shaping of the robot's body to match object contours
    - The inherent compliance of the variable-stiffness structure provides passive adaptation to minor object variations
3. *Grasp quality significantly impacts subsequent transportation performance:*
    - Imperfect grasping can cause oscillations during initial transport
    - The system demonstrates self-stabilizing capabilities that gradually attenuate initial misalignments

- Despite larger errors in trials with autonomous grasping, the system successfully completed all manipulation tasks

The system demonstrated remarkable robustness across varied experimental conditions, successfully transporting objects even under non-ideal grasping configurations. This adaptability represents a significant advantage for practical applications in unstructured environments.

The integration of adaptive morphology through variable stiffness with predictive control strategies creates a manipulation system that effectively leverages both mechanical intelligence and algorithmic optimization. This synergistic approach enables the 2SR robot to achieve adaptive, secure manipulation of diverse object geometries while maintaining precise trajectory control during transport tasks.

Chapter 7

Traversing Cluttered Environments

7.1 Path Planning with Fixed Morphology

Path planning in cluttered environments presents unique challenges when a mobile robot has an *elongated shape*. Unlike point-mass robots where only position matters, the robot's orientation becomes crucial for successful navigation. This section presents a planning approach for a rectangular-shaped mobile robot tasked with reaching and grasping objects in environments with obstacles. The proposed method addresses two key challenges:

Problem 7.1.1. *First, while traditional sampling-based planners like RRT* excel at finding collision-free paths for point robots, they become computationally expensive when directly applied to both position and orientation planning. Random sampling in the full configuration space often leads to collisions, significantly increasing planning time or causing failures. Second, rapid orientation changes, even if theoretically valid, may be difficult to execute precisely during physical experiments.*

To overcome these limitations, we decompose the planning problem into position search and orientation control. The former utilizes *rapidly exploring random trees (RRT*)* to efficiently explore the workspace and find optimal paths between start and goal positions. The orientation is then generated using an *artificial potential field (APF)* that considers multiple factors: obstacle proximity and alignment, goal orientation, and path smoothness. This decomposition significantly reduces the computational burden while ensuring smooth and practical trajectories.

7.1.1 Position Search with RRT*

The schematic figure 7.1 demonstrates a potential scenario when a robot is tasked to approach, grasp, and transport an object along a specified path. The object's initial location and geometry are known, as well as the desired transportation trajectory. Before the actual manipulation can begin, the robot must safely navigate through the workspace to reach a suitable pre-grasp position near the object. This approaching motion must be carefully planned to avoid collisions with obstacles while ensuring that the final configuration allows for a secure grasp of the object.

The pre-grasp location $\mathbf{x}'_r$ is determined according to (6.4). It is going to serve as a target destination for the path planner. For environments with minimal clutter, the robot can maintain its default rigid configuration throughout the navigation phase. This eliminates the need for complex shape changes during transit, effectively reducing the problem to conventional rigid body motion planning.

Since no morphological variations are required, bridge curvatures in configuration $\mathbf{x}'_r$ are ignored. By preserving a constant shape profile with straight bridge segments, we can simplify the robot's collision boundary as a rectangular shape with length l and width w, where $l \gg w$. VS segments transition to flexible upon reaching the object and deform to match $\mathbf{q}_g$ (offset ensures adequate space for reshaping). Finally, the robot establishes contact with the object at $\mathbf{q}_f$.

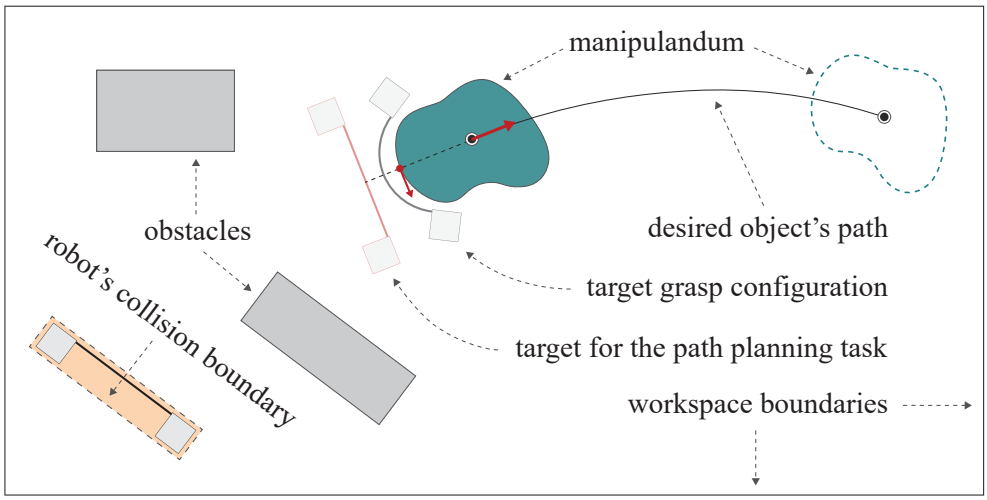

Figure 7.1: Schematic representation of the manipulation planning scenario: workspace layout showing the robot, obstacles, object with its desired transportation path, computed grasp configuration, and the corresponding path planning target.

Definition 7.1.1. *During path traversal, the robot maintains a default rigid configuration with straight segments, allowing its collision boundary to be approximated as a rectangle. This simplification permits us to ignore curvature constraints and define the path planning problem as finding a sequence of poses* $\mathbf{\Gamma}_r = [\mathbf{x}_{r,0}, ..., \mathbf{x}_{r,k}, ..., \mathbf{x}'_r]^\intercal$ *where* $\mathbf{x}_{r,k} = [\mathbf{p}_{r,k}, \theta_{r,k}]^\intercal \in \mathcal{C} \subset \mathbb{R}^2 \times \mathbb{S}^1$, $k \in \mathbb{N}$. *The configuration space* $\mathcal{C}$ *is constrained by workspace boundaries and obstacles, requiring collision-free paths from the robot's initial location* $\mathbf{x}_{r,0} = [x_b, y_b, \theta_b]^\intercal$ *to target* $\mathbf{x}'_r$.

Our solution for this problem combines the **RRT* (Rapidly-exploring Random Tree Star)** algorithm for position sampling with an **Artificial Potential Field (APF)** approach for orientation guidance. This hybrid approach leverages the strengths of both methods: RRT* excels at efficient exploration of the position space and finding collision-free paths in complex environments, while APF provides a computationally efficient way to determine suitable orientations based on workspace geometry and task constraints.

The RRT* algorithm is particularly well-suited for position planning due to its probabilistically complete nature and asymptotic optimality guarantees. It effectively handles the non-convex constraints imposed by workspace obstacles and the robot's rectangular geometry. However, directly applying RRT* to the full configuration space, including orientation, would significantly increase the computational complexity and potentially lead to inefficient exploration due to the periodic nature of angular coordinates. Instead, the orientation at each sampled position is computed using an APF-based method that considers the local workspace geometry and target configuration.

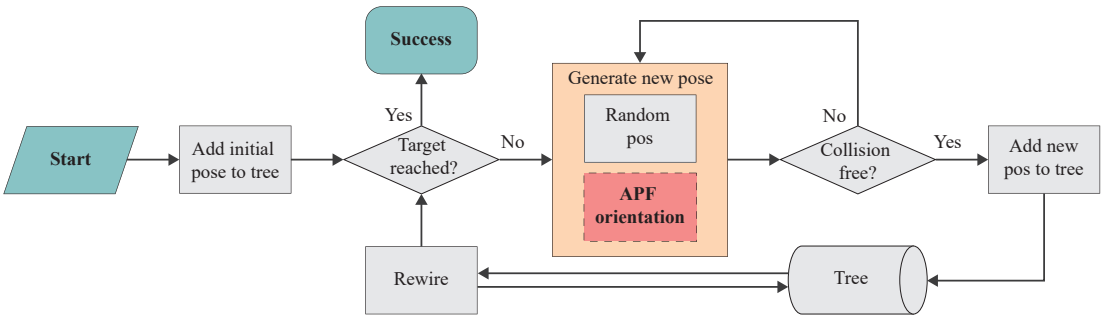

Figure 7.2: Flow chart illustrating the main steps of the hybrid path planning algorithm, combining RRT* for position sampling with APF-based orientation guidance.

The flow chart in Fig. 7.2 illustrates the working principle of the proposed approach. The RRT* algorithm constructs a tree $\mathcal{T} = (\mathbf{X}, \mathbf{E})$ where vertices $\mathbf{X}$ represent robot configurations and edges $\mathbf{E}$ represent feasible transitions between configurations. Each node maintains position coordinates, orientation angle, parent reference, and cost-to-come value. The tree grows incrementally through the following steps:

1. *Initialization*: The tree is rooted at the initial configuration $\mathbf{x}_{r,0}$, storing its position, orientation, and a cost-to-come value of zero.

2. *New Pose Generation*:

   - *Position Sampling*: A new position $\mathbf{p}_{r,new}$ is randomly sampled within the workspace boundaries. The sampling is biased towards the target position with probability p_{goal} to improve convergence.

   - ***Orientation Assignment***: The orientation $\theta_{r,new}$ at the sampled position is computed using the APF method, which is detailed in the subsequent section. This approach ensures the robot's orientation aligns with both local obstacle constraints and the global task objective.

3. *Collision Checking*: The local path connecting the closest node from $\mathcal{T}$ to the new configuration $\mathbf{x}_{r,new} = [\mathbf{p}_{r,new}, \theta_{r,new}]^\intercal$ is checked for collisions. If a collision is detected, the sample is discarded, and the algorithm returns to *Step 2*.

4. *Node Addition*: If the path is collision-free, $\mathbf{x}_{r,new}$ is added to the tree. The algorithm then searches within a neighborhood radius r for potential parent nodes that could provide a lower cost-to-come value.

5. *Tree Rewiring*: The algorithm examines if $\mathbf{x}_{r,new}$ can provide better paths with lower cost to existing nearby nodes. If such opportunities are found, the tree is rewired to maintain optimality.

6. *Termination Check*: The algorithm checks if target $\mathbf{x}_r$ is reachable from the new node with a collision-free path Γ_r. If successful, the algorithm terminates; otherwise, it continues from *Step 2*.

7.1.2 Orientation Control via APF

The orientation $\theta_{r,new}$ at each sampled position during RRT* is determined using an Artificial Potential Field (APF) approach that balances three key influences: obstacle repulsion, goal attraction, and path smoothness.

Definition 7.1.2. *Each obstacle in the workspace is defined as a polygon with a set of vertices* $\mathcal{O}_i = \{\mathbf{p}_{i,1}, \mathbf{p}_{i,2}, ..., \mathbf{p}_{i,n_i}\}$*, where* $\mathbf{p}_{i,j} \in \mathbb{R}^2$ *denotes the* j*-th vertex of the* i*-th obstacle, and* n_i *is the number of vertices in obstacle* i*, see Fig. 7.3(left). The complete workspace obstacle set is denoted as* $\mathcal{O} = \{\mathcal{O}_1, \mathcal{O}_2, ..., \mathcal{O}_m\}$*, where* m *is the total number of obstacles.*

The total potential function U at each RRT* sampling step can be calculated as a weighted sum:

$$U(\mathbf{p}_{r,k}, \mathcal{O}) = \lambda_o U_{\text{obs}}(\mathbf{p}_{r,k}, \mathcal{O}) + \lambda_g U_{\text{goal}}(\mathbf{p}_{r,k}) + \lambda_p U_{\text{par}}, \tag{7.1}$$

where coefficients λ_o, λ_g, and λ_p are weights for obstacle, goal, and parent node potentials.

The obstacle repulsion potential U_{obs} combines distance-based repulsion with an orientation alignment, encouraging configurations where the robot's longitudinal axis parallels nearby obstacles. For each obstacle $\mathcal{O}_i \in \mathcal{O}$, the potential is only considered when the robot is within a threshold distance $d_{\text{thresh}} = 2l$, where l is the robot's length. Thus, the obstacle potential can be found as:

$$U_{\text{obs}}(\mathbf{p}_{r,k}, \mathcal{O}) = \sum_{\mathcal{O}_i \in \mathcal{O}} \frac{||\alpha(\mathbf{p}_{r,k}, \mathcal{O}_i)| - \frac{\pi}{2}|}{d(\mathbf{p}_{r,k}, \mathcal{O}_i)}. \tag{7.2}$$

Here, $d(\mathbf{p}_{r,k}, \mathcal{O}_i)$ denotes the minimum distance between robot and obstacle $\mathcal{O}_i$ and $\alpha(\mathbf{p}_{r,k}, \mathcal{O}_i)$ represents the angle between the robot's longitudinal axis (defined by $\theta_{r,k}$) and the vector from the robot's centre to the i-th obstacle's centroid. This formulation creates a potential field that simultaneously pushes the robot away from obstacles while encouraging parallel alignment with them when in close proximity.

The goal attraction potential U_{goal} is designed to align the robot's orientation with the goal configuration while considering the distance to the goal. This poten-

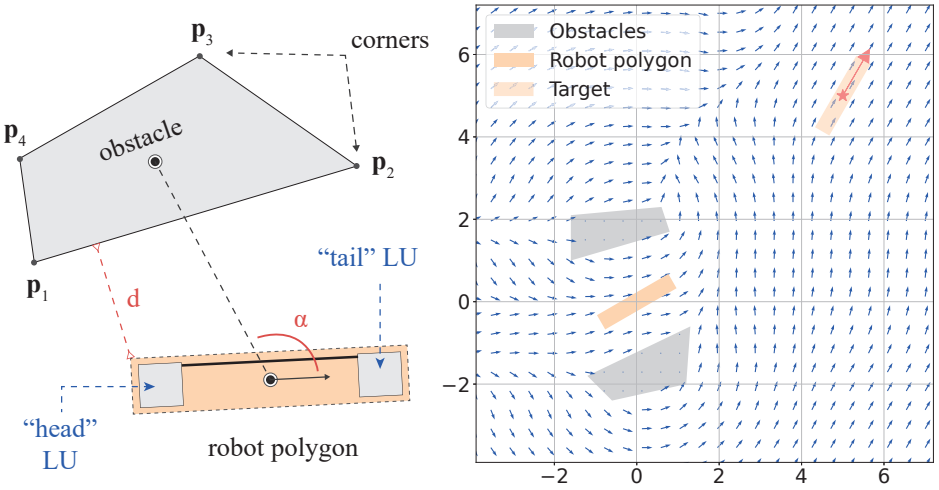

Figure 7.3: Left: Geometrical features of the obstacle and robot polygons used when calculating the obstacle repulsion potential. **Right:** Artificial potential field visualization with orientation optimization. Blue arrows show the optimal orientation at each point. The robot's initial position (solid yellow) and target position (transparent yellow) are shown, along with obstacles (grey).

tial is calculated as:

$$U_{\text{goal}}(\mathbf{p}_{r,k}) = \frac{|\theta_{r,k} - \theta'_r|}{d(\mathbf{p}_{r,k}, \mathbf{p}'_r)}, \tag{7.3}$$

where θ'_r is the desired orientation at the goal configuration, and $d(\mathbf{p}_{r,k}, \mathbf{p}'_r)$ is the Euclidean distance between the robot's current position and the goal position. The denominator term makes the goal orientation influence stronger as the robot approaches the target.

The parent node influence potential U_{par} promotes path smoothness by penalizing sharp changes in orientation between consecutive configurations:

$$U_{\text{par}} = |\theta_{r,k} - \theta_{\text{par}}|, \tag{7.4}$$

where θ_{par} is the parent node's orientation in the RRT* tree.

Given the defined potential terms, the optimal orientation $\theta_{r,k}$ for a sampled pose is determined by solving the following optimization problem:

$$\begin{aligned} &\underset{\theta_{r,k}}{\text{minimize}} \quad U(\mathbf{p}_{r,k}, \mathcal{O}) \\ &\text{subject to} \quad d(\mathbf{p}_{r,k}, \mathcal{O}) > 0 \quad \text{(collision-free configuration)}. \end{aligned} \tag{7.5}$$

The complete orientation control algorithm is summarized in Algorithm 4:

Algorithm 4: APF-Based Orientation Optimization

Input: robot position $\mathbf{p}_{r,k}$, obstacle set $\mathcal{O}$, parent orientation θ_{par}, goal position $\mathbf{p}'_r$, goal orientation θ'_r, weights λ_o, λ_g, λ_p

Result: optimal orientation $\theta_{r,k}$

Initialize: $\theta_{\text{best}} \leftarrow \theta_{\text{par}}$, $U_{\min} \leftarrow \infty$;
Compute distance threshold: $d_{\text{thresh}} \leftarrow 2l$ (where l is robot length);
for $\theta_{test} \in [-\pi, \pi]$ *with step* $\Delta\theta$ **do**
    if $d(\boldsymbol{q}_{r,k}, \mathcal{O}) \leq 0$ **then**
        continue;
    $U_{\text{obs}} \leftarrow 0$;
    for *each obstacle* $\mathcal{O}_i \in \mathcal{O}$ **do**
        $d_i \leftarrow \mathtt{d}(\mathbf{p}_{r,k}, \mathcal{O}_i)$;
        if $d_i < d_{thresh}$ **then**
            $\alpha_i \leftarrow \alpha(\mathbf{p}_{r,k}, \mathcal{O}_i)$;
            $U_{\text{obs}} \leftarrow U_{\text{obs}} + \frac{||\alpha_i| - \frac{\pi}{2}|}{d_i}$;
    $d_{\text{goal}} \leftarrow \mathtt{d}(\mathbf{p}_{r,k}, \mathbf{p}'_r)$;
    $U_{\text{goal}} \leftarrow \frac{|\theta_{\text{test}} - \theta'_r|}{d_{\text{goal}}}$;
    $U_{\text{par}} \leftarrow |\theta_{\text{test}} - \theta_{\text{par}}|$;
    $U_{\text{total}} \leftarrow \lambda_o U_{\text{obs}} + \lambda_g U_{\text{goal}} + \lambda_p U_{\text{par}}$;
    if $U_{total} < U_{min}$ **then**
        $U_{\min} \leftarrow U_{\text{total}}$;
        $\theta_{\text{best}} \leftarrow \theta_{\text{test}}$;
$\theta_{r,k} \leftarrow \theta_{\text{best}}$;
return $\theta_{r,k}$

Introduced method provides a stable path planning approach for rectangular-shaped mobile robots in cluttered environments. The algorithm separates position and orientation planning, using RRT* for finding optimal collision-free paths and APF for determining suitable orientations. The orientation control considers obstacle proximity, goal configuration, and path smoothness, ensuring practical trajectories that account for the robot's elongated shape, example instance of APF execution is illustrated in Fig. 7.3(right). This decomposition significantly reduces computational complexity while maintaining effective navigation capabilities.

7.1.3 Experiment and Performance Analysis

The effectiveness of the proposed **hybrid RRT*-APF path planning** algorithm was validated through a comprehensive manipulation experiment that combines navigation, full-body grasping, and transportation tasks with a heart-shaped manipulandum. The experiment was designed to evaluate the algorithm's performance in a typical pick-and-transport scenario, where the robot must traverse a cluttered environment, achieve an optimal pre-grasp configuration, grasp the object and successfully manipulate an object along a predetermined path.

The experimental setup uses the platform introduced in Chapter 6, equipped with an OptiTrack motion capture system and an overhead RGB camera for environmental perception. The workspace contains multiple identical obstacles (3D-printed blue rectangular blocks with rounded corners, measuring $16 \times 8 \times 6$ cm) and a heart-shaped target object. This setup creates a structured yet challenging environment that requires the robot to:

1. Navigate safely between obstacles while maintaining appropriate configurations for collision avoidance
2. Achieve precise positioning at the pre-grasp location while considering the object's geometry
3. Execute a stable enveloping grasp that minimizes object displacement and ensures reliable manipulation
4. Transport the object smoothly along the predetermined path while maintaining grasp stability

System Initialization and Environment Mapping

Prior to executing the experiment, several preparatory steps were completed to establish a comprehensive understanding of the workspace. The experimental setup leverages the OptiTrack motion capture system, which provides continuous and precise tracking of both the robot's configuration and the object's pose throughout the entire experimental procedure. With the given object's contour, we generate a desired manipulation path using a Bézier curve, carefully maintaining a safe distance from the obstacles positioned behind the path's direction. This path generation process follows the methodology previously detailed in Chapter 6. Based

on this established path, we then compute the necessary grasp and pre-grasp configurations using Equations (6.4).

The environmental perception is achieved through an overhead RGB camera system. The obstacle detection pipeline is implemented using Python OpenCV, which begins with identifying obstacle contours in the camera frame. These contours are then approximated to four-corner polygons for simplified representation while maintaining accurate obstacle boundaries.

Remark 16. *A heart-shaped manipulandum is also treated as an obstacle during navigation, but with its contour represented by a higher-resolution polygon approximation to capture its more complex curvature. For grasping operations, however, we employ a more precise parametrized contour representation defined as* $\bar{\mathbf{c}}_o = (\mathbf{c}_o(\varsigma))_{\varsigma \in 0...1}$, *where* ς *traces the normalized arc length along the boundary. This detailed representation is processed using elliptical Fourier descriptors, enabling accurate computation of local curvatures and tangent vectors essential for optimizing the robot's conformable grasp configuration.*

Obstacles' coordinates are then transformed from the camera frame to the global coordinate system (after the calibration procedure). As a final step, each polygon is uniformly expanded by 2 cm to create safety buffer zones for conservative collision avoidance. With all elements in place - tracked poses, desired path, grasp configurations, and processed obstacle information - the workspace is fully characterized and ready for the execution of the RRT*-APF algorithm.

The complete initialization procedure is summarized in Table 7.1.

	Step Description	**Input**	**Output**
1	Initialize robot and object	Shape id	$\mathbf{x}_{r,0}$, $(\mathbf{x}_o, \bar{\mathbf{c}}_o)$
2	Generate manipulation path	$\mathbf{x}_o$	Γ_o
3	Calculate grasp configurations	$\mathbf{x}_o$, Γ_o	$\mathbf{q}_g$, $\mathbf{x}'_r$
4	Identify obstacles	RGB camera frame	$\mathcal{O}$

Table 7.1: Summary of system initialization and environment mapping steps.

Implementation of the Hybrid RRT*-APF Algorithm

The experimental validation consisted of four distinct scenarios, each featuring 2-3 obstacles with varying configurations of robot initial pose, manipulandum's position, and obstacle placement. Each scenario presented unique navigation challenges requiring adaptive path planning and precise orientation control.

The top panel of Fig. 7.4 provides a visual representation of the algorithm's operation. The exploration process is depicted through the network of white nodes and connecting edges, with directional arrows indicating the locally optimal orientation determined by the APF method at each sampled configuration. This visualization demonstrates how the potential field approach influences the robot's orientation throughout the search space, adapting to both obstacle proximity and goal alignment requirements. The final path $\mathbf{\Gamma}_r$, highlighted in green, illustrates the optimal route from the robot's initial pose to the designated pre-grasp configuration near the heart-shaped manipulandum.

The planner's efficiency is evident in its rapid convergence typically requiring only four to five exploration steps to identify a feasible path. This sparse path representation is subsequently enriched through linear interpolation, generating additional waypoints that ensure smoother transitions between configurations. The interpolation process maintains the core trajectory while mitigating abrupt directional changes that could compromise control stability during physical execution.

The quantitative performance metrics in the lower panels of Fig. 7.4 reveal important characteristics of the planning method. The orientation tracking plot demonstrates how the robot adjusts its heading early in the trajectory, making major orientation corrections during the first 40-50% of the path. This front loaded adjustment strategy allows the robot to establish proper alignment well before approaching the manipulandum, transitioning smoothly toward the precise pre-grasp orientation required for successful object interaction.

The clearance metrics provide insight into the algorithm's obstacle avoidance capabilities. It depends on distance and robot's orientation, being computed as the minimum distance between the robot's geometry and all surrounding obstacles.

For each robot's pose $\mathbf{x}_{r,k}$ in the path, the clearance $c(\mathbf{x}_{r,k})$ is calculated as:

$$c(\mathbf{x}_{r,k}) = \min_{\mathcal{O}_i \in \mathcal{O}} \min_{\mathbf{p} \in \mathcal{O}_i, \mathbf{q} \in \mathcal{R}(\mathbf{x}_{r,k})} ||\mathbf{p} - \mathbf{q}||_2, \tag{7.6}$$

where $\mathcal{R}(\mathbf{x}_{r,k})$ represents the set of points defining the robot's geometric boundary.

Maximum clearance naturally occurs at the initial configuration, typically positioned away from obstacles. As the robot navigates through the constrained workspace, clearance values fluctuate based on the proximity to different obstacles. Trial "Heart 4" exhibited the most challenging navigation sequence, recording the minimum clearance (approximately 0.2 m) when passing between closely spaced obstacles. This minimum occurs at an interpolated point between two RRT* nodes, highlighting a limitation of the discrete sampling approach.

Remark 17. *This observation reveals a crucial trade-off in the planning method: interpolated points inherit orientations without explicit APF optimization. Had a search node been placed at this precise location, the APF method would have calculated an orientation parallel to the nearby obstacle, potentially increasing clearance by aligning the robot's longitudinal axis with the obstacle boundary. We could address this limitation by reducing the search step size, generating more densely distributed nodes with individually optimized orientations. However, this approach would significantly increase computational overhead — a critical consideration for real-time applications.*

Our implementation strikes a pragmatic balance between optimization quality and computational efficiency. The safety margins incorporated into the obstacle definitions (expanded polygons accounting for robot dimensions) ensure that even interpolated configurations maintain sufficient clearance for collision-free navigation. This design choice prioritizes planning speed while preserving the fundamental safety constraints essential for reliable physical execution.

The consistent successful execution across all four experimental scenarios demonstrates the practical robustness of our approach. Despite the inherent limitations of discrete sampling and interpolation, the planning framework reliably generates executable trajectories that navigate complex environments while maintaining appropriate clearance and arriving at precisely oriented pre-grasp configurations ready for the subsequent manipulation phase.

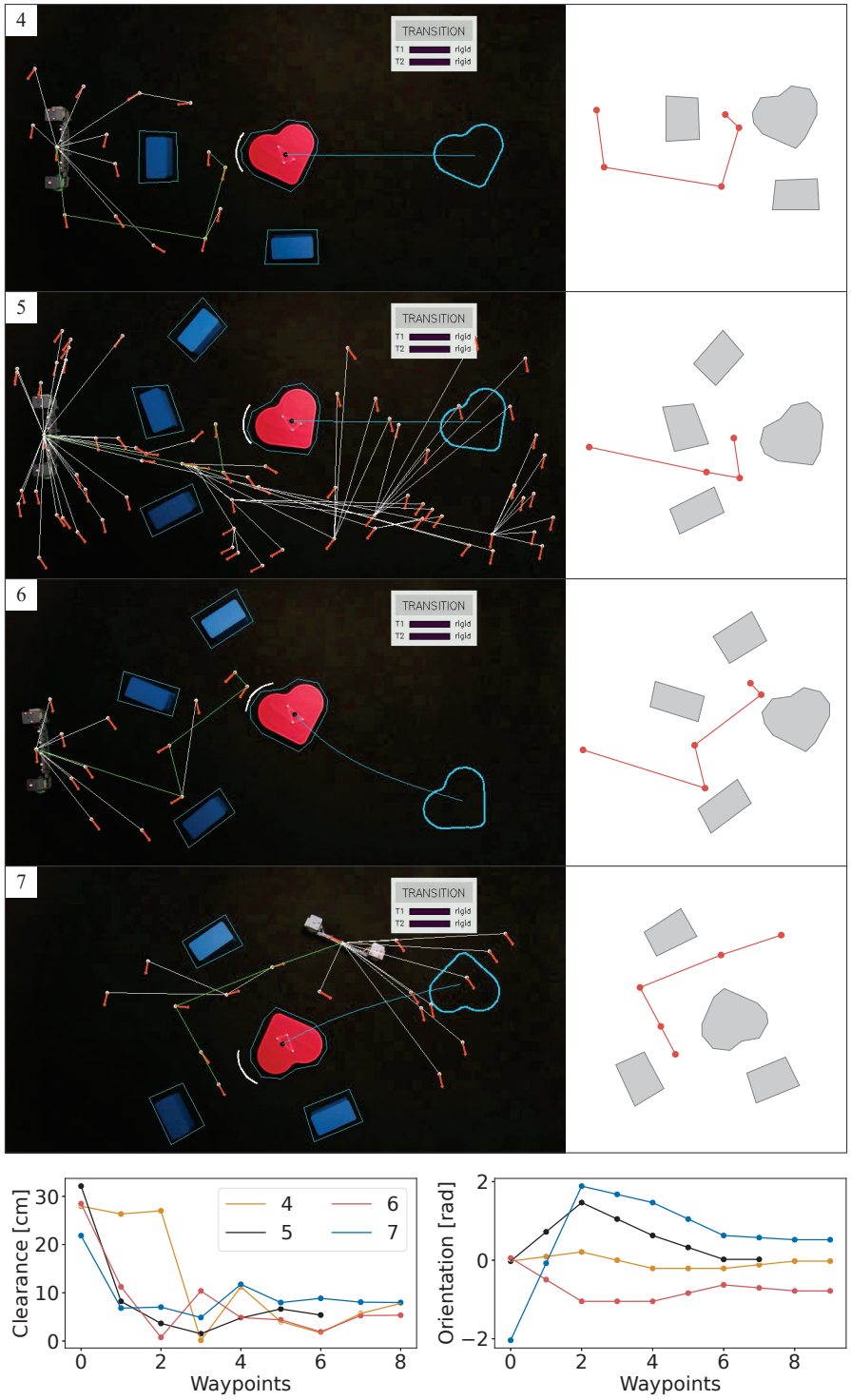

Figure 7.4: Path planning using the RRT*-APF method for navigating the 2SR robot through a cluttered environment to reach the target object. **Bottom**: Evolution of obstacle clearance and robot's orientation along the path waypoints.

Task Execution and Performance Analysis

Fig. 7.5 shows the physical implementation of the planned navigation strategy. The M&M controller executes the derived path $\mathbf{\Gamma}_r$ by sequentially processing each waypoint, generating appropriate control signals that produce smooth acceleration and deceleration profiles. As illustrated in the velocity control input plots, the controller implements brief stabilization periods at critical waypoints to ensure precise positioning before initiating subsequent trajectory segments. This approach mitigates accumulated positional errors and enhances system stability throughout the execution process.

The evolution of the robot's states and clearance metrics over time exhibits strong correlation with the planned profiles depicted in Fig. 7.4, validating the feasibility and accuracy of our planning framework. Minor discrepancies between planned and executed trajectories manifest primarily as transient positional overshoots at target waypoints. These deviations stem from the 2SR robot's elongated morphology, which introduces asymmetric inertial characteristics and nonholonomic constraints that complicate precise orientation control. Unlike robots with symmetric geometries (e.g., differential drive platforms), the 2SR's extended body creates momentum effects during rotational maneuvers that require additional settling time — a characteristic accounted for in our controller's design through adaptive deceleration profiles.

The box plot analysis in Fig. 7.5 provides quantitative insights into the mechanical performance of the variable stiffness segments during rigid states. By measuring curvature variations — a key indicator of structural integrity — we evaluated the consistency of shape maintenance throughout the navigation process. These variations arise from the inherent flexibility of the bridge design that is mostly caused by its modular structure.

The first VS segment demonstrates superior shape consistency, characterized by a near-zero median curvature and a relatively narrow distribution ranging between 2 and 5 m^{-1}. In contrast, the second segment exhibits both higher median values and wider distribution spread, indicating reduced stiffness and greater susceptibility to deformation under dynamic loading conditions. This performance differential, when considered alongside the faster thermal response and more rapid phase transitions observed in Fig. 6.5, suggests a material composition variance

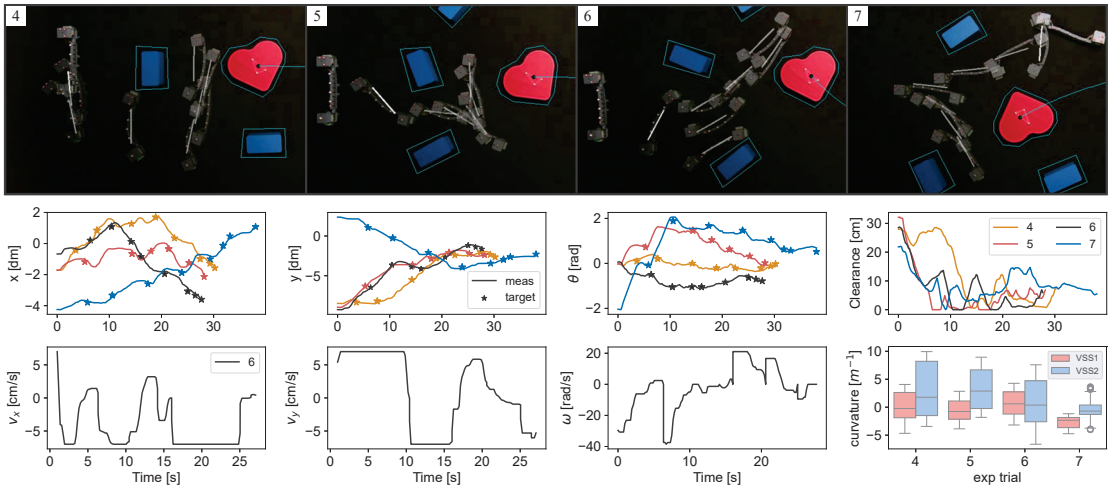

Figure 7.5: Top: Time-lapse sequence showing the 2SR robot navigating through a cluttered environment using the hybrid RRT*-APF path planning method in four different scenarios. **Bottom**: System response data during experiments, including: robot pose evolution, velocity control inputs and clearance measurements over time for trial "Heart 6", and box plots of VS segment curvature variations across trials (indicating rigidity maintenance).

between segments. Specifically, the second segment likely contains a lower volumetric fraction of Field's metal within its modular units, resulting in reduced thermal mass and diminished mechanical rigidity.

Notably, trial "Heart 7" presents an anomalous pattern with significantly reduced curvature fluctuations across both segments. This exceptional performance correlates directly with the predominant motion pattern in this particular scenario, which features primarily lateral displacement (movement along the robot's longitudinal axis) rather than forward/backward progression. This motion profile generates substantially lower bending moments across the robot's structure, as the primary forces align with the robot's axis of greatest stiffness. The reduced mechanical loading consequently minimizes flexural deformation, preserving the intended rigid-body kinematics essential for accurate navigation.

The systematic analysis of these navigation experiments demonstrates the robustness of our integrated planning and control framework across diverse environmental configurations. The controller successfully compensates for the inherent mechanical limitations of the variable stiffness design, maintaining sufficient positional accuracy while leveraging the morphological advantages of the 2SR robot. These navigational capabilities establish the essential foundation for the subse-

quent manipulation phase, enabling precise positioning of the robot prior to grasping engagement.

The comprehensive analysis of full-body grasping mechanics and object manipulation strategies has been presented in Chapter 6, where we examine the transition from navigation to interaction and the adaptive control methodologies employed during conformable manipulation tasks.

7.2 Motion Planning with Adaptive Morphology

While the RRT*-APF method demonstrated effectiveness in moderately cluttered environments, it encounters limitations in heavily obstructed scenarios. Fig. 7.6 illustrates a case where path planning fails: the target object is surrounded by obstacles positioned in a configuration that prevents direct robot navigation, causing RRT*-APF to fail despite extensive search attempts.

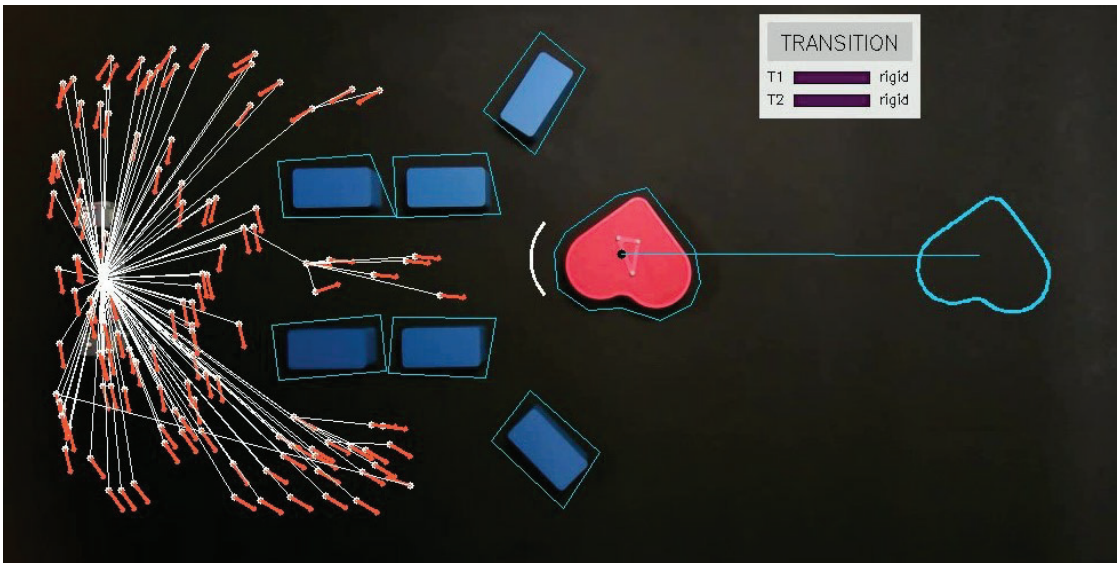

Figure 7.6: The **hybrid RRT*-APF** algorithm fails in a highly cluttered environment.

Problem 7.2.1. *The integration of shape adaptation significantly expands the configuration space to include five generalized coordinates, two stiffness states, four motion modes. This expansion introduces the challenge of planning not only motion trajectories but also coordinated shape deformations and stiffness transitions, resulting in a high-dimensional planning problem.*

To address this increased complexity, we developed a multi-step method that systematically decomposes the problem into manageable components, with each successive step refining the solution. The method consists of the following phases:

1. **Environment Analysis**: Utilizes Voronoi diagrams to identify theoretically traversable narrow passages. Voronoi diagrams are particularly suitable as they naturally identify the maximum clearance paths between obstacles.

2. **Critical Point Path Planning**: Determines feasible paths for three crucial robot points (front, middle, and rear) within the Voronoi graph. These points define the robot's fundamental shape during navigation.

3. **Configuration Fitting**: Maps feasible robot configurations to the identified point sequences and ensures the planned shapes are physically reachable.

4. **Traverse Configuration Selection**: Identifies key configurations that define the complete traverse.

This discrete, step-based approach significantly reduces computational complexity compared to continuous-space solutions, making it tractable for real-world applications. Each of these steps will be discussed in detail in the following subsections, providing comprehensive insight into the methodology and implementation of each phase.

7.2.1 Voronoi Analysis

The first step in our method involves analyzing the environment to identify potentially traversable narrow passages. We employ Voronoi diagrams, a geometric structure that partitions space based on the proximity to a set of points.

Definition 7.2.1 (Voronoi Cell)**.** *For an obstacle $\mathcal{O}_i \in \mathcal{O}$ within the workspace, its Voronoi cell $\mathcal{V}(\mathcal{O}_i)$ is the set of all points in the configuration space that are closer to $\mathcal{O}_i$ than to any other obstacle:*

$$\mathcal{V}(\mathcal{O}_i) = \{\mathbf{v} \in \mathbb{R}^2 \mid d(\mathbf{v}, \mathcal{O}_i) \leq d(\mathbf{v}, \mathcal{O}_j), \forall j \neq i\}, \tag{7.7}$$

where $d(\mathbf{v}, \mathcal{O}i) = \min_{\mathbf{p}\in\mathcal{O}_i} ||\mathbf{v} - \mathbf{p}||_2$ denotes the minimum Euclidean distance between point $\mathbf{v}$ and obstacle $\mathcal{O}_i$.

Definition 7.2.2 (Voronoi diagram)**.** *The complete Voronoi diagram* $\mathcal{V}(\mathcal{O})$ *is the collection of all Voronoi cells* $(\mathcal{V}(\mathcal{O}_i))_{\mathcal{O}_i \in \mathcal{O}}$*, partitioning the workspace into regions based on proximity to obstacles. The boundaries between adjacent Voronoi cells form the Voronoi edges, which represent points equidistant from the two nearest obstacles. The intersection of multiple Voronoi edges forms Voronoi vertices, which are equidistant from three or more obstacles.*

The Voronoi diagram provides a powerful spatial decomposition framework particularly well-suited for our robot navigation task due to several key properties::

- Voronoi edges represent paths of *maximum clearance* between obstacles, naturally biasing trajectory planning toward safer corridors in the workspace
- Voronoi vertices serve as critical decision points where multiple clearance-maximizing paths intersect, enabling efficient topological reasoning about viable navigation routes
- The diagram provides a complete decomposition of free space, systematically covering all potential passages regardless of environmental complexity.

This geometric structure enables us to transform the continuous navigation problem into a discrete graph search problem while preserving essential safety guaran-

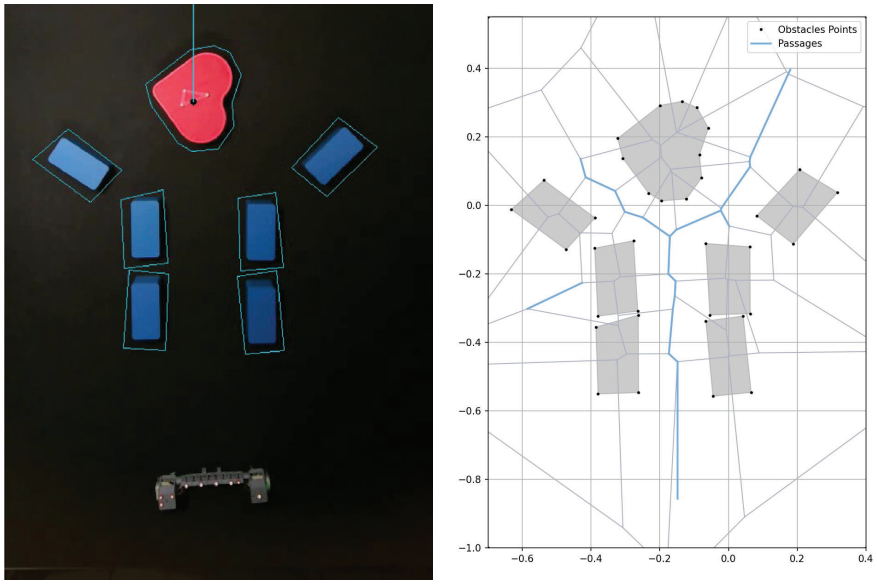

Figure 7.7: Left: Highly cluttered environment with detected obstacles. **Right**: Voronoi diagram of the environment. The traversable passages are highlighted in blue.

tees. Fig. 7.7 illustrates the resulting spatial decomposition in our experimental workspace.

From the Voronoi diagram, we construct a weighted graph $\mathcal{G} = (\mathcal{V}, \mathbf{E})$ where vertices $\mathcal{V}$ correspond to Voronoi vertices and edges $\mathbf{E}$ connect adjacent vertices along Voronoi edges. Each vertex $\mathbf{v} \in \mathcal{V}$ has an associated clearance defined as:

$$c(\mathbf{v}) = \min_{\mathcal{O}_i \in \mathcal{O}} d(\mathbf{v}, \mathcal{O}_i). \tag{7.8}$$

This clearance value represents the minimum distance between the vertex and any obstacle in the environment, providing a direct measure of navigational safety at that point.

Each edge $\mathbf{e} \in \mathbf{E}$ with endpoints $(\mathbf{v}_1, \mathbf{v}_2)$ has length $l(\mathbf{e})$ and clearance $c(\mathbf{e})$:

$$\begin{aligned} l(\mathbf{e}) &= ||\mathbf{v}_2 - \mathbf{v}_1||_2 \\ c(\mathbf{e}) &= \min(c(\mathbf{v}_1), c(\mathbf{v}_2)). \end{aligned} \tag{7.9}$$

Here, $l(\mathbf{e})$ represents the Euclidean length of the edge, which directly influences traversal time and energy expenditure. The edge clearance $c(\mathbf{e})$ provides a conservative initial estimate of minimum passage width along the edge, essential for determining whether the robot can safely navigate through this corridor.

While the Voronoi diagram inherently maximizes clearance, the elongated geometry of our 2SR robot necessitates more rigorous verification of passage traversability. For each candidate edge, we perform detailed clearance analysis by sampling a *passage* $\mathcal{S}_\mathbf{e}$ with k discretization points distributed uniformly along the edge:

$$\mathbf{p}_i = \mathbf{v}_1 + \frac{i}{k}(\mathbf{v}_2 - \mathbf{v}_1), \quad i \in \{0, 1, ..., k-1\}. \tag{7.10}$$

At each sampled point, we calculate precise clearance values and verify collision-free status, accounting for the robot's dimensional constraints and potential orientation configurations. The sampling density k is adaptively determined based on edge length and environmental complexity to ensure comprehensive coverage without excessive computational burden.

Lemma 1. *A passage $\mathcal{S}_\mathbf{e}$ between vertices $\mathbf{v}_1$ and $\mathbf{v}_2$ is traversable if $\forall \mathbf{p}_i \in \mathcal{S}_\mathbf{e}$: $\mathbf{p}_i \cap \mathcal{O} = \varnothing$, $\min_{\mathbf{p}_i \in \mathcal{S}} c(\mathbf{p}_i) \geq \tau$, and there exists at least one continuous connection between $\mathcal{S}_\mathbf{e}$ and another traversable passage*

This lemma establishes three critical conditions for passage traversability:

1. Complete collision avoidance ($\mathbf{p}_i \cap \mathcal{O} = \varnothing$) throughout the passage
2. Minimum clearance threshold satisfaction ($\min_{\mathbf{p}_i \in \mathcal{S}} c(\mathbf{p}_i) \geq \tau$), where τ represents the safety margin accounting for robot width, control uncertainty, and motion dynamics
3. Connectedness with the broader traversable network, ensuring the passage contributes to viable end-to-end navigation paths rather than forming isolated segments

The minimum clearance threshold τ is particularly important as it incorporates not only the robot's physical dimensions but also accounts for potential orientation-dependent variations in effective width and trajectory tracking errors that might occur during execution.

Following comprehensive traversability analysis, we construct a reduced graph $\hat{\mathcal{G}} = (\hat{\mathcal{V}}, \hat{\mathbf{E}}) \subseteq \mathcal{G}$ containing only verified safe passages:

$\hat{\mathbf{E}} = \{\mathbf{e} \in \mathbf{E} \mid \mathcal{S}_\mathbf{e}$ is traversable according to Lemma 1$\}$

The vertex set $\hat{\mathcal{V}}$ consists of all endpoints associated with traversable edges. This reduced graph $\hat{\mathcal{G}}$ offers several computational advantages:

- Significantly decreases search space complexity while preserving all viable navigation options
- Encodes critical clearance information for risk-aware path planning
- Provides topological guarantees about connectedness between regions

This representation serves as the foundation for subsequent high-level path planning, enabling efficient computation of clearance maximizing routes through the environment. By discretizing the continuous navigation problem while preserving safety guarantees, this approach strikes an optimal balance between computational efficiency and navigation performance.

7.2.2 Control Points Path Planning

Given the complex, high-dimensional configuration space of a 2SR in flexible mode, we introduce a geometric abstraction approach that reduces planning complexity while preserving navigational feasibility. This method focuses on three strategically selected characteristic points along the robot's length: the *rear* (r), *middle* (m), and *front* (f) control points. This minimal representation captures the robot's essential spatial occupancy requirements while supporting efficient path computation.

As illustrated in Fig. 7.8, these control points are defined as follows:

- *Front* point $\boldsymbol{\xi}_f$: The leading point during passage traversal, located at the head or tail locomotion unit depending on the intended direction of motion. This point serves as the navigation vanguard, probing the environment and determining initial entry feasibility into narrow corridors.
- *Middle* point $\boldsymbol{\xi}_m$: The central reference point of the robot, serving as the primary coordinate frame for motion planning and control.
- *Rear* point $\boldsymbol{\xi}_r$: The trailing point during traversal, which ensures that the entire robot body successfully clears obstacles during complex navigational maneuvers.

These control points are positioned symmetrically along the robot's centerline (assuming a default straight configuration) such that:

$$||\boldsymbol{\xi}_f - \boldsymbol{\xi}_m|| = ||\boldsymbol{\xi}_r - \boldsymbol{\xi}_m|| = \frac{L}{2}, \tag{7.11}$$

where L represents the robot's total length. This distribution ensures comprehensive coverage of the robot's physical extent while minimizing computational requirements during planning.

This carefully selected set of control points provides multiple advantages for navigation planning:

1. Enables efficient verification of passage traversability by checking clearance constraints at critical points
2. Ensures collision-free transitions between connected passages by capturing the robot's spatial extremities

3. Provides essential reference points for subsequent full-body configuration reconstruction using interpolation methods

4. Simplifies the high-dimensional planning problem to a more tractable sequence of waypoint assignments

Remark 18. *The selection of the front point depends on the environment. In most cases, either locomotion unit can be designated as front. However, when the manipulandum is asymmetrically obstructed, the choice depends on the accessibility relative to the body frame in the target (grasp) configuration that is determined according to (6.4): $\mathbf{q}' = [\mathbf{x}'_r, 0, 0]^\intercal$. The head locomotion unit is designated as front when the region corresponding to the negative x-axis of the body frame offers greater accessibility, while the tail LU is selected when the positive x-axis region is more accessible. This selection ensures that the robot's "hugging" front side will be properly oriented towards the manipulandum in the grasp configuration.*

For a specified target configuration $\mathbf{q}'$ (determined by task requirements), we first identify the global coordinates of the three target control points:

$$\boldsymbol{\Xi}' = \{\boldsymbol{\xi}_f(\mathbf{q}'), \boldsymbol{\xi}_m(\mathbf{q}'), \boldsymbol{\xi}_r(\mathbf{q}')\}. \tag{7.12}$$

These target points must be mapped to the traversable Voronoi graph $\hat{\mathcal{G}}$ to enable practical path planning. For each control point, we identify the nearest edge in the traversable graph. Formally, let $d(\boldsymbol{\xi}, \mathbf{e})$ denote the minimum Euclidean distance from point $\boldsymbol{\xi}$ to edge $\mathbf{e}$. The set of nearest edges for all target control points is then defined as:

$$\mathbf{E}' = \{\mathbf{e}_i \mid \mathbf{e}_i = \arg\min_{\mathbf{e}\in\hat{\mathbf{E}}} d(\boldsymbol{\xi}_i, \mathbf{e}), \boldsymbol{\xi}_i \in \boldsymbol{\Xi}'\}. \tag{7.13}$$

This mapping process connects the desired target configuration to the traversable network structure, establishing feasible goal locations within the graph.

The robot's entry to the passage network is determined by identifying the most accessible open-ended vertex closest to its initial position:

$$\mathbf{v}_0 = \arg\min_{\mathbf{v}\in\mathcal{V}'_{open}} ||\mathbf{v} - \mathbf{q}_0||, \tag{7.14}$$

where $\mathcal{V}'_{open} \subseteq \mathcal{V}'$ represents the subset of vertices with exactly one incident edge — typically corresponding to passage entrances or exits at the periphery of the environment. This formulation ensures that the robot begins its traversal from a feasible entry point with sufficient clearance.

After establishing both entry point and target locations within the graph, we proceed to compute optimal paths to each target control point. Let $\mathbf{V}(\mathbf{E}')$ denote the set of vertices incident to edges in $\mathbf{E}'$. For each vertex $\mathbf{v} \in \mathbf{V}(\mathbf{E}')$, we define $\mathcal{P}_\mathbf{v}$ as the complete set of possible paths from $\mathbf{v}_0$ to $\mathbf{v}$, where each path $\mathcal{P} \in \mathcal{P}_\mathbf{v}$ consists of a sequence of connected edges from $\hat{\mathbf{E}}$.

The optimal paths to all target vertices are efficiently determined using Dijkstra's algorithm, which guarantees minimum-cost traversal:

$$\mathcal{P}^* = \{\mathcal{P}_i^* \mid \mathcal{P}_i^* = \arg\min_{\mathcal{P} \in \mathcal{P}_{\mathbf{v}_i}} \sum_{\mathbf{e} \in \mathbf{P}} l(\mathbf{e}), \mathbf{v}_i \in \mathbf{V}(\mathbf{E}')\}. \tag{7.15}$$

This formulation prioritizes path length minimization while inherently preserving safety constraints through the underlying traversable graph structure.

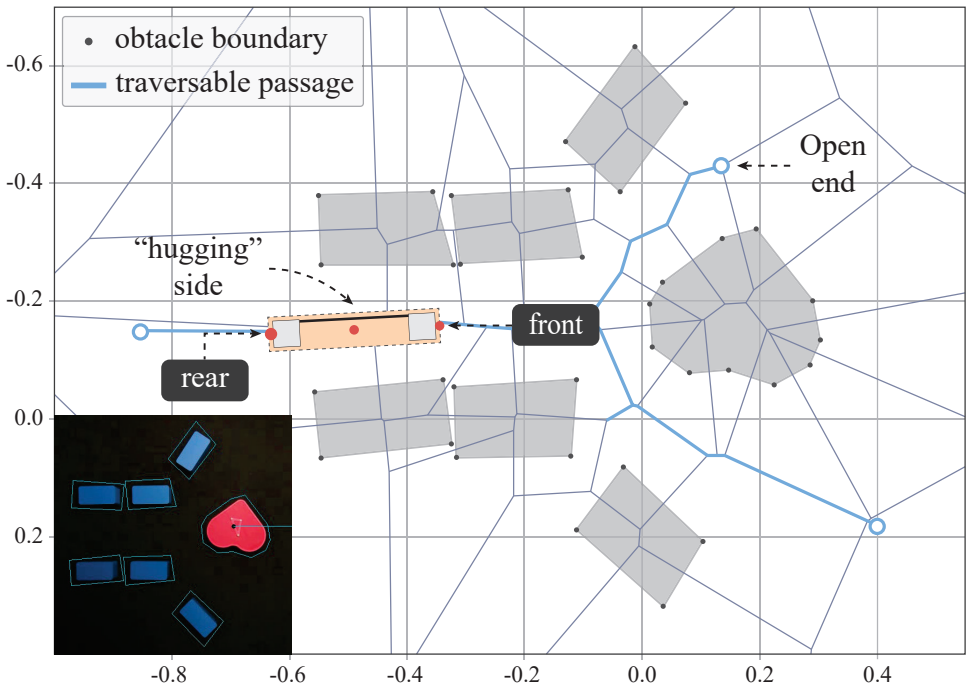

Figure 7.8: Voronoi diagram of the highly cluttered environment with detected obstacles. The location of critical points on the robot is highlighted in red.

Remark 19. *To ensure computational efficiency while maintaining path optimality, we implement a strategic vertex selection process. For each edge* $\mathbf{e} \in \mathbf{E}'$*, we include only one endpoint (*$\mathbf{v}_1$ *or* $\mathbf{v}_2$*) in* $\mathbf{V}(\mathbf{E}')$ *based on which vertex yields the shorter path from the entry point* $\mathbf{v}_0$*. This selective approach prevents redundant path calculations while preserving optimality guarantees.*

After determining the optimal path $\mathcal{P}_i^*$*, we compute the projection point* $\bar{\boldsymbol{\xi}}_i$ *on the corresponding edge* $\mathbf{e}_i$ *that is closest to the control point* $\boldsymbol{\xi}_i$*:*

$$\bar{\boldsymbol{\xi}}_i = \underset{\mathbf{p} \in \mathcal{S}_{\mathbf{e}_i}}{\arg\min} ||\mathbf{p} - \boldsymbol{\xi}_i||_2, \ \boldsymbol{\xi}_i \in \boldsymbol{\Xi}', \mathbf{e}_i \in \mathbf{E}'. \tag{7.16}$$

The final path is then augmented by adding an edge connecting vertex $\mathbf{v}$ *to the projection point* $\bar{\boldsymbol{\xi}}_i$*.*

This final refinement step allows for exact positioning of each control point while maintaining the path's connectivity with the traversable network. The projection mechanism enables smooth transitions from the discretized Voronoi graph to continuous workspace positions, facilitating precise alignment with the desired target configuration.

The resulting control point paths provide a sequence of waypoints that guide the robot from its initial position to the target configuration while respecting all environmental constraints. These paths serve as the foundation for subsequent detailed trajectory planning, where continuous curves will be generated to smoothly connect the sequence of waypoints while maintaining clearance constraints and ensuring kinematic feasibility for the snake-like robot's articulated structure.

Path Coordination under Physical Constraints

While the individual paths computed for the front, middle, and rear control points provide initial guidance through the passage network, a critical challenge emerges: these independently optimized paths may violate the physical constraints of the robot's structure. Variable stiffness bridge is inextensible therefore 2SR robot's body cannot arbitrarily stretch or compress to follow arbitrary point trajectories. Instead, we must coordinate these paths to maintain the physical integrity of the robot throughout the navigation process.

Problem 7.2.2. *The fundamental challenge in path coordination stems from the robot's inherent structural constraints. 2SR robot consists of three critical control points connected by segments of fixed length, forming an articulated chain-like structure. Throughout the motion sequence, these inter-point distances must remain constant, reflecting the robot's physical properties and preventing any unrealistic deformations. This constraint transforms the planning problem from independent point navigation to a coordinated chain propagation through the environment.*

Our solution employs a biomimetically-inspired rear-driven propagation strategy that mirrors the natural locomotion patterns observed in biological snake movement. We designate the rear point's path $\mathcal{P}_r^*$ as the primary reference trajectory, treating it as the "pushing" or driving end of the robot through the passage sequence. This approach offers several advantages:

1. It naturally emulates the physical behaviour of snake-like organisms pushing through confined spaces
2. It simplifies the coordination problem by establishing a clear causal relationship between control points
3. It provides robust handling of narrow passages where the rear segment must actively propel the body forward

This rear-driven approach is particularly effective in highly constrained environments, where the trailing end of the robot must exert force to propel the middle and front segments through narrow apertures. By prioritizing the rear path, we ensure that the robot's motion remains physically realizable throughout the navigation.

To implement this coordination strategy, we first generate a dense sequence of sample points $\mathcal{S}_r = (\mathcal{S}_\mathbf{e})_{\mathbf{e}\in\mathcal{P}_r^*}$ along the edges in the rear point's path $\mathcal{P}_r^*$. These sample points represent discrete positions of the rear control point as it traverses through the environment.

For each rear point position $\boldsymbol{\xi}_r(k) \in \mathcal{S}_r$ at time step k, we determine the corresponding locations of the middle and front points $\boldsymbol{\xi}_m(k)$ and $\boldsymbol{\xi}_f(k)$ subject to the

following physical constraints:

$$\begin{cases} d\hat{\mathcal{G}}(\boldsymbol{\xi}_f(k), \boldsymbol{\xi}_r(k)) = L, \\ d\hat{\mathcal{G}}(\boldsymbol{\xi}_m(k), \boldsymbol{\xi}_f(k)) = d\hat{\mathcal{G}}(\boldsymbol{\xi}_m(k), \boldsymbol{\xi}_r(k)) = \frac{L}{2}, \end{cases} \tag{7.17}$$

where $d_{\hat{\mathcal{G}}}(\cdot, \cdot)$ is the geodesic distance measured along edges in the traversable graph $\hat{\mathcal{G}}$, and L denotes the robot's total length. These constraints ensure that the physical length of the robot is preserved at all times, maintaining a constant distance between control points along the navigation path.

The computation of these coordinated positions requires solving a constraint satisfaction problem at each time step. For the middle point $\boldsymbol{\xi}_m(k)$, we identify locations that are equidistant from both the rear and front points along the graph. For the front point $\boldsymbol{\xi}_f(k)$, we identify locations that maintain the proper distance L from the rear point. These positions are computed incrementally as the rear point advances along its path, creating a cascading effect where the rear point's motion directly influences the positions of the middle and front points.

The coordination process requires special handling at network branching points where multiple navigational options become available. Our algorithm employs a hierarchical decision-making strategy at these junctions. When propagating the middle and front points, we first prioritize edges that appear in their respective guidance paths $\mathcal{P}_m^*$ and $\mathcal{P}_f^*$, maintaining alignment with the individually optimized routes whenever possible.

However, as the propagation continues, these points may eventually be pushed beyond their original guidance paths due to physical constraints. In such cases, we dynamically select the next edge connected to their last visited edge based on topological properties of the network. When multiple candidate edges exist, we preferentially select edges incident to vertices with higher degree in $\hat{\mathcal{G}}$ (i.e., vertices with more connections), as these typically represent junctions with greater navigational flexibility and clearance.

This adaptive edge selection enables the algorithm to effectively handle situations where physical constraints force deviations from the initially computed optimal paths, ensuring continuous progress through the environment while maintaining the robot's structural integrity.

Remark 20. *This decision-making strategy implements a form of* "rolling horizon" planning*, where the algorithm continuously adapts the front and middle point trajectories based on the current state and physical constraints, while maintaining alignment with the pre-computed guidance paths whenever possible. The preference for high-degree vertices during divergence from guidance paths reflects a heuristic bias toward regions with greater navigational options, reducing the likelihood of reaching dead ends or highly constrained configurations.*

In particularly complex environments with tight turns or narrow passages, the algorithm may encounter situations where maintaining exact distances between control points becomes challenging within the discrete graph representation. To address this, we implement a two-phase resolution strategy:

1. First, we attempt to satisfy constraints using only edges within the $\hat{\mathcal{G}}$ graph, following the safety guarantees provided by the Voronoi-based decomposition

2. If no exact solution exists within the graph, we permit limited off-graph interpolation between adjacent edges, creating smooth transitions that satisfy the physical constraints while staying within the verified collision-free regions

This approach ensures that the robot's configuration remains valid throughout the navigation sequence, even in highly constrained environments where the graph representation may not perfectly capture all possible configurations.

By coordinating the paths of all control points through this rear-driven propagation approach, we generate a physically consistent trajectory that guides the snake-like robot through complex environments while respecting both environmental constraints and the robot's structural limitations. The resulting coordinated path serves as the foundation for detailed trajectory planning and control execution, enabling reliable navigation even in highly cluttered spaces.

Paths Smoothing and Optimization

The path planning through Voronoi passages, while ensuring feasibility and safety, often results in trajectories containing unnecessary fluctuations and sharp turns. These artifacts, inherent to Voronoi diagrams, may lead to jerky motions and inefficient trajectories. Therefore, a final smoothing step is crucial to refine the raw paths while preserving their essential navigational properties.

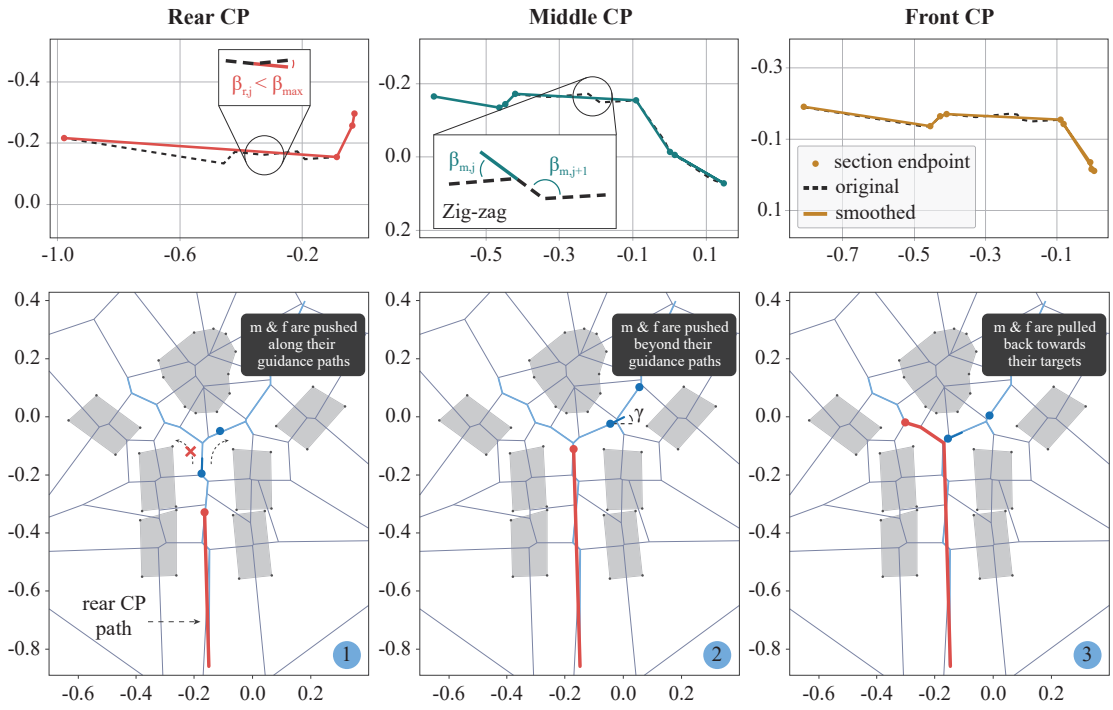

Figure 7.9: Path optimization results for articulated robot navigation. **Top**: Comparison of paths before and after smoothing optimization. **Bottom**: Evolution of the robot's motion through the workspace, showing the Voronoi diagram and the coordinated movement of the three control points.

Problem 7.2.3. *Path planning through Voronoi analysis, while ensuring feasibility, often results in trajectories containing unnecessary fluctuations and sharp turns. These artifacts, inherent to Voronoi diagrams, can lead to jerky motions and excessive shape deformations of a 2SR robot. A smoothing step is therefore crucial to refine the raw paths while preserving their essential navigational properties and maintaining clearance constraints.*

The smoothing process begins with geometric analysis of the path structure, treating it as a collection of straight sections. Each j-th section in $\mathcal{S}_i$, $i \in \mathbb{S}$, $\mathbb{S} = \{r, m, f\}$ is characterized by its direction vector $\vec{\mathbf{d}}_{i,j}$ and length $l_{i,j}$. The smoothing strategy employs a two-phase approach.

The first phase focuses on section merging, targeting situations where adjacent path sections are nearly parallel. For two consecutive sections, we compute their directional similarity:

$$\cos \beta_{i,j} = \frac{\vec{\mathbf{d}}_{i,j} \cdot \vec{\mathbf{d}}_{i,j+1}}{||\vec{\mathbf{d}}_{i,j}|| \cdot ||\vec{\mathbf{d}}_{i,j+1}||}. \tag{7.18}$$

When $\beta_{i,j} < \beta_{max}$, these sections are merged through cubic spline interpolation, eliminating small oscillations while maintaining the path's overall structure.

The second phase addresses zigzag patterns that typically emerge when the path navigates between multiple obstacles. For any three consecutive sections, we analyze the total direction change:

$$\Delta\beta_{i,j} = |\beta_{i,j} - \beta_{i,j+1}|. \tag{7.19}$$

If $\Delta\beta_{i,j} < \Delta\beta_{max}$, we replace the zigzag pattern with a single straight section while preserving endpoint positions and ensuring clearance constraints are maintained.

Finally, we perform uniform resampling to generate equally spaced points along the smoothed paths $\mathcal{S}_r^*$, $\mathcal{S}_m^*$, and $\mathcal{S}_f^*$, ensuring they contain the same number of points. Implementation of this path optimization is illustrated in Fig. 7.9.

7.2.3 Fitting Configurations

After generating coordinated paths for the critical control points, we face the essential challenge of reconstructing complete robot configurations that satisfy these waypoints while maintaining both physical feasibility and kinematic constraints. This process translates the simplified point-based representation back into the full 5-dimensional configuration space of the 2SR robot.

Problem 7.2.4. *For each n-th timestep along the path, we must determine the optimal robot configuration $\mathbf{q}_n$ that accurately positions the control points at their desired locations while ensuring mechanical feasibility and maintaining smooth transitions between consecutive states. This configuration must respect the robot's intrinsic constraints such as maximum curvature limitations.*

We formulate this reconstruction process as a constrained multi-objective optimization problem that balances positional accuracy, motion smoothness, orienta-

tion alignment, and shape simplicity:

$$\begin{aligned} \underset{\mathbf{q}_n \in \mathbb{R}^5}{\text{minimize}} \quad & \sum_{i \in \mathbb{S}} w_i ||\boldsymbol{\xi}_i(\mathbf{q}_n) - \mathcal{S}_i^*(n)||_2 + \tilde{\mathbf{q}}_n^\intercal \mathbf{W} \tilde{\mathbf{q}}_n + \\ & + \lambda_\theta |\theta_{b,n} - \gamma_n| + \lambda_\kappa (|\kappa_{1,n}| + |\kappa_{2,n}|) \\ \text{subject to} \quad & \tilde{\mathbf{q}}_n = \mathbf{q}_n - \mathbf{q}_{n-1} \\ & |\kappa_{j,n}| \leq \frac{\pi}{2l}, \; j \in \{1, 2\}, \end{aligned} \tag{7.20}$$

where $\mathbb{S} = \{f, m, r\}$ represents the set of critical control points, and $\boldsymbol{\xi}_i(\mathbf{q}_n)$ denotes the forward kinematics mapping from configuration space to the global position of the i-th control point.

This objective function carefully balances four key requirements through its component terms:

1. *Positional Accuracy:* The first term $\sum_{i \in \mathbb{S}} w_i ||\boldsymbol{\xi}_i(\mathbf{q}_n) - \mathcal{S}_i^*(n)||_2$ ensures accurate positioning of all critical points, minimizing the weighted Euclidean distance between the actual and desired positions. The weights w_i allow for prioritization, typically giving higher importance to the middle point ($w_m > w_f, w_r$) as it serves as the primary reference for overall positioning.

2. *Motion Smoothness:* The second term $\tilde{\mathbf{q}}_n^\intercal \mathbf{W} \tilde{\mathbf{q}}_n$ penalizes large changes between consecutive configurations, promoting smooth transitions in the configuration space. The matrix $\mathbf{W}$ is a positive definite weighting matrix that allows differential emphasis on various configuration components. Typically, we assign higher weights to changes in body orientation and segment curvatures compared to translational components, as abrupt changes in these parameters lead to more noticeable jerky motions.

3. *Orientation Alignment:* The term $\lambda_\theta |\theta_{b,n} - \gamma_n|$ enforces alignment between the robot's body orientation $\theta_{b,n}$ and the desired direction γ_n. This direction is computed as the tangent vector at the middle point's position $\mathcal{S}_m^*(n)$ oriented toward the tail locomotion unit, ensuring that the robot's body naturally aligns with the path's directionality.

4. *Shape Simplicity:* The final term $\lambda_\kappa (|\kappa_{1,n}| + |\kappa_{2,n}|)$ introduces a preference for minimal absolute curvatures in both segments, discouraging unnecessary

bending when straighter configurations are viable. This regularization promotes more natural-looking configurations and reduces mechanical stress on the robot's joints.

The weighting parameters (w_i, λ_θ, λ_κ) play a crucial role in determining the robot's behaviour across different environmental contexts. For instance:

- In narrow passages, we increase the positional accuracy weights (w_i) to ensure precise adherence to the planned safe trajectory
- During sharp turns, we reduce the orientation alignment weight (λ_θ) to permit greater deviation from path tangency, allowing the robot to execute the turn more naturally
- In open areas, we increase the curvature minimization weight (λ_κ) to prefer straighter configurations that optimize speed and efficiency

This adaptive weighting strategy enables the robot to exhibit context appropriate behaviours across varying environmental conditions, balancing multiple competing objectives.

Remark 21. *This constrained optimization problem is solved sequentially along the path using Sequential Least Squares Programming (SLSQP), which efficiently handles the nonlinear objective function with mixed equality and inequality constraints. The process begins with the initial configuration and progresses forward in time, with each optimized solution $\mathbf{q}_{n-1}$ serving as the initial guess for the subsequent optimization at timestep n. This sequential approach exploits temporal coherence to improve computational efficiency and solution stability.*

7.2.4 Discretizing Crucial Configurations

After obtaining a continuous path of robot configurations, we must address a fundamental limitation:

Problem 7.2.5. *A physical 2SR robot cannot execute continuous shape changes with arbitrary precision in a flexible state, especially when target configurations are significantly distant from each other. Substantial planar displacements require omnidirectional motion of the robot in a rigid state.*

This limitation reflects the practical constraints of robotic systems, where continuous shape changes may require complex control mechanisms, excessive energy expenditure, or may simply exceed the robot's mechanical capabilities. Rather than pursuing an idealized but impractical continuous deformation trajectory, we develop a systematic approach to identify a discrete sequence of key configurations that effectively capture the essential characteristics of the planned motion.

This discretized representation provides a series of target configurations that can be sequentially supplied to the *Motion & Morphology Controller* for execution by the physical robot. The robot can then navigate between these configurations using a combination of rigid-state motion and flexible-state shape adjustment, leveraging the strengths of each operational mode while respecting their limitations.

Our discretization process employs a rigorous mathematical framework based on three complementary criteria that identify configurations of particular significance along the continuous path:

1. *Curvature Extrema Analysis:* Let $\kappa_j(n)$ be a curvature function for the j-th VS segment along the robot configuration path with a path length parameter n. We identify local extrema where:

$$\frac{d\kappa_j}{dn} = 0 \text{ and } \left|\frac{d^2\kappa_j}{dn^2}\right| > 0, \quad j \in 1, 2. \tag{7.21}$$

   Specifically, we detect peaks and valleys where $|\kappa_j| > \eta$.

2. *Flat Region Detection:* We perform flat region detection by identifying regions of approximately constant curvature where:

$$\frac{1}{\Delta n}\sum_{n=n_1}^{n_2}\left|\frac{d\kappa_j}{dn}\right| < \epsilon, \tag{7.22}$$

   where ϵ is a small threshold and $\Delta n = n_2 - n_1$ represents the length of the evaluated region. These flat regions correspond to configurations where the robot maintains a consistent shape while moving through uniform passages or open areas. By identifying the midpoints or representative configurations within these regions, we capture the stable morphologies that should be maintained during portions of the trajectory.

3. *Spatial Extrema:* Finally, we include configurations at spatial extrema:

$$\begin{cases} \arg\min_n \mathbf{p}(n) \\ \arg\max_n \mathbf{p}(n), \end{cases} \tag{7.23}$$

where $\mathbf{p} = [x_b, y_b]^\intercal$ is a robot position vector. These extrema capture the outermost positions reached by the robot during navigation, ensuring that the discretized sequence covers the full spatial extent of the planned trajectory. This is particularly important for ensuring that the robot can reach positions near obstacles or at the boundaries of the navigable space.

After applying these criteria to generate an initial set of crucial configurations $\mathcal{Q}$, we perform a refinement step to eliminate redundancy through a proximity filter:

$$\mathcal{Q}^* = \{\mathbf{q}_i \in \mathcal{Q} : ||\mathbf{p}_i - \mathbf{p}_{i+1}||_2 > d_{\min},\ \mathbf{p}_i \in \mathbf{q}_i, \tag{7.24}$$

where $d_{\min}$ represents a minimum distance threshold in the workspace. This filtering ensures that consecutive configurations in the final sequence are sufficiently distinct to warrant separate execution, preventing redundant shape changes that would unnecessarily complicate the robot's motion or consume additional energy.

The proximity filter also incorporates orientation and curvature differences to ensure that configurations with similar positions but different shapes are properly preserved. This is implemented by using a weighted distance metric in the full configuration space rather than just positional distance.

As illustrated in Fig. 7.10, the resulting discrete sequence of robot configurations $\mathcal{Q}^* = \{\mathbf{q}_1, \mathbf{q}_2, ..., \mathbf{q}_k\}$ provides a comprehensive set of waypoints that captures the essential morphological adaptations required for successful navigation through the environment. This visualization demonstrates how the robot progressively adjusts its shape to navigate through narrow passages, execute turns, and reach the target position while maintaining appropriate clearance from obstacles.

The discretization process significantly reduces the number of target configurations that must be communicated to the robot controller while preserving the navigational intent of the original continuous trajectory. This reduction in complexity facilitates more efficient implementation on physical hardware with limited computational resources and control bandwidth.

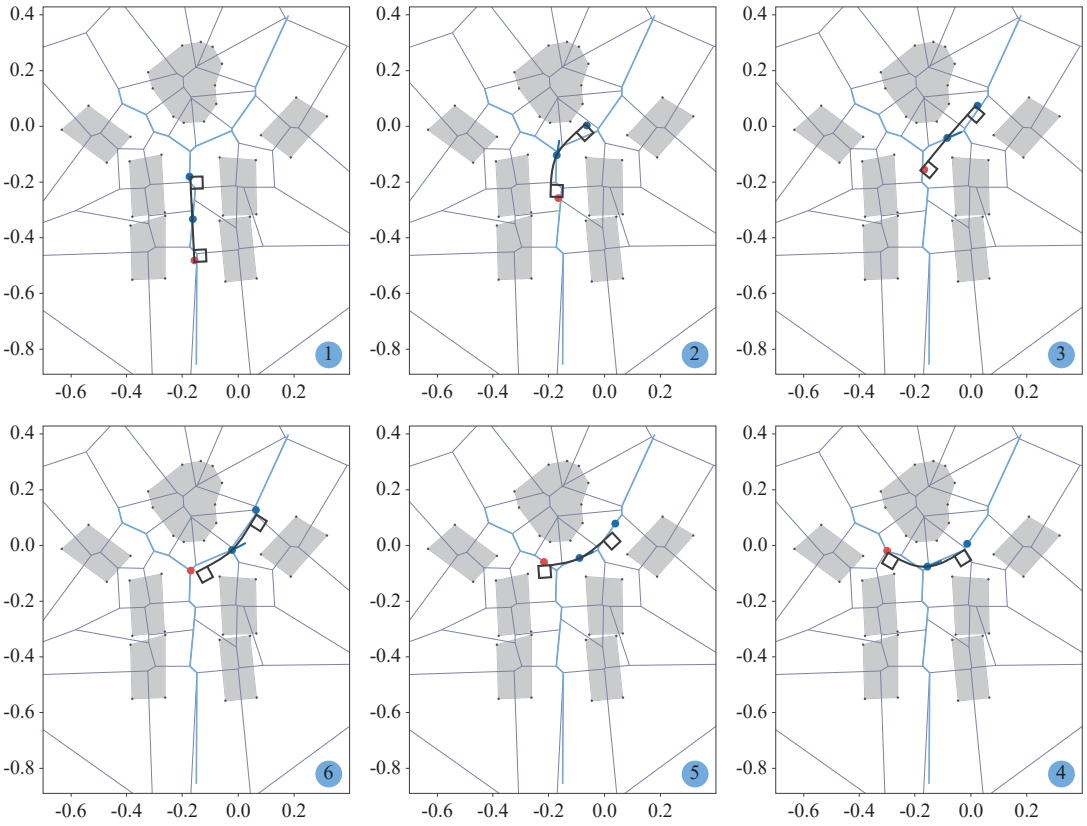

Figure 7.10: Evolution of the robot's crucial configurations through the workspace. Configurations are reconstructed from the robot control points.

We denote this integrated approach as **VAMP (Voronoi-Assisted Morphological Planning)**, which encompasses the complete pipeline from environment perception and Voronoi decomposition through path planning, configuration fitting, and final discretization.

The VAMP framework offers several key advantages:

1. **Safety-Biased Planning:** By leveraging Voronoi diagrams, the framework inherently maximizes clearance from obstacles, enhancing navigational safety

2. **Practical Feasibility:** The discretization process ensures that the planned motion respects the physical limitations of the robot hardware

3. **Computational Efficiency:** By reducing the continuous trajectory to a smaller set of key configurations, the approach minimizes the computational burden during execution

4. **Adaptive Morphology:** The selected configurations capture crucial shape changes required to adapt to environmental constraints, ensuring successful navigation through complex spaces

The discretized configuration sequence serves as the final output of the planning phase, providing concrete targets for the robot's control system. During execution, the robot will transition between these configurations through a combination of rigid-state locomotion and flexible-state shape adjustment, leveraging the complementary capabilities of both operational modes to achieve effective navigation through the environment.

7.2.5 Experiment and Performance Analysis

To validate the effectiveness of the proposed VAMP method, we conducted a series of experiments in challenging navigation scenarios. The experimental setup mirrors our previous validation of the RRT*APF method, enabling direct comparison while testing the enhanced capabilities of VAMP in more complex environments.

We designed four distinct navigation scenarios with increasing complexity, featuring 3-5 obstacles strategically placed to create challenging passage configurations. Unlike previous experiments, the obstacles were positioned to create narrow corridors and confined spaces that specifically test the manipulandum's shape-changing capabilities. Similarly to the RRT*APF experiment, the robot's task consists of three phases: traverse, grasp and transport.

Path Planning Results

Fig. 7.11 illustrates the robot configuration sequences generated by the VAMP method across four distinct scenarios. The planning process begins by transforming each workspace into a Voronoi diagram, which automatically identifies maximum-clearance pathways through the environment. The traversable passages (highlighted in blue) represent corridors with sufficient width for robot navigation after filtering based on minimum clearance requirements.

For each scenario, VAMP generates an optimized sequence of configurations $\mathcal{Q}^*$ comprising just four to five key waypoints. These sequences start with the robot in its default straight configuration and progressively adapt to environmental

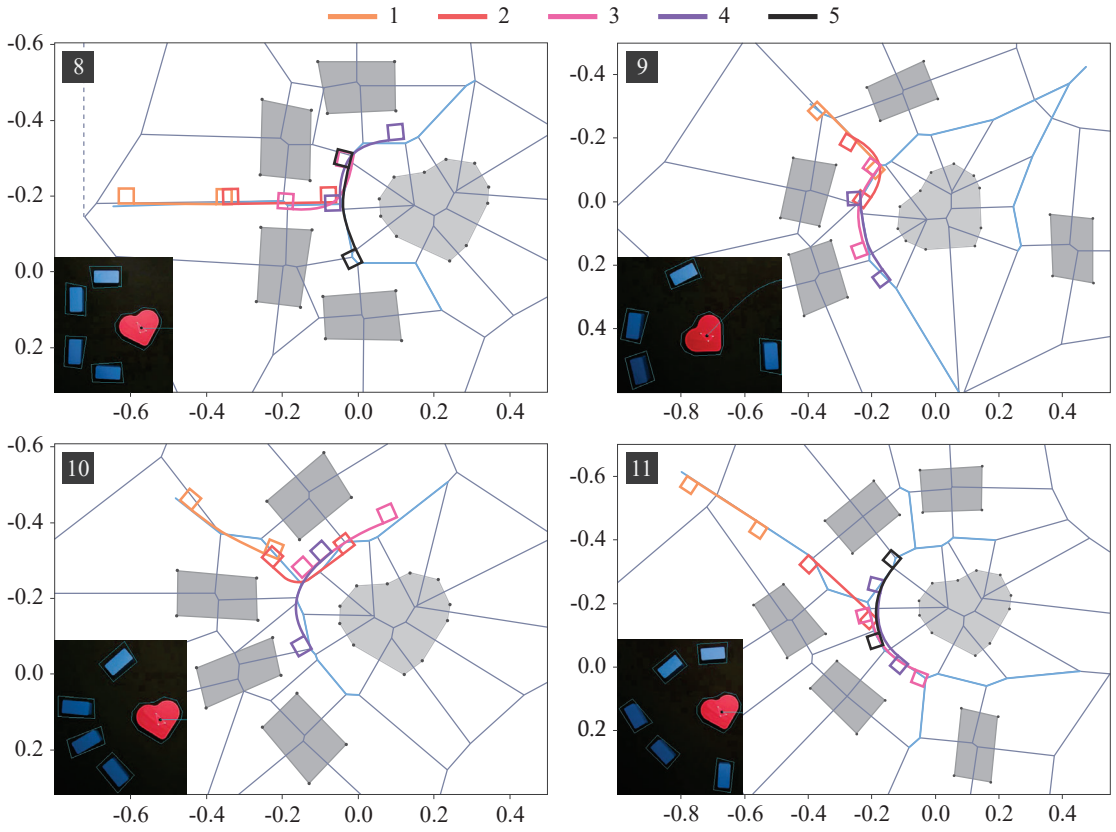

Figure 7.11: Time-lapse sequence showing the 2SR robot navigating through a densely cluttered environment using the VAMP motion and morphology planning method in four different scenarios.

constraints. The method determines the minimum deformation needed for the robot to navigate through constricted areas while maintaining adequate clearance from obstacles.

Several notable features are evident across the scenarios. The method consistently follows a minimal deformation principle by maintaining straighter configurations in areas with generous clearance and only deforms when necessary to navigate constrictions. This approach minimizes energy expenditure while ensuring safety. The configurations also show remarkable environmental awareness, with the robot adopting appropriate curvatures that align with passage geometry — whether S-shaped configurations, C-shaped bends, or more complex compound curves are required.

The resulting sequence shows smooth, gradual shape transitions rather than abrupt changes, enhancing executability by the physical robot. Each configura-

tion serves as a logical intermediate step toward the next, creating a progression that respects the robot's physical capabilities. Throughout all scenarios, adequate clearance from obstacles is maintained, accommodating potential control inaccuracies during physical execution.

The scenarios demonstrate VAMP's versatility in handling various environmental challenges. These include navigation through corridors with offset obstacles requiring gentle S-curves, tight passages demanding more pronounced bending, complex multi-turn scenarios necessitating sequences of coordinated bends, and asymmetric environments requiring correspondingly asymmetric shape adaptations.

Task Execution

After determining the set of target configurations $\mathcal{Q}^*$ through the VAMP framework, we implemented the planned motion on our physical 2SR robot system. To ensure smooth transitions between the crucial configurations identified during planning, we enhanced the path with intermediate waypoints using an adaptive interpolation approach. The interpolation density varied based on spatial distance—inserting either one or two additional configurations between consecutive waypoints depending on their separation in the workspace. This adaptive scheme balanced motion smoothness with computational efficiency, providing denser sampling for larger configuration changes while avoiding redundancy for closely spaced waypoints.

The resulting interpolated configuration sequence was then passed to the Motion & Morphology (M&M) controller for physical execution on the robot. The complete navigation tasks required considerable execution time, ranging from approximately 2 to 11 minutes across different trials. This extended duration primarily stemmed from the multiple stiffness transition cycles necessary for safe navigation through the complex environments. Each transition between rigid and soft states requires a physical morphological change in the robot's variable stiffness segments, which necessarily consumes time due to the mechanical nature of the stiffening process.

Fig. 7.12 provides a detailed visual documentation of the robot's navigation through a cluttered obstacle course. The sequential photographs capture key moments throughout the execution, revealing the robot's dynamic capabilities:

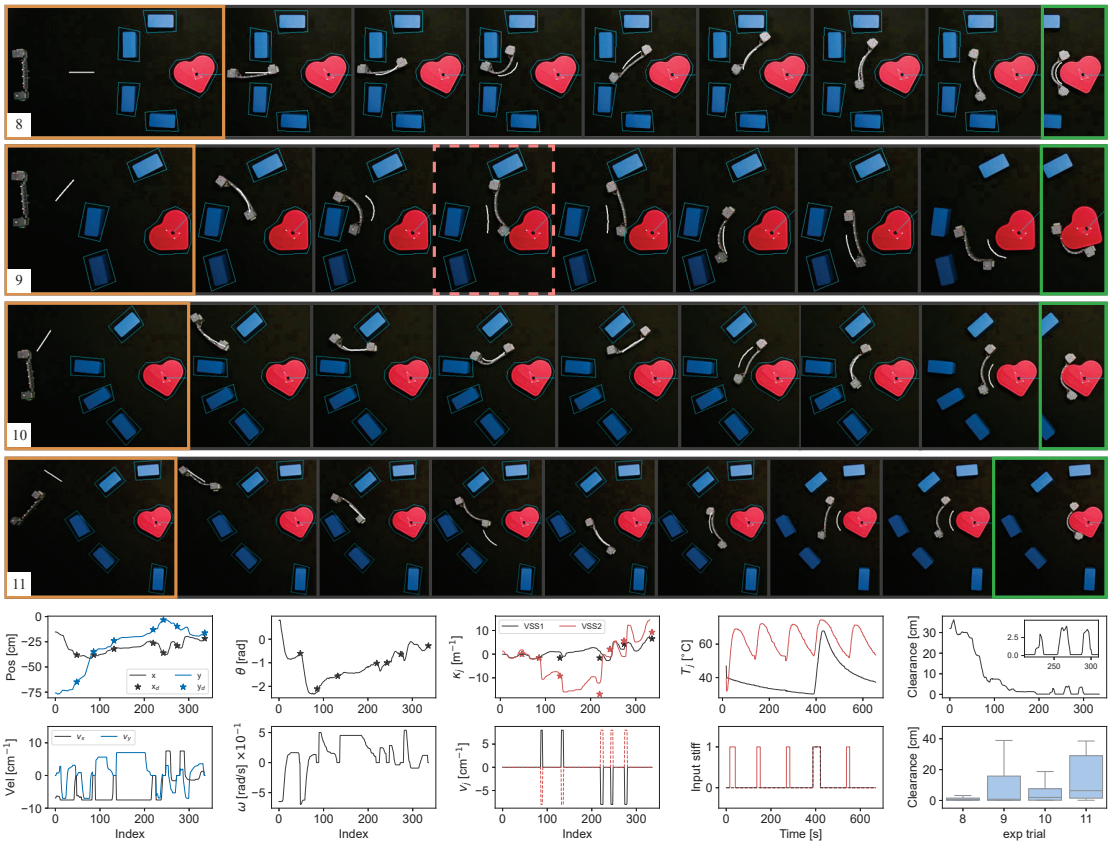

Figure 7.12: Sequential photographs illustrating the execution of a planned path by the 2SR robot through a cluttered environment. The robot transitions between rigid and soft states to navigate around obstacles. The yellow-framed photo marks the start configuration, while the green-framed photo shows the final grasping state. A pink dashed frame highlights a moment when the robot entered the safety zone but avoided direct obstacle contact.

stiffness switching between rigid and soft states, transitions between different motion modes, and adaptive morphological deformation in response to environmental constraints. The execution sequence begins with the yellow-framed photograph showing the robot in its initial configuration, proceeds through a series of carefully executed maneuvers around obstacles, and concludes with the green-framed photograph depicting the robot in its final configuration reaching the target object for grasping.

Throughout the navigation sequence, the robot dynamically adjusts its stiffness state according to the needs of each phase. It maintains rigid segments during omnidirectional locomotion phases for precise positioning, then transitions specific segments to the soft state when shape adaptation is required to navigate tight spaces. Of particular note is a moment highlighted by a pink dashed frame, where

the robot momentarily entered a safety buffer zone near an obstacle but successfully avoided any physical contact. This incident demonstrates the robustness of the planning and control framework even when operating near the boundaries of the safety constraints.

Quantitative performance data presented in Fig. 7.12 provides deeper insight into the robot's behaviour during trial "Heart 10." The plots track robot state responses and velocity control inputs throughout the execution, revealing the complex interplay between position control, orientation adjustment, and stiffness state transitions. This data showcases the controller's ability to handle the multi-modal nature of the robot's operation, smoothly transitioning between different control regimes as needed.

The trials exhibited varying degrees of complexity in terms of required morphological adaptations. In the challenging "Heart 10" scenario, the second variable stiffness segment underwent ten phase transitions (five rigid-to-soft and five soft-to-rigid cycles) with significant deformation, while the first segment required only two stiffness transitions with a single deformation. In contrast, trial "Heart 11" represented the simplest case, requiring just one deformation in each segment. Other trials fell between these extremes, typically requiring 3-4 deformations (6-8 phase transitions) per segment. These differing requirements directly impacted completion times: the complex "Heart 10" trial took nearly 11 minutes to complete, while the simpler "Heart 11" finished in just 2.5 minutes. Trials "Heart 8" and "Heart 9" completed in 9.45 and 8.87 minutes respectively.

Clearance measurements during these experiments revealed consistently lower values compared to previous experiments, reflecting the more constrained nature of the workspaces. As the robot navigated and deformed in the confined spaces between obstacles and the manipulandum, its locomotion units frequently approached the edges of obstacle buffer zones. This behaviour is evident in the clearance plot in Fig. 7.12, where values fluctuate considerably and often approach zero during deformation phases near obstacles. Despite these challenges, the 2SR robot generally maintained safe distances from physical obstacles.

One notable exception occurred during trial "Heart 9" (highlighted with a red frame in Fig. 7.12), where the robot briefly violated the buffer zone boundary. Importantly, even in this instance, no physical collisions occurred, and neither

the obstacles nor the manipulandum were disturbed despite the technical safety boundary violation. This demonstrates the inherent robustness of the system, where the safety margins built into the planning process provide a buffer against minor execution inaccuracies.

The box plot in Fig. 7.12 summarizes clearance measurements across all trials, providing a statistical perspective on navigational safety in different scenarios. Trial "Heart 8," featuring the most congested workspace, predictably exhibited the lowest average clearance values, while the simpler "Heart 11" trial maintained consistently higher clearances. This data quantitatively confirms the visual observation that more complex environments necessitate operation with tighter clearances, pushing the system closer to its performance limits.

These experimental results validate the effectiveness of the VAMP planning framework for generating executable configuration sequences that enable a 2SR robot to successfully navigate complex, cluttered environments through a combination of adaptive morphology changes and multi-modal locomotion strategies.

7.3 Summary

This chapter presents a comprehensive exploration of path planning strategies for elongated mobile robots navigating through cluttered environments. The research addresses the unique challenges posed by robots with extended geometries, where orientation and shape become critical factors in successful navigation - a significant departure from traditional point-mass robot planning problems.

This chapter develops two complementary planning approaches:

1. **Hybrid RRT*-APF method** for scenarios where fixed morphology
2. **VAMP framework** for complex environments requiring adaptive shape changes

Both approaches enable a 2SR robot to successfully navigate, approach, and grasp objects in constrained spaces.

The **hybrid RRT*-APF method** efficiently decomposes the planning problem into position search and orientation control. It leverages Rapidly-exploring

Random Trees (RRT*) for efficient workspace exploration and Artificial Potential Fields (APF) to determine optimal orientations that consider obstacle proximity, goal alignment, and path smoothness. This decomposition significantly reduces computational complexity while generating smooth, executable trajectories. The method introduces an orientation control algorithm that balances multiple competing objectives through a weighted potential function, creating an effective guidance system for elongated robots.

For path planning with fixed morphology, the chapter introduces a three-phase grasping strategy:

1. Approach with default shape
2. Grasp without contact
3. Final contact

This systematic approach enables precise positioning relative to target objects. The planning process carefully considers the robot's rectangular boundary during navigation, ensuring collision-free paths through moderately complex environments. The resulting trajectories demonstrate effective obstacle avoidance while maintaining appropriate orientation transitions, particularly the front-loaded adjustment strategy that establishes proper alignment early in the trajectory.

When confronted with highly cluttered environments where fixed morphology proves insufficient, the chapter introduces the innovative **VAMP (Voronoi Assisted Morphological Planning) framework**. This method expands planning into the full configuration space, addressing the high-dimensional challenge of coordinating motion, shape changes, and stiffness transitions. VAMP systematically decomposes this complex problem through four key phases that progressively refine the solution from environmental analysis to executable robot configurations.

First, Voronoi diagrams identify maximum-clearance pathways between obstacles, automatically detecting traversable passages. Second, coordinated paths are planned for three critical control points (front, middle, and rear) that maintain physical constraints of the robot's structure through a biomimetically-inspired rear-driven propagation strategy. Third, complete robot configurations are reconstructed through multi-objective optimization that balances positional accuracy,

motion smoothness, orientation alignment, and shape simplicity. Finally, crucial configurations are discretized to create a minimal set of waypoints capturing essential shape changes through rigorous mathematical criteria including curvature extrema analysis, flat region detection, and spatial extrema identification.

Experimental validation demonstrates both methods' effectiveness across diverse scenarios. The RRT*-APF approach efficiently generates paths with appropriate clearance and smooth orientation transitions, enabling successful navigation in moderately constrained environments. Performance metrics reveal that the algorithm typically requires only four to five exploration steps to identify feasible paths, with clearance measurements confirming safe navigation throughout execution. The VAMP framework extends these capabilities to highly cluttered spaces, generating optimized configuration sequences that enable the robot to adaptively reshape and navigate through passages previously considered impassable. These sequences follow a minimal deformation principle, maintaining straighter configurations where possible and deforming only when necessary to navigate constrictions.

Performance analysis reveals important practical insights: navigation with adaptive morphology requires considerably longer execution times (2-11 minutes) primarily due to the multiple stiffness transition cycles necessary for shape adaptation. The complexity of required shape adaptations directly impacts completion time, with more deformations requiring more phase transitions. In the most challenging scenario, the second variable stiffness segment underwent ten phase transitions with significant deformation, while simpler scenarios required as few as one deformation per segment. Clearance measurements show that VAMP successfully navigates tighter spaces than the RRT*-APF method, though occasionally approaching safety boundaries without causing physical collisions.

The mechanical performance of variable stiffness segments during rigid states showed interesting characteristics, with the first segment demonstrating superior shape consistency compared to the second segment. This performance differential, when considered alongside thermal response patterns, suggests material composition variance between segments that affects both mechanical rigidity and phase transition speed.

The chapter makes significant contributions to robot navigation in constrained environments by introducing planning strategies that effectively leverage both

position-orientation planning and morphological adaptation. The resulting frameworks - hybrid RRT*-APF for moderate constraints and VAMP for severe constraints - provide complementary approaches that expand the operational capabilities of elongated robots in real-world cluttered environments, establishing the foundation for effective grasping and manipulation tasks in complex scenarios.

Chapter 8

Conclusions

THIS thesis has presented a novel approach to mobile robotics, introducing a hybrid robot that seamlessly integrates the paradigms of conventional rigid robotics and soft robotics. Our work addressed the limitations inherent in both approaches by developing a robot capable of transitioning between rigid and flexible states, thereby combining the precision and mobility of conventional robots with the adaptability and safe interaction capabilities of soft robots.

8.1 Summary of Contributions

Through our research, we have:

- Designed and fabricated the Self-Reconfigurable Soft-Rigid (2SR) robot, a novel hybrid mobile platform that successfully bridges the gap between conventional rigid robots and soft systems. The 2SR robot consists of two fundamental components: autonomous locomotion units equipped with omnidirectional wheels, sensors, and control systems, connected by a variable-stiffness bridge mechanism. This bridge, utilizing low melting point alloy (LMPA) as its core element, enables controlled transitions between rigid and flexible states, allowing the robot to adapt its morphology according to environmental demands. In its rigid state, the robot maintains precise positioning and can effectively transfer forces for manipulation tasks, while in its flexible state, it can conform to various shapes and navigate through confined spaces.

The research significantly advanced existing LMPA-based variable stiffness technology by introducing a modular design approach, which addresses traditional limitations of monolithic LMPA systems such as high power consumption, slow response times, and material inefficiency. The robot's operation is coordinated through an integrated control system that manages both the mobility of the locomotion units and the state transitions of the variable-stiffness mechanism. This unique combination of adaptive morphology and mobile manipulation capabilities positions the 2SR robot as a versatile platform for applications requiring both precise movement and environmental adaptation.

- Derived a comprehensive stiffness control system for a mobile robot equipped with modular variable stiffness segments based on Field's metal, a low melting point alloy (LMPA) that transitions between states at approximately 62°C. The control architecture was optimized through a series-connected configuration of modular units within each segment, monitored by a single temperature sensor. To overcome the challenges of limited sensing and complex thermal dynamics, we implemented a nonlinear temperature estimation model that accounts for thermal mass effects and heat transfer delays, providing more accurate state assessment. The control system's core component is a Finite-State Machine (FSM) that effectively manages discrete state transitions between rigid and flexible states while coordinating with continuous motion control. The system incorporates conservative temperature thresholds to ensure reliable operation and account for hysteresis in the phase transition process. Experimental validation using a single variable-stiffness segment demonstrated the system's effectiveness, achieving average transition times of 35.9 seconds for heating and 47.1 seconds for cooling, while successfully maintaining arbitrary shapes in the rigid state and enabling significant deformation in the flexible state. These results confirm the viability of our control approach for applications requiring adaptive morphology and precise stiffness control.

- Developed a comprehensive motion and morphology control framework, addressing the unique challenges of controlling a hybrid rigid-flexible robotic system. The framework encompasses three major components: a unified kinematic model that handles both rigid and flexible states, a sophisticated

control architecture, and experimental validation of the system's capabilities. The kinematic model identifies four distinct operational scenarios based on segment stiffness combinations and validates the constant curvature assumption for flexible segments, while incorporating logarithmic spiral trajectories for state transitions. The control architecture evolved from a baseline controller featuring basic motion planning and stiffness control to an advanced hierarchical framework utilizing Model Predictive Controllers for different operational modes. The platform successfully demonstrated pose-shape formation and object manipulation capabilities, while also revealing practical considerations such as wheel contact challenges during flexible-state operations. Experimental validation confirmed the system's ability to perform complex tasks that leverage both rigid and flexible states, though certain limitations were identified, particularly regarding wheel slip during flexible state operations.

- Designed a framework for curvilinear object manipulation using the 2SR robot, focusing on the challenges of implementing full-body grasping and optimizing object transport. For grasping, a three-phase strategy was developed (approach, grasp without contact, final contact) with configurations mathematically derived from object geometry. The system employs progressive offset positions to prevent object disturbance during approach. For object transport, an MPC-based pure pursuit algorithm tracks reference paths by linearizing object dynamics and optimizing control inputs over a prediction horizon. The robot-object contact model establishes a kinematic mapping between desired object motion and required robot velocities, enabling coordinated manipulation through the robot's variable-stiffness bridge that conforms to object surfaces. Experimental validation with four distinct object shapes (circle, ellipse, heart, and bean) demonstrated the framework's effectiveness while also revealing important insights into the relationship between object geometry and manipulation performance. The system showed particularly strong performance with larger objects that provided better surface contact, as demonstrated with the bean-shaped object, while the elliptical shape revealed limitations in the current approach. These findings indicated that system performance is primarily bounded by physical robot-object conformance rather than control limitations, suggesting future improvements

in areas such as force sensing integration, enhanced contact modelling, and adaptive control strategies.

- Developed sophisticated path planning approaches designed for manipulandum operation in cluttered environments: RRT*-APF and VAMP. The former algorithm combines Rapidly-Exploring Random Tree with an Artificial Potential Field, efficiently generating collision-free paths while maintaining safe distances from obstacles, though the resulting paths sometimes contain sharp turns that could benefit from smoothing techniques. The VAMP (Voronoi Assisted Morphological Planning) approach addresses navigation through highly cluttered environments when the RRT*-APF method fails to find a path. To solve this issue, we leverage the robot's morphological adaptability, decomposing the complex task into manageable steps and alternating between rigid and flexible states to navigate confined spaces. Experimental validation demonstrated successful execution of both traverse and transport tasks, with the 2SR robot effectively transitioning between states to navigate tight spaces while maintaining stability in open areas.

8.2 Future Work

Future work could focus on:

- *Advanced Learning-Based Control Systems*: Development of sophisticated reinforcement learning frameworks that can dynamically adapt to varying environmental conditions and task requirements. This would involve creating deep learning models trained on extensive simulation and real-world data to better handle the nonlinear dynamics of state transitions. The system could incorporate multi-modal sensing data (force, temperature, position) to make more informed decisions about morphological changes and movement strategies. This learning-based approach would reduce the current reliance on manual parameter tuning and could potentially enable the robot to develop emergent behaviours for complex manipulation tasks that were not explicitly programmed.

- *Enhanced Contact Modeling and Force Control:*: Implementation of a comprehensive contact modeling system integrated with real-time force sensing

capabilities. This would include developing detailed models of surface friction variations, local deformation effects, and contact pressure distribution across different object geometries. The system would benefit from multiple force sensors strategically placed along the robot's structure, enabling dynamic adjustment of grasping pressure and real-time assessment of grasp stability. This improved understanding of contact dynamics could lead to more sophisticated manipulation strategies, particularly for objects with challenging geometries or varying surface properties.

- *Optimization of Morphological Transitions*: Research into faster and more energy-efficient methods for state transitions between rigid and flexible configurations. This would involve investigating alternative LMPA materials with lower transition temperatures, developing more efficient heating/cooling mechanisms, and implementing predictive temperature control strategies. The optimization would also focus on reducing the current transition times while maintaining reliable operation. Additionally, this research direction would explore the possibility of achieving variable degrees of stiffness rather than just binary rigid/flexible states, potentially enabling more nuanced manipulation strategies and better adaptation to different task.

- *Multi-Robot Coordination and Collaborative Manipulation*: Extension of the current single-robot framework to enable coordinated operation of multiple 2SR robots. This would involve developing distributed control algorithms for collaborative object manipulation, implementing communication protocols for real-time state sharing between robots, and creating planning strategies for coordinated morphological changes. The multi-agent system could tackle more complex manipulation tasks, such as handling larger or more irregularly shaped objects, and could potentially achieve greater flexibility in confined spaces through coordinated shape-shifting behaviours.

- *Environmental Adaptation and Robustness*: Development of adaptive behaviours and control strategies to handle varying environmental conditions and unexpected disturbances. This would include creating robust state estimation methods that work reliably in different lighting conditions and on various surface types, implementing adaptive friction compensation for different floor materials, and developing recovery strategies for unexpected loss

of grasp or stability. The research would also focus on making the system more resilient to temperature variations, mechanical wear, and other real-world factors that could affect performance, ultimately working toward a more deployment-ready system suitable for practical applications.

Appendix A

List of Publications

Google Scholar: Luiza Labazanova

A.1 Peer-reviewed Journal Articles

- **L. Labazanova**, L. Qiu, J. G. Romero, T. Nanayakkara, and D. Navarro-Alarcon, "Full-Body Grasping for Combined Mobility and Object Manipulation," 2025.

  [In Progress] [video]

- **L. Labazanova**, S. Peng, L. Qiu, H.-Y. Lee, T. Nanayakkara, and D. Navarro-Alarcon, "Self-Reconfigurable Soft-Rigid Mobile Agent With Variable Stiffness and Adaptive Morphology," *IEEE Robotics and Automation Letters (RA-L)*, 2023.

  [DOI][video]

A.2 Peer-reviewed Conference Papers

- **L. Labazanova**, Z. Wu, Z. Gu, and D. Navarro-Alarcon, "Bio-Inspired Design of Artificial Striated Muscles Composed of Sarcomere-Like Contraction Units," *2021 20th International Conference on Advanced Robotics (ICAR)*, Dec. 2021.

- Z. Wu, **L. Labazanova**, P. Zhou, and D. Navarro-Alarcon, "A Novel Approach to Model the Kinematics of Human Fingers Based on an Elliptic Multi-Joint Configuration," *2021 20th International Conference on Advanced Robotics (ICAR)*, Dec. 2021.

- D. Navarro-Alarcon, **L. Labazanova**, M. K. Chow, and K. W. Ng, "Can a Tesla Turbine Be Utilised as a Non-Magnetic Actuator for MRI-Guided Robotic Interventions?," *2021 IEEE International Conference on Robotics and Biomimetics (ROBIO)*, pp. 1735–1742, 2021.

Bibliography

[1] I. Ermolov, "Industrial robotics review. in: Kravets, a. (eds) robotics: Industry 4.0 issues & new intelligent control paradigms.," *Studies in systems, Decision and Control*, vol. 272, p. 195–204, Jan 2020.

[2] S. Srinivas, S. Ramachandiran, and S. Rajendran, "Autonomous robot-driven deliveries: a review of recent developments and future directions," *Transportation Research Part E: Logistics and Transportation Review*, vol. 165, p. 102834, Sep 2022.

[3] C. Chen, E. Demir, Y. Huang, and R. Qiu, "The adoption of self-driving delivery robots in last mile logistics," *Transportation Research Part E: Logistics and Transportation Review*, vol. 146, p. 102214, Feb 2021.

[4] P. Ferreira and J. Reis, "A systematic literature review on the application of automation in logistics," *Logistics*, vol. 7, p. 80–80, Nov 2023.

[5] Y. Gao and S. Chien, "Review on space robotics: toward top-level science through space exploration," *Science Robotics*, vol. 2, p. eaan5074, Jun 2017.

[6] D. Huamanchahua, D. Yalli-Villa, A. Bello-Merlo, and J. Macuri-Vasquez, "Ground robots for inspection and monitoring: A state-of-the-art review," in *2021 IEEE 12th Annual Ubiquitous Computing, Electronics & Mobile Communication Conference (UEMCON)*, pp. 0768–0774, 2021.

[7] M. Kyrarini, F. Lygerakis, A. Rajavenkatanarayanan, C. Sevastopoulos, H. R. Nambiappan, K. K. Chaitanya, A. R. Babu, J. Mathew, and F. Makedon, "A survey of robots in healthcare," *Technologies*, vol. 9, p. 8, Jan 2021.

[8] M. H. Kang and S. Kim, "Research trends in entertainment robots: a comprehensive review of the literature from 1998 to 2024," *Digital Business*, vol. 5, p. 100102, Dec 2024.

[9] R. Riener, L. Rabezzana, and Y. Zimmermann, "Do robots outperform humans in human-centered domains?," *Frontiers in Robotics and AI*, vol. 10, Nov 2023.

[10] A. E. Direct, "2 wheel drive ultrasonic arduino projects robot kit," Dec 2022.

[11] A. Agarwal, A. Kumar, J. Malik, and D. Pathak, "Legged locomotion in challenging terrains using egocentric vision," in *The Conference on Robot Learning (CoRL) 2022*, Sep 2022.

[12] M. Bjelonic, N. Kottege, T. Homberger, P. Borges, P. Beckerle, and M. Chli, "Weaver: Hexapod robot for autonomous navigation on unstructured terrain," *Journal of Field Robotics*, vol. 35, p. 1063–1079, Jul 2018.

[13] T. Jin and X. Han, "Robotic arms in precision agriculture: a comprehensive review of the technologies, applications, challenges, and future prospects," *Computers and Electronics in Agriculture*, vol. 221, p. 108938–108938, Jun 2024.

[14] S. Jarecha, B. Mewada, and A. Mistry, "Robotic arm review," *International Journal of Research Publication and Reviews*, vol. 4, no. 5, p. 8061–8066, 2024.

[15] M. Blatnický, J. Dižo, J. Gerlici, M. Sága, T. Lack, and E. Kuba, "Design of a robotic manipulator for handling products of automotive industry," *International Journal of Advanced Robotic Systems*, vol. 17, Feb 2020.

[16] Z. Samadikhoshkho, K. Zareinia, and F. Janabi-Sharifi, "A brief review on robotic grippers classifications," in *2019 IEEE Canadian Conference of Electrical and Computer Engineering (CCECE)*, pp. 1–4, 2019.

[17] L. Birglen and T. Schlicht, "A statistical review of industrial robotic grippers," *Robotics and Computer-Integrated Manufacturing*, vol. 49, p. 88–97, Feb 2018.

[18] Y. Jiang, Z. Huang, B. Yang, and W. Yang, "A review of robotic assembly strategies for the full operation procedure: planning, execution and evaluation," *Robotics and Computer-Integrated Manufacturing*, vol. 78, p. 102366, Dec 2022.

[19] M. Li, J. Huang, L. Xue, and R. Zhang, "A guidance system for robotic welding based on an improved yolov5 algorithm with a realsense depth camera," *Scientific Reports*, vol. 13, p. 21299, Dec 2023.

[20] J. Bai, S. Lian, Z. Liu, K. Wang, and D. Liu, "Deep learning based robot for automatically picking up garbage on the grass," *IEEE Transactions on Consumer Electronics*, vol. 64, p. 382–389, Aug 2018.

[21] W. Kornmaneesang, S.-L. Chen, and S. Boonto, "Contouring control of an innovative manufacturing system based on dual-arm robot," *IEEE Transactions on Automation Science and Engineering*, vol. 19, p. 2042–2053, Jul 2022.

[22] Y. Rivero-Moreno, S. Echevarria, C. Vidal-Valderrama, L. Pianetti, J. Cordova-Guilarte, J. Navarro-Gonzalez, J. Acevedo-Rodríguez, G. Dorado-Avila, L. Osorio-Romero, C. Chavez-Campos, K. Acero-Alvarracín, Y. Rivero, S. Echevarria, C. Vidal-Valderrama, L. Pianetti, J. C. Guilarte, J. Navarro-Gonzalez, J. Acevedo-Rodríguez, G. L. D. Avila, and L. Osorio-Romero, "Robotic surgery: a comprehensive review of the literature and current trends," *Cureus*, vol. 15, Jul 2023.

[23] R. Raj and A. Kos, "A comprehensive study of mobile robot: History, developments, applications, and future research perspectives," *Applied Sciences*, vol. 12, p. 6951, Jul 2022.

[24] H. Shen, J. Zeng, and Y. Yang, "Overview of technologies in marine robotics," *Lecture Notes in Computer Science*, p. 340–351, Jan 2023.

[25] E. Zereik, M. Bibuli, N. Mišković, P. Ridao, and A. Pascoal, "Challenges and future trends in marine robotics," *Annual Reviews in Control*, vol. 46, p. 350–368, 2018.

[26] L. Tagliavini, G. Colucci, A. Botta, P. Cavallone, L. Baglieri, and G. Quaglia, "Wheeled mobile robots: State of the art overview and kinematic comparison among three omnidirectional locomotion strategies," *Journal of Intelligent & Robotic Systems*, vol. 106, Oct 2022.

[27] Z. Yin, J. Liu, B. Chen, and C. Chen, "A delivery robot cloud platform based on microservice," *Journal of Robotics*, vol. 2021, p. 1–10, Feb 2021.

[28] J. Laber, R. Thamma, and E. Kirby, "The impact of warehouse automation in amazon's success," *IJISET - International Journal of Innovative Science, Engineering & Technology*, vol. 7, no. 8, p. 63–70, 2020.

[29] Y. Zhong, R. Wang, H. Feng, and Y. Chen, "Analysis and research of quadruped robot's legs: a comprehensive review," *International Journal of Advanced Robotic Systems*, vol. 16, p. 172988141984414, May 2019.

[30] Y. Mae, A. Yoshida, T. Arai, K. Inoue, K. Miyawaki, and H. Adachi, "Application of locomotive robot to rescue tasks," in *Proceedings. 2000 IEEE/RSJ International Conference on Intelligent Robots and Systems (IROS 2000) (Cat. No.00CH37113)*, vol. 3, pp. 2083–2088 vol.3, 2000.

[31] I. Dronova, C. Kislik, Z. Dinh, and M. Kelly, "A review of unoccupied aerial vehicle use in wetland applications: Emerging opportunities in approach, technology, and data," *Drones*, vol. 5, p. 45, May 2021.

[32] A. Rovira-Sugranes, A. Razi, F. Afghah, and J. Chakareski, "A review of ai-enabled routing protocols for uav networks: Trends, challenges, and future outlook," *Ad Hoc Networks*, vol. 130, p. 102790, May 2022.

[33] N. Ghodsian, K. Benfriha, A. Olabi, V. Gopinath, and A. Arnou, "Mobile manipulators in industry 4.0: a review of developments for industrial applications," *Sensors*, vol. 23, p. 8026–8026, Sep 2023.

[34] P. Ben-Tzvi, A. A. Goldenberg, and J. W. Zu, "Design and analysis of a hybrid mobile robot mechanism with compounded locomotion and manipulation capability," *Journal of Mechanical Design*, vol. 130, May 2008.

[35] O. Lee, D. Kim, Y. Kim, W. Kim, S. Lee, D. Y. Kim, Y.-O. Kim, and K. Kim, "Development and validation of reconfigurable autonomous mobile manipulator for flexible manufacturing process," in *2023 23rd International Conference on Control, Automation and Systems (ICCAS)*, pp. 914–918, 2023.

[36] G. ALICI, "Softer is harder: What differentiates soft robotics from hard robotics?," *MRS Advances*, vol. 3, no. 28, p. 1557–1568, 2018.

[37] S. Mintchev and D. Floreano, "Adaptive morphology: a design principle for multimodal and multifunctional robots," *IEEE Robotics & Automation Magazine*, vol. 23, p. 42–54, Sep 2016.

[38] M. Kovač, Wassim-Hraiz, O. Fauria, J.-C. Zufferey, and D. Floreano, "The epfl jumpglider: A hybrid jumping and gliding robot with rigid or folding wings," in *2011 IEEE International Conference on Robotics and Biomimetics*, pp. 1503–1508, 2011.

[39] M. A. Woodward and M. Sitti, "Multimo-bat: a biologically inspired integrated jumping–gliding robot," *The International Journal of Robotics Research*, vol. 33, p. 1511–1529, Sep 2014.

[40] F. Zhao, W. Wang, J. Wyrwa, J. Zhang, W. Du, and P. Zhong, "Design and demonstration of a flying-squirrel-inspired jumping robot with two modes," *Applied Sciences*, vol. 11, p. 3362–3362, Apr 2021.

[41] C. Liu, O. Edwards, K. Althoefer, K. Zhang, and H. Godaba, "An electro-pneumatic shape morphing rolling robot with variable locomotion modes," in *2022 IEEE 5th International Conference on Soft Robotics (RoboSoft)*, pp. 715–721, 2022.

[42] Y. Yudong, X. Fengyu, Y. Hongliang, and Z. PengFei, "A rolling soft cable climbing robot: Design analysis and fabrication," in *2017 IEEE International Conference on Robotics and Biomimetics (ROBIO)*, pp. 663–668, 2017.

[43] T. Yanagida, R. Elara Mohan, T. Pathmakumar, K. Elangovan, and M. Iwase, "Design and implementation of a shape shifting rolling–crawling–wall-climbing robot," *Applied Sciences*, vol. 7, p. 342, Mar 2017.

[44] F. Boria, R. Bachmann, P. Ifju, R. Quinn, R. Vaidyanathan, C. Perry, and J. Wagener, "A sensor platform capable of aerial and terrestrial locomotion," in *2005 IEEE/RSJ International Conference on Intelligent Robots and Systems*, pp. 3959–3964, 2005.

[45] L. Daler, S. Mintchev, C. Stefanini, and D. Floreano, "A bioinspired multi-modal flying and walking robot," *Bioinspiration & Biomimetics*, vol. 10, p. 016005, Jan 2015.

[46] J. P. Ramirez and S. Hamaza, "Multimodal locomotion: next generation aerial–terrestrial mobile robotics," *Advanced intelligent systems*, Dec 2023.

[47] R. J. Lock, R. Vaidyanathan, S. C. Burgess, and J. Loveless, "Development of a biologically inspired multi-modal wing model for aerial-aquatic robotic vehicles through empirical and numerical modelling of the common guillemot,uria aalge," *Bioinspiration & Biomimetics*, vol. 5, p. 046001–046001, Nov 2010.

[48] X. Liang, M. Xu, L. Xu, P. Liu, X. Ren, Z. Kong, J. Yang, and S. Zhang, "The amphihex: A novel amphibious robot with transformable leg-flipper composite propulsion mechanism," in *2012 IEEE/RSJ International Conference on Intelligent Robots and Systems*, pp. 3667–3672, 2012.

[49] R. J. Lock, R. Vaidyanathan, and S. C. Burgess, "Impact of marine locomotion constraints on a bio-inspired aerial-aquatic wing: Experimental performance verification," *Journal of Mechanisms and Robotics*, vol. 6, Oct 2013.

[50] A. A. Chafik, J. Gaber, S. Tayane, M. Ennaji, J. Bourgeois, and T. El Ghazawi, "From conventional to programmable matter systems: a review of design, materials, and technologies," *ACM Computing Surveys*, vol. 56, p. 1–26, Apr 2024.

[51] K. Gilpin, A. Knaian, and D. Rus, "Robot pebbles: One centimeter modules for programmable matter through self-disassembly," in *2010 IEEE International Conference on Robotics and Automation*, pp. 2485–2492, 2010.

[52] Y. Ozkan-Aydin and D. I. Goldman, "Self-reconfigurable multilegged robot swarms collectively accomplish challenging terradynamic tasks," *Science Robotics*, vol. 6, Jul 2021.

[53] J. Zhou, J. Wang, J. He, J. Gao, A. Yang, S. Hu, and Q. Li, "Design, fabrication, and control algorithm of self-reconfigurable modular intelligent vehicles," *Applied Sciences*, vol. 12, p. 6886–6886, Jul 2022.

[54] E. Hawkes, B. An, N. M. Benbernou, H. Tanaka, S. Kim, E. D. Demaine, D. Rus, and R. J. Wood, "Programmable matter by folding," *Proceedings of the National Academy of Sciences*, vol. 107, p. 12441–12445, Jun 2010.

[55] H. Gu, M. Möckli, C. Ehmke, M. Kim, M. Wieland, S. Moser, C. Bechinger, Q. Boehler, and B. J. Nelson, "Self-folding soft-robotic chains with reconfigurable shapes and functionalities," *Nature Communications*, vol. 14, Mar 2023.

[56] C. H. Belke and J. Paik, "Mori: a modular origami robot," *IEEE/ASME Transactions on Mechatronics*, vol. 22, p. 2153–2164, Oct 2017.

[57] D. Rus and M. T. Tolley, "Design, fabrication and control of origami robots," *Nature Reviews Materials*, vol. 3, p. 101–112, May 2018.

[58] M. Cianchetti, C. Laschi, A. Menciassi, and P. Dario, "Biomedical applications of soft robotics," *Nature Reviews Materials*, vol. 3, p. 143–153, May 2018.

[59] D. Rus and M. T. Tolley, "Design, fabrication and control of soft robots," *Nature*, vol. 521, p. 467–475, May 2015.

[60] S. Kim, C. Laschi, and B. Trimmer, "Soft robotics: a bioinspired evolution in robotics," *Trends in Biotechnology*, vol. 31, p. 287–294, May 2013.

[61] R. K. Katzschmann, A. D. Marchese, and D. Rus, "Autonomous object manipulation using a soft planar grasping manipulator," *Soft Robotics*, vol. 2, p. 155–164, Dec 2015.

[62] Z. Gong, B. Chen, J. Liu, X. Fang, Z. Liu, T. Wang, and L. Wen, "An opposite-bending-and-extension soft robotic manipulator for delicate grasping in shallow water," *Frontiers in Robotics and AI*, vol. 6, Apr 2019.

[63] X. Peng, N. Zhang, L. Ge, and G. Gu, "Dimension optimization of pneumatically actuated soft continuum manipulators," in *2019 2nd IEEE International Conference on Soft Robotics (RoboSoft)*, pp. 13–18, 2019.

[64] R. F. Shepherd, F. Ilievski, W. Choi, S. A. Morin, A. A. Stokes, A. D. Mazzeo, X. Chen, M. Wang, and G. M. Whitesides, "Multigait soft robot," *Proceedings of the National Academy of Sciences*, vol. 108, p. 20400–20403, Nov 2011.

[65] S. A. Morin, R. F. Shepherd, S. W. Kwok, A. A. Stokes, A. Nemiroski, and G. M. Whitesides, "Camouflage and display for soft machines," *Science*, vol. 337, p. 828–832, Aug 2012.

[66] M. T. Tolley, R. F. Shepherd, B. Mosadegh, K. C. Galloway, M. Wehner, M. Karpelson, R. J. Wood, and G. M. Whitesides, "A resilient, untethered soft robot," *Soft Robotics*, vol. 1, p. 213–223, Sep 2014.

[67] S. Seok, C. D. Onal, K.-J. Cho, R. J. Wood, D. Rus, and S. Kim, "Meshworm: a peristaltic soft robot with antagonistic nickel titanium coil actuators," *IEEE/ASME Transactions on Mechatronics*, vol. 18, p. 1485–1497, Oct 2013.

[68] R. F. Shepherd, F. Ilievski, W. Choi, S. A. Morin, A. A. Stokes, A. D. Mazzeo, X. Chen, M. Wang, and G. M. Whitesides, "Multigait soft robot," *Proceedings of the National Academy of Sciences*, vol. 108, p. 20400–20403, Nov 2011.

[69] J. Tirado, C. D. Do, J. Moisson de Vaux, J. Jørgensen, and A. Rafsanjani, "Earthworm-inspired soft skin crawling robot," *Advanced Science*, vol. 11, Apr 2024.

[70] Y. Zhang, P. Li, J. Quan, L. Li, G. Zhang, and D. Zhou, "Progress, challenges, and prospects of soft robotics for space applications," *Advanced Intelligent Systems*, vol. 5, Jun 2022.

[71] C. D. Santina, C. Duriez, and D. Rus, "Model-based control of soft robots: a survey of the state of the art and open challenges," *IEEE Control Systems Magazine*, vol. 43, p. 30–65, Jun 2023.

[72] M. M. Gor and J. M. Prajapati, "A brief review on hybrid robot," in *International Journal of Innovative Research in Science, Engineering and Technology*, 2015.

[73] H. C. Lee, N. Elder, M. Leal, S. Stantial, E. Vergara Martinez, S. Jos, H. Cho, and S. Russo, "A fabrication strategy for millimeter-scale, self-sensing soft-rigid hybrid robots," *Nature Communications*, vol. 15, Sep 2024.

[74] L. Paternò, G. Tortora, and A. Menciassi, "Hybrid soft–rigid actuators for minimally invasive surgery," *Soft Robotics*, vol. 5, p. 783–799, Dec 2018.

[75] H.-T. Lin, G. G. Leisk, and B. Trimmer, "Goqbot: a caterpillar-inspired soft-bodied rolling robot," *Bioinspiration & Biomimetics*, vol. 6, p. 026007, Apr 2011.

[76] C. Liu, O. Edwards, K. Althoefer, K. Zhang, and H. Godaba, "An electro-pneumatic shape morphing rolling robot with variable locomotion modes," in *2022 IEEE 5th International Conference on Soft Robotics (RoboSoft)*, pp. 715–721, 2022.

[77] R. J. Lock, S. C. Burgess, and R. Vaidyanathan, "Multi-modal locomotion: from animal to application," *Bioinspiration & Biomimetics*, vol. 9, p. 011001, Dec 2013.

[78] M. Kovač, Wassim-Hraiz, O. Fauria, J.-C. Zufferey, and D. Floreano, "The epfl jumpglider: A hybrid jumping and gliding robot with rigid or folding wings," in *2011 IEEE International Conference on Robotics and Biomimetics*, pp. 1503–1508, 2011.

[79] Y. Chen, *Development of Lobster-Inspired Hybrid Actuators for Compliant Robotic Applications*. PhD thesis, Monash University, Sep 2020.

[80] Z. Li, X. Chu, X. Hu, Z. Zhang, N. Li, and J. Li, "Variable stiffness methods for robots: a review," *Smart Materials and Structures*, vol. 33, p. 063002–063002, Oct 2023.

[81] Y. Xia, Y. He, F. Zhang, Y. Liu, and J. Leng, "A review of shape memory polymers and composites: Mechanisms, materials, and applications," *Advanced Materials*, vol. 33, p. 2000713, Sep 2020.

[82] J.-S. Koh, S.-M. An, and K.-J. Cho, "Finger-sized climbing robot using artificial proleg," in *2010 3rd IEEE RAS & EMBS International Conference on Biomedical Robotics and Biomechatronics*, pp. 610–615, 2010.

[83] B. Kim, M. G. Lee, Y. P. Lee, Y. Kim, and G. Lee, "An earthworm-like micro robot using shape memory alloy actuator," *Sensors and Actuators A: Physical*, vol. 125, p. 429–437, Jan 2006.

[84] H. M. Jaeger, "Celebrating soft matter's 10th anniversary: toward jamming by design," *Soft Matter*, vol. 11, no. 1, p. 12–27, 2015.

[85] E. Steltz, A. M. Mozeika, J. Rembisz, N. Corson, and H. M. Jaeger, "Jamming as an enabling technology for soft robotics," *Proceedings of SPIE*, Mar 2010.

[86] M. A. Karimi, V. Alizadehyazdi, H. M. Jaeger, and M. Spenko, "A self-reconfigurable variable-stiffness soft robot based on boundary-constrained modular units," *IEEE Transactions on Robotics*, vol. 38, no. 2, p. 1–12, 2021.

[87] T. Buschmann and B. Trimmer, "Bio-inspired robot locomotion," *Neurobiology of Motor Control*, p. 443–472, Jun 2017.

[88] K. H. Low, T. Hu, S. Mohammed, J. Tangorra, and M. Kovac, "Perspectives on biologically inspired hybrid and multi-modal locomotion," *Bioinspiration & Biomimetics*, vol. 10, p. 020301, Mar 2015.

[89] W. D. Shin, J. Park, and H.-W. Park, "Development and experiments of a bio-inspired robot with multi-mode in aerial and terrestrial locomotion," *Bioinspiration & Biomimetics*, vol. 14, p. 056009, Jul 2019.

[90] P. Amodio, N. Josef, N. Shashar, and G. Fiorito, "Bipedal locomotion in octopus vulgaris: a complementary observation and some preliminary considerations," *Ecology and Evolution*, Mar 2021.

[91] S. Miller, J. Van Der Burg, and F. Van Der Meché, "Locomotion in the cat: Basic programmes of movement," *Brain Research*, vol. 91, p. 239–253, Jun 1975.

[92] R. Baines, S. K. Patiballa, J. Booth, L. Ramirez, T. Sipple, A. Garcia, F. Fish, and R. Kramer-Bottiglio, "Multi-environment robotic transitions through adaptive morphogenesis," *Nature*, vol. 610, p. 283–289, Oct 2022.

[93] R. D. Quinn, G. M. Nelson, R. J. Bachmann, D. A. Kingsley, J. T. Offi, T. J. Allen, and R. E. Ritzmann, "Parallel complementary strategies for implementing biological principles into mobile robots," *The International Journal of Robotics Research*, vol. 22, p. 169–186, Mar 2003.

[94] R. E. Ritzmann, R. D. Quinn, and M. S. Fischer, "Convergent evolution and locomotion through complex terrain by insects, vertebrates and robots," *Arthropod Structure & Development*, vol. 33, p. 361–379, Jul 2004.

[95] A. S. Boxerbaum, J. Oro, G. Peterson, and R. D. Quinn, "The latest generation whegs™ robot features a passive-compliant body joint," in *2008 IEEE/RSJ International Conference on Intelligent Robots and Systems*, pp. 1636–1641, 2008.

[96] Y.-S. Kim, G.-P. Jung, H. Kim, K.-J. Cho, and C.-N. Chu, "Wheel transformer: a wheel-leg hybrid robot with passive transformable wheels," *IEEE Transactions on Robotics*, vol. 30, p. 1487–1498, Dec 2014.

[97] D. Zarrouk, A. Pullin, N. Kohut, and R. S. Fearing, "Star, a sprawl tuned autonomous robot," in *2013 IEEE International Conference on Robotics and Automation*, pp. 20–25, 2013.

[98] Y. She, C. J. Hurd, and H.-J. Su, "A transformable wheel robot with a passive leg," in *2015 IEEE/RSJ International Conference on Intelligent Robots and Systems (IROS)*, pp. 4165–4170, 2015.

[99] S.-C. Chen, K.-J. Huang, W.-H. Chen, S.-Y. Shen, C.-H. Li, and P.-C. Lin, "Quattroped: a leg–wheel transformable robot," *IEEE/ASME Transactions on Mechatronics*, vol. 19, p. 730–742, Apr 2014.

[100] U. Saranli, M. Buehler, and D. E. Koditschek, "Rhex: a simple and highly mobile hexapod robot," *The International Journal of Robotics Research*, vol. 20, p. 616–631, Jul 2001.

[101] H. Komsuoğlu, K. Sohn, R. J. Full, and D. E. Koditschek, "A physical model for dynamical arthropod running on level ground," *Springer tracts in advanced robotics*, p. 303–317, Jan 2009.

[102] K. C. Galloway, J. E. Clark, and D. E. Koditschek, "Variable stiffness legs for robust, efficient, and stable dynamic running," *Journal of Mechanisms and Robotics*, vol. 5, Jan 2013.

[103] J. Brackenbury, "Caterpillar kinematics," *Nature*, vol. 390, p. 453–453, Dec 1997.

[104] I. K. Kuder, A. F. Arrieta, W. E. Raither, and P. Ermanni, "Variable stiffness material and structural concepts for morphing applications," *Progress in Aerospace Sciences*, vol. 63, p. 33–55, Nov 2013.

[105] S. Wolf, G. Grioli, O. Eiberger, W. Friedl, M. Grebenstein, H. Höppner, E. Burdet, D. G. Caldwell, R. Carloni, M. G. Catalano, D. Lefeber, S. Stramigioli, N. Tsagarakis, M. Van Damme, R. Van Ham, B. Vanderborght, L. C. Visser, A. Bicchi, and A. Albu-Schäffer, "Variable stiffness actuators: Review on design and components," *IEEE/ASME Transactions on Mechatronics*, vol. 21, no. 5, pp. 2418–2430, 2016.

[106] N. Pagliarani, L. Arleo, S. Albini, and M. Cianchetti, "Variable stiffness technologies for soft robotics: a comparative approach for the stiff-flop manipulator," *Actuators*, vol. 12, p. 96, Mar 2023.

[107] Z. H. Rao and G. Q. Zhang, "Thermal properties of paraffin wax-based composites containing graphite," *Energy Sources, Part A: Recovery, Utilization, and Environmental Effects*, vol. 33, p. 587–593, Jan 2011.

[108] G. Raza, S. Iqbal, and A. Farooq, "Paraffin wax-based thermal composites," *IntechOpen eBooks*, Jun 2021.

[109] R. Brito-Pereira, C. Tubio, P. Costa, and S. Lanceros-Mendez, "Multifunctional wax based conductive and piezoresistive nanocomposites for sensing applications," *Composites Science and Technology*, vol. 213, p. 108892, Sep 2021.

[110] N. G. Cheng, A. Gopinath, L. Wang, K. Iagnemma, and A. E. Hosoi, "Thermally tunable, self-healing composites for soft robotic applications," *Macromolecular Materials and Engineering*, vol. 299, p. 1279–1284, Jun 2014.

[111] W. H. Choong, H. H. Hamidi, and K. B. Yeo, "Self-healing efficiency study of thermoset-thermoplastic polymer material," *IOP Conference Series Materials Science and Engineering*, vol. 1217, p. 012004–012004, Jan 2022.

[112] D. McCoul, W. Nie, P. Kim, C. Kengla, C. Clouse, and A. Atala, "Thermoplastic polycaprolactone elastomer for a 3d-printed pericardial scaffold in the treatment of dilated cardiomyopathy," *Bioprinting*, vol. 28, p. e00252, Dec 2022.

[113] J. Li, J. Li, Z. Wu, and Y. Huang, "A soft variable stiffness hand with an integrated actuating–cooling system," *IEEE Transactions on Industrial Electronics*, vol. 70, no. 11, pp. 11464–11473, 2023.

[114] I. Ward, "The molecular structure and mechanical properties of polyethylene terephthalate fibers," *Textile Research Journal*, vol. 31, p. 650–664, Jul 1961.

[115] L. N. Ji, "Study on preparation process and properties of polyethylene terephthalate (pet)," *Applied Mechanics and Materials*, vol. 312, p. 406–410, Feb 2013.

[116] A. K. Singh, R. Bedi, and B. S. Kaith, "Composite materials based on recycled polyethylene terephthalate and their properties – a comprehensive review," *Composites Part B: Engineering*, vol. 219, p. 108928, Aug 2021.

[117] T. T. Hoang, P. T. Phan, M. T. Thai, N. H. Lovell, and T. N. Do, "Bio-inspired conformable and helical soft fabric gripper with variable stiffness and touch sensing," *Advanced Materials Technologies*, vol. 5, p. 2000724, Nov 2020.

[118] S. Bahl, H. Nagar, I. Singh, and S. Sehgal, "Smart materials types, properties and applications: a review," *Materials Today: Proceedings*, vol. 28, p. 1302–1306, Jan 2020.

[119] N. Jain, S. N. Ovhal, V. Patil, and K. N. Kartik, "Smart materials – a state-of-the-art-review," *Materials Today Proceedings*, vol. 82, p. 381–389, Mar 2025.

[120] Q. Zhao, H. J. Qi, and T. Xie, "Recent progress in shape memory polymer: New behavior, enabling materials, and mechanistic understanding," *Progress in Polymer Science*, vol. 49-50, p. 79–120, Oct 2015.

[121] A. Lendlein and O. E. C. Gould, "Reprogrammable recovery and actuation behaviour of shape-memory polymers," *Nature Reviews Materials*, vol. 4, p. 116–133, Jan 2019.

[122] T. Dayyoub, A. V. Maksimkin, O. V. Filippova, V. V. Tcherdyntsev, and D. V. Telyshev, "Shape memory polymers as smart materials: a review," *Polymers*, vol. 14, p. 3511, Aug 2022.

[123] Y. Zhang, N. Zhang, H. Hingorani, N. Ding, D. Wang, C. Yuan, B. Zhang, G. Gu, and N. X. Fang, "Fast-response, stiffness-tunable soft actuator by hybrid multimaterial 3d printing," *Advanced Functional Materials*, vol. 29, p. 1806698–1806698, Apr 2019.

[124] Q. Meng and J. Hu, "A review of shape memory polymer composites and blends," *Composites Part A: Applied Science and Manufacturing*, vol. 40, p. 1661–1672, Nov 2009.

[125] J. N. Rodriguez, C. Zhu, E. B. Duoss, T. S. Wilson, C. M. Spadaccini, and J. P. Lewicki, "Shape-morphing composites with designed micro-architectures," *Scientific Reports*, vol. 6, Jun 2016.

[126] Z. Noohi, S. Nosouhian, B. Niroumand, and G. Timelli, "Use of low melting point metals and alloys (tm $<$ 420°c) as phase change materials: a review," *Metals*, vol. 12, p. 945, May 2022.

[127] Y. Hao, J. Gao, Y. Lv, and J. Liu, "Low melting point alloys enabled stiffness tunable advanced materials," *Advanced Functional Materials*, vol. 32, p. 2201942, Apr 2022.

[128] L. Jin, X. Zhai, K. Zhang, and J. Jiang, "Unlocking the potential of low-melting-point alloys integrated extrusion additive manufacturing: Insights into mechani-

cal behavior, energy absorption, and electrical conductivity," *Progress in Additive Manufacturing*, Sep 2024.

[129] Z. Xing, F. Wang, Y. Ji, D. McCoul, X. Wang, and J. Zhao, "A structure for fast stiffness-variation and omnidirectional-steering continuum manipulator," *IEEE Robotics and Automation Letters*, vol. 6, p. 755–762, Apr 2021.

[130] R. Takahashi, T. L. Sun, Y. Saruwatari, T. Kurokawa, D. R. King, and J. P. Gong, "Creating stiff, tough, and functional hydrogel composites with low-melting-point alloys," *Advanced Materials*, vol. 30, p. 1706885, Mar 2018.

[131] J. S. Kumar, P. S. Paul, G. Raghunathan, and D. G. Alex, "A review of challenges and solutions in the preparation and use of magnetorheological fluids," *International Journal of Mechanical and Materials Engineering*, vol. 14, Nov 2019.

[132] V. Chauhan, A. Kumar, and R. Sham, "Magnetorheological fluids: a comprehensive review," *Manufacturing review*, vol. 11, p. 6–6, Jan 2024.

[133] Q.-A. Nguyen, S. Jorgensen, J. Ho, and L. Sentis, "Characterization and testing of an electrorheological fluid valve for control of erf actuators," *Actuators*, vol. 4, p. 135–155, Jun 2015.

[134] I. C. Vladu and V. Stoian, "Hyper-redundant arm with er fluid based actuator and control system," in *2018 22nd International Conference on System Theory, Control and Computing (ICSTCC)*, pp. 317–322, 2018.

[135] A. J. Mazursky, J.-H. Koo, and T.-H. Yang, "Design, modeling, and evaluation of a slim haptic actuator based on electrorheological fluid," *Journal of Intelligent Material Systems and Structures*, vol. 30, p. 2521–2533, Mar 2019.

[136] J. Cao, L. Qin, J. Liu, Q. Ren, C. C. Foo, H. Wang, H. P. Lee, and J. Zhu, "Untethered soft robot capable of stable locomotion using soft electrostatic actuators," *Extreme Mechanics Letters*, vol. 21, p. 9–16, May 2018.

[137] T. Wang, J. Zhang, Y. Li, J. Hong, and M. Y. Wang, "Electrostatic layer jamming variable stiffness for soft robotics," *IEEE/ASME Transactions on Mechatronics*, vol. 24, no. 2, pp. 424–433, 2019.

[138] M. Yamano, N. Ogawa, M. Hashimoto, M. Takasaki, and T. Hirai, "A contraction type soft actuator using poly vinyl chloride gel," in *2008 IEEE International Conference on Robotics and Biomimetics*, pp. 745–750, 2009.

[139] M. Al-Rubaiai, X. Qi, Z. Frank, R. Tsuruta, U. Gandhi, K. J. Kim, and X. Tan, "Nonlinear modeling and control of polyvinyl chloride (pvc) gel actuators," *IEEE/ASME Transactions on Mechatronics*, vol. 27, no. 4, pp. 2168–2175, 2022.

[140] Z. Frank and K. J. Kim, "On the mechanism of performance improvement of electroactive polyvinyl chloride (pvc) gel actuators via conductive fillers," *Scientific Reports*, vol. 12, Jun 2022.

[141] C. Liu, H. Qin, and P. T. Mather, "Review of progress in shape-memory polymers," *Journal of Materials Chemistry*, vol. 17, p. 1543–1558, 4 2007.

[142] N. C. Rosenfeld and N. M. Wereley, "Volume-constrained optimization of magnetorheological and electrorheological valves and dampers," *Smart Materials and Structures*, vol. 13, p. 1303–1313, 9 2004.

[143] M. E. Hossain and C. Ketata, "Experimental study of physical and mechanical properties of natural and synthetic waxes using uniaxial compressive strength test," in *Proceedings of the Third International Conference on Modeling, Simulation and Applied Optimization*, 2011.

[144] A. Tonazzini, S. Mintchev, B. Schubert, B. Mazzolai, J. Shintake, and D. Floreano, "Variable stiffness fiber with self-healing capability," *Advanced Materials*, vol. 28, p. 10142–10148, 9 2016.

[145] C. Chautems, A. Tonazzini, Q. Boehler, S. H. Jeong, D. Floreano, and B. J. Nelson, "Magnetic continuum device with variable stiffness for minimally invasive surgery," *Advanced Intelligent Systems*, vol. 2, p. 1900086, 10 2019.

—